Numerische Analyse der hydrodynamischen Stabilität in der Schmelze bei der Czochralski-Züchtung oxidischer Kristalle

vorgelegt von
Dipl.-Ing.
Nebojša Crnogorac
aus Sarajevo

von der Fakultät V – Verkehrs- und Maschinensysteme
der Technischen Universität Berlin
zur Erlangung des akademischen Grades

Doktor der Ingenieurwissenschaften
- Dr.-Ing. -

genehmigte Dissertation

Promotionsausschuss:

Vorsitzender:	Prof. Dr. Wolfgang H. Müller
Gutachter:	Prof. Dr. Jörn Sesterhenn
Gutachter:	Prof. Dr. Roberto Fornari

Tag der wissenschaftlichen Aussprache: 16.05.2013

Berlin 2013
D 83

Dedication and acknowledgments

Acknowledgements

This work was supported by the German-Israeli Foundation (GIF), Grant no. I-794-145.10/2003. I am grateful to our team leader Dr. R. Uecker and the director of the Leibniz Institute for Crystal Growth (IKZ) Prof. Dr. R. Fornari for their support.

I am especially grateful to my supervisor Dr. H. Wilke from IKZ, where I got the chance and support to prepare this work.

I would like to thank the technical staff M. Bernhagen, M. Brützam, and A. Tauchert from the oxide laboratory at IKZ for support in realizing the measurement setups and for useful advices.

I am especially indebted to Prof. Dr. K. A. Cliffe from the University of Nottingham for his help and many useful advices. Also, I would like to thank our GIF partner Prof. Dr. A. Y. Gelfgat from the University of Tel-Aviv for his help and constructive critique. I appreciate the very useful practical measurement technique advices of Prof. Dr. D. Schwabe from the University of Giessen.

Scientific contributions

Parts of this work have already been published in international peer reviewed journals and/or were presented at international scientific conferences as oral or poster presentations.

Journal publications

- N. Crnogorac, H. Wilke and K.A. Cliffe: Numerical Study of Hydrodynamic Instabilities during Growth of Dielectric Crystals from the Melt. In: Journal of Crystal Growth 303, 1, 246 (2007), (Proceedings of the Fifth Workshop on Modelling in Crystal Growth - IWMCG-5)
- M.H. Tavakoli, H. Wilke and N. Crnogorac: Influence of the Crucible Bottom Shape on the Heat Transport and Fluid Flow during the Seeding Process of Oxide Czochralski Growth. In: Crystal Research and Technology 42, 1252 (2007)
- N. Crnogorac, H. Wilke, K.A. Cliffe, A.Y. Gelfgat and E. Kit: Numerical Modelling of Instability and Supercritical Oscillatory States in a Czochralski Model System of Oxide Melts. In: Crystal Research and Technology 43, 606 (2008)
- N. Crnogorac and H. Wilke: Measurement of physical properties of $DyScO_3$ melt. In: Crystal Research and Technology 44, 581 (2009)

Oral presentations

- N. Crnogorac*, H. Wilke and K.A. Cliffe: Numerical Study of Hydrodynamic Instabilities during Growth of Dielectric Crystals from the melt, 5. International Workshop on Modelling in Crystal Growth, Bamberg/Germany (2006)
- N. Crnogorac*, H. Wilke and K.A. Cliffe: Neue Erkenntnisse zur Stabilität der Strömung in oxidischen Schmelzen, DGKK-Arbeitskreis - Kristalle für Laser und Nichtlineare Optik, Hamburg/Germany (2006)
- N. Crnogorac*, H. Wilke, K.A. Cliffe and A.Y. Gelfgat: Numerical Bifurcation Study for Czochralski Crystal Growth, Internal presentation at the Leibniz Institute for Crystal Growth (IKZ), Berlin/Germany (2006)
- N. Crnogorac*, H. Wilke and K.A. Cliffe: Bifurkation und Pfadverfolgung in der Kristallzüchtung, Arbeitskreis der Deutschen Gesellschaft für Kristallwachstum und Kristallzüchtung (DGKK) - 5. Workshop für Angewandte Simulation in der Kristallzüchtung, Iphofen/Germany (2007)

- N. Crnogorac*, H.Wilke and K.A. Cliffe: Spiral Growth of High Melting Point Oxide Crystals, Fifth International Conference on Solid State Crystals and Eighth Polish Conference on Crystal Growth (ICSSC-5 and PCCG-8), Zakopane/Poland (2007)
- H. Wilke*, K.A. Cliffe and N. Crnogorac: Continuation Methods for Detecting Spiral Growth of High Melting Point Oxide Crystals, The 15th International Conference on Crystal Growth, Salt Lake City/USA (2007)
- N. Crnogorac*, H. Wilke, K.A. Cliffe and A.Y. Gelfgat: Numerische Analyse der hydrodynamischen Stabilität in der Schmelze bei der Cz-Züchtung oxidischer Kristalle, Colloquium at the Leibniz Institute for Crystal Growth (IKZ), Berlin/Germany (2008)

Poster presentations

- M.H. Tavakoli, H. Wilke and N. Crnogorac*: Influence of the Crucible Bottom Shape on the Heat Transport and Fluid Flow during the Seeding Process of Oxide Czochralski Crystal Growth, Fifth International Conference on Solid State Crystals and Eighth Polish Conference on Crystal Growth (ICSSC-5 and PCCG-8), Zakopane/Poland (2007)
- N. Crnogorac, H. Wilke, K.A. Cliffe, A. Y. Gelfgat* and E. Kit: A comparison Exercise for Computational Modelling of Instability and Supercritical Oscillatory States of Melt Flows in Czochralski Growth of Oxide Crystals, The 15th International Conference on Crystal Growth, Salt Lake City/USA (2007)
- N. Crnogorac*, H. Wilke and K.A. Cliffe: Influence of the RF-heating Configuration during Growth of High Melting Point Oxide Crystals, Jahrestagung der Deutschen Gesellschaft für Kristallwachstum und Kristallzüchtung (DGKK), München/Germany (2008)

Authors of oral and/or poster presentations marked with (*) are the corresponding speakers/presenters.

Contents

List of Figures

List of Tables

Chapter 1

Introduction

The present work arose from investigations of hydrodynamic instabilities which may occur in the melt flow during Czochralski crystal growth of high melting point oxides. It was supported by the German-Israeli Foundation and prepared at the Leibniz Institute for Crystal Growth in Berlin (German group). The analyzed problems of the hydrodynamic instability in a Czochralski crucible were investigated partly by two groups applying two independent numerical techniques. The second group is the Israeli group of Prof. Dr. A. Y. Gelfgat at Tel-Aviv University.

1.1 Motivation

Many processes arising in scientific and industrial applications require a non-trivial or time and cost intensive analysis. Often this analysis cannot be done experimentally. Therefore mathematical models are necessary, which can be used in numerical simulations. The fast progress in computer performance allows for applying very complex numerical models and solving many scientific and technological questions.
In crystal growth numerical simulations play an important role. Since 1950's the growth of crystals is applied industrially using different methods [2–4]. Crystals can be grown from gas phase epitaxially (e.g. chemical vapour deposition - CVD), from solution (e.g. top seeded solution growth - TSSG) or from the melt (e.g. Bridgman, Czochralski or floating zone method). This way crystals with one crystallographic direction (single), many crystallographic directions (poly) or solids without any characteristic geometry (amorphous) can be grown. For the best crystallographic perfection the Czochralski (Cz) and floating zone (FZ) method has been established producing bulk crystals with high quality and excellent physical properties and chemical stability.

Single bulk crystals grown by the Cz method have a wide application field in science and industry. Semiconductive crystals (e.g. Ge, Si) mainly are used in microelectronic and photovoltaic applications. The second large segment of industrially grown single crystals are oxides, which are used in optoelectronic, laser or sensor applications or as substrates in epitaxial crystal growth. The range of oxide single crystals is huge and they are designed to satisfy the demands of upcoming applications. Important examples are rare earth scandates ($ReScO_3$,Re=La, Ce, Pr, Nd, Sm, Eu, Gd, Tb and Dy), which can be used as substrates in epitaxial crystal growth. From the crystallographic point of view rare earth scandates are very interesting, because nearly all ranges of lattice constants are adjustable by selecting the proper rare earth type and therefore it can be used in almost all epitaxial applications (strain engineering of perovskite thin films [5]). From the technological side the very high melting temperature which is about $2100 \circ C$ requires special conditions for rare earth scandates. Difficulties occur during finding the optimal technological parameters and often symmetry breaking of the axisymmetric crystal growth arises (see fig. 1.1 (A-C)). This symmetry breaking is called spiral

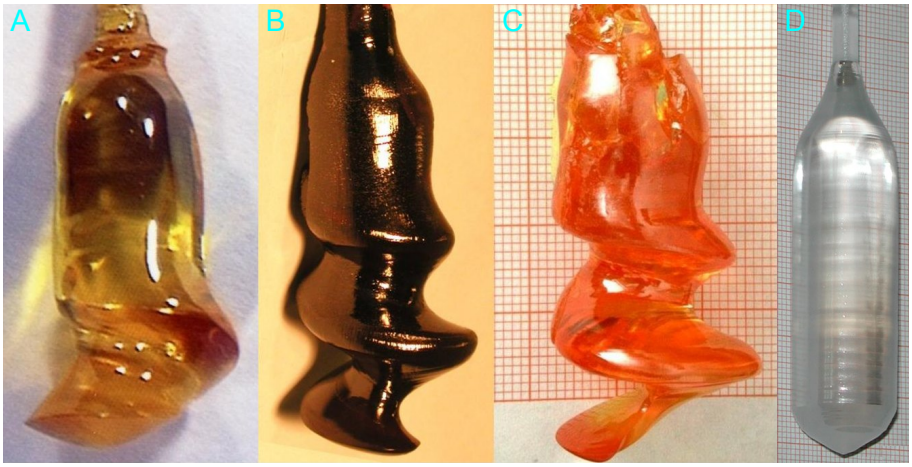

Figure 1.1: Rare-earth scandate crystals grown at the Leibniz Institute for Crystal Growth (IKZ) using the Czochralski method (A: dysprosium scandate ($DyScO_3$), B: neodymium scandate ($NdScO_3$), C: samarium scandate ($SmScO_3$), D: gadolinium scandate ($GdScO_3$)).

growth or spiral pattern and it leads to decreased yield of the usable single crystal. The high operating temperatures require a very compact and good insulated Cz setup, thus an experimental investigation of the spiral growth is non-trivial. Therefore numerical methods were used to clarify the initiation process of spiral patterns during growth of rare earth scandates. The

complex interaction of flow generated by buoyancy, rotation and surface tension leads to the hypothesis, that heat and momentum changes in the melt initiate the unwanted occurrence of spiral patterns when growing rare earth scandate crystals. It must be noted, that not all rare earth scandates show a spiral pattern (see fig. 1.1 (D)). Apparently, the heat transport, especially via internal radiation, in the crystal during the growth plays a role in the spiral growth mechanism [6].

1.2 Czochralski crystal growth

During the last century scientists like Kossel [7], Stranski [8], Volmer [9] and other made their contribution to crystal growth. Many crystal growth techniques have been developed, e.g. the Verneuil method, Bridgman method or Czochralski (Cz) method [2–4]. In the present work bulk oxide crystals grown from melt using the Cz method [10, 11] were investigated.
The Cz method is one of the most important techniques in crystal growth which is named after the Polish scientist Jan Czochralski ($\star$1885; †1953) [12]. Using the Cz technology single crystals of metals, semiconductors, oxides, fluorides and other multicomponent materials can be grown [4, 13, 14]. The basic idea is to dip a small seed crystal into the melt and pull out a single crystal of defined diameter. The temperature differences cause a crystallization of the melt and the crystal grows. Better results can be obtained, if the crystal is being rotated, additionally [11]. This is because rotational forces compete against the thermal forces, so that the crystal growth becomes more stable. The second effect of rotation is the influence on the distribution of dopants, which are added if the physical properties of the crystal should be changed, e.g. in crystals for laser application [15, 16]. Applying this simple procedure in connection with a certain temperature field, which is controllable by the position of the heat source, cylindrical single crystals with a high degree of structural perfection are the result. However, it should be noticed, that the Cz crystal growth technology is steadily being improved and developed, even today [4, 14, 17–23].
Fig. 1.2 shows the principle sketch of a state-of-the-art Cz crystal growth facility. The whole Cz apparatus is located in a water cooled steel vessel, which is evacuated and filled with an quasi inert gas, e.g. nitrogen or argon. The crucible contains the melt. Therefore it has to be chemically and physically stable up to very high temperatures (e.g. rare earth scandates melt around 2100°C). Usually platinum (up to $\approx$ 1650°C) or iridium (up to $\approx$ 2300°C) crucibles are used, because of their good chemical stability in oxide environments. For heating graphite heaters can be used achieving

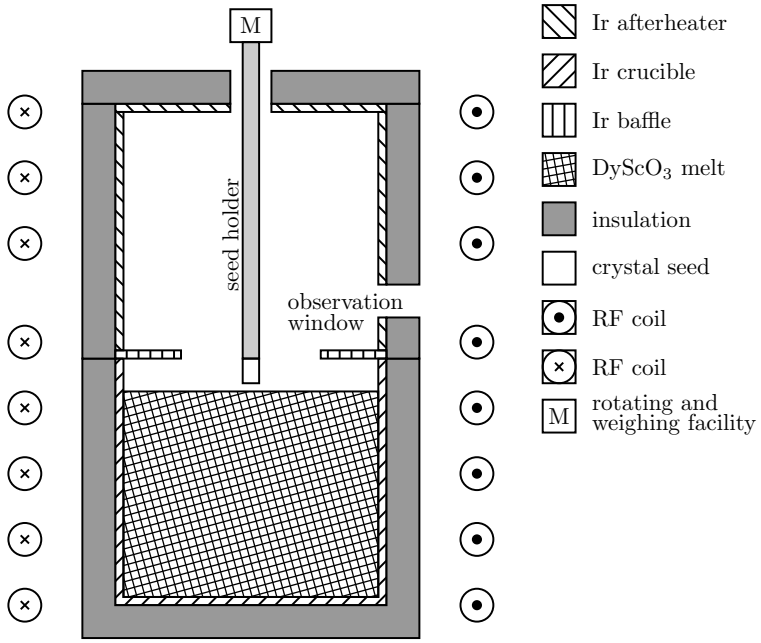

Figure 1.2: The principle sketch of a Czochralski (Cz) crystal growth facility. (Ir: iridium, $DyScO_3$: dysprosium scandate, RF: radio frequency)

very high temperatures, but they are unsuitable in oxide environments. For oxides/scandates an inductive heating is suitable, only (see chapter 4). In fig. 1.2 the radio frequency (RF) coils are shown. Their relative position to the crucible and the gap height between the windings are controlling the temperature field in the system. Of course, the used amount of generator power determines the absolute temperature. Additionally, the temperature distribution in the upper part above the melt is controlled by an active afterheater. This affects directly the temperature field in the crystal and is used to avoid mechanical crackings in the grown crystal. In contrast to the active afterheater, a passive afterheater has no corresponding RF coils. The whole system must be insulated by ceramics in order to keep the heat losses as minimal as possible and to be able to melt the oxide substances, without local overheating of the crucible. However, an observation window is necessary, which is an unwanted heat sink.
A seed holder is connected to the rotating and weighing facility. It fixes the seed and has to be centre aligned as good as possible. This is not trivial in practice, and is necessary to avoid unbalances. The weighing facility generates a weight signal which is used in connection with the generator power signal for the automatic computer-assisted crystal growth control. The crystal rotation typically ranges between 5-20 rpm. In fig. 1.2 an iridium baffle

above the melt is shown, also. It can be inclined and reflects the heat from the melt surface. It affects the temperature field and stabilizes the flow in the melt, additionally. More about the Cz setup can be found in [24].
A typical Cz crystal growth run consists of 6 steps. Fig. 1.3 shows the first three steps. Before starting the crystal growth the basic oxide substances have to be molten (fig. 1.3, a). In the case of dysprosium scandate ($DyScO_3$) these are dysprosium oxide (Dy_2O_3) and scandium oxide (Sc_2O_3). Often, because of smaller density of the raw substances, it is not possible to produce enough melt at once. Therefore the first step must be applied several times unless enough melt is produced.

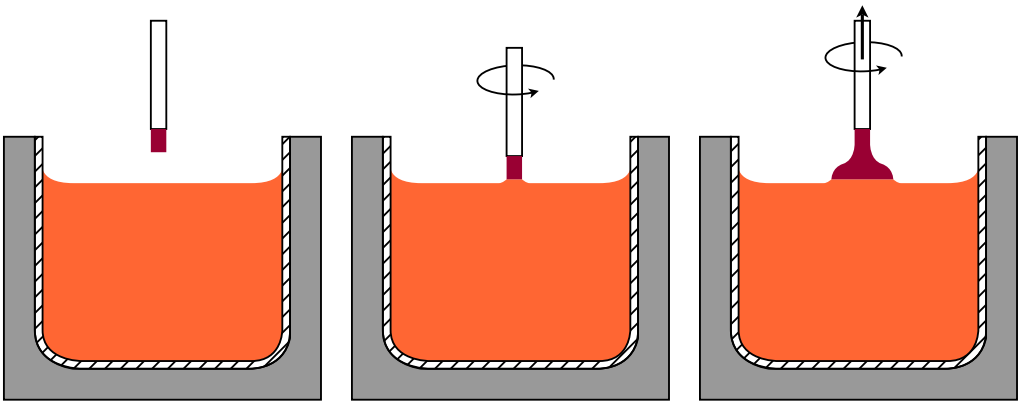

(a) melting process (b) seeding process (c) crowning process

Figure 1.3: Sketch of first three principle steps in a Cz crystal growth run.

The next step needs a small single crystal for the seeding process (fig. 1.3, b). The seed is cut out of another single crystal with certain crystallographic alignment. The seeding process is the most sensitive step in Cz crystal growth, because the right temperature has to be found. Is the temperature too high, the seed melts away, and is the temperature too low, the melt surface starts to solidify. This process is done manually by the crystal grower while observing the seed and the melt surface through the observation window (see fig. 1.2). After the melt has reached the melting point, it is slightly overheated. Then the single crystal seed with the desired orientation (e.g. $\langle 100 \rangle$ or $\langle 0\bar{1}0 \rangle$), which is connected to the seed holder and the pulling rod, is being moved down until it touches the melt surface. Afterwards, it needs some experimental experience to adjust the temperature in order to get a thermal equilibrium at the melt-crystal interface. Under suitable thermal conditions, e.g. slightly undercooled melt, crystallization occurs around the single crystal seed [24–26]. The crystal grows in the same crystallographic direction as the single crystal seed. After this sensitive process the crystal

can be lifted up with a certain pulling rate. Only a successful seeding process will guarantee that further steps will result in a cylindrically formed crystal. A meniscus is formed around the crystals edge at the melt-crystal interface as the result of the balance of the surface tension against gravity.
In fig. 1.4 a shape of the liquid meniscus with a cylindrical crystal is shown. Thereby, $r_1(t)$ and $r_2(t)$ are the time dependent radii of the meniscus curvature, $h(t)$ is the meniscus height and α is the contact angle.

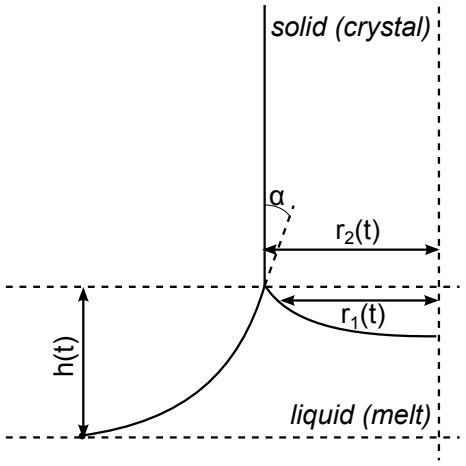

Figure 1.4: Shape of the meniscus with a cylindrical crystal.

In the case of incomplete wetting the contact angle is $\alpha \neq 0$ and is characteristic for any substance. α depends mainly on the surface tension of the melt and on the density difference between melt and crystal. Therefore, the shape of the meniscus is determined mainly by the magnitude of the surface tension of the melt and external forces (e.g. gravity). The meniscus shape is a function of the contact angle α and the external forces and is described by the solution of the Young-Laplace differential equation 1.1 (see also [20]).

$$\Delta p = \sigma \left(\frac{1}{r_1(t)} + \frac{1}{r_2(t)} \right) \tag{1.1}$$

Thereby, Δp is the pressure difference across the phase interface (solid/melt) and σ is the surface tension of the melt. Changing the crystal radius, the meniscus shape changes, also. Therefore the crystal diameter control is very important during crystal growth.
After a successful seeding process the crystal is grown with a very small diameter, even smaller than the seed diameter, for a certain crystal length. This is called necking and reduces the dislocation density in the crystal core by forcing the dislocations to "grow out" to the surface of the crystal.

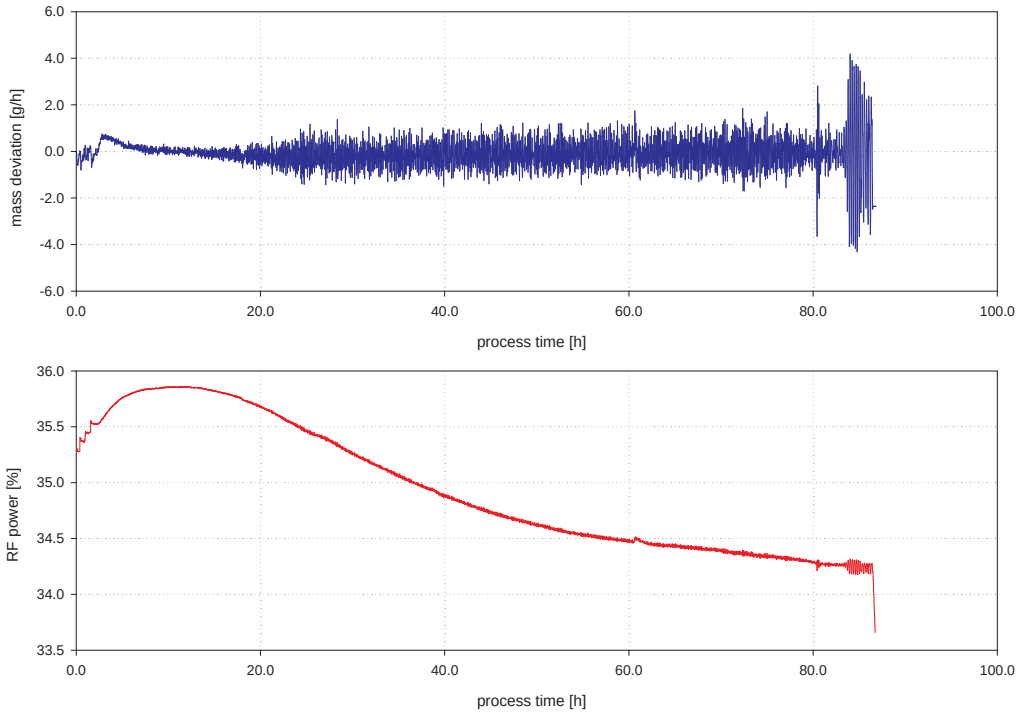

Figure 1.5: RF generator power signal and weight signal example during a $DyScO_3$ automatic crystal growth run.

After the necking process the next steps are done automatically by the computer-assisted software using the weight signal and the RF generator power signal (see fig. 1.5). The crowning process (fig. 1.3, c) sets the desired diameter of the resulting single crystal and is usually not critical.
The last three steps are shown in fig. 1.6. The main step of the Cz method is the growth process (fig. 1.6, a). It takes about one week for a $DyScO_3$ crystal and is done automatically. Normally this step is not critical, but especially the rare earth scandates show sometimes unwanted spiral growth. If this happens the crystal growth process has to be stopped.
After the crystal is grown completely almost all melt is consumed and the crystal has to be moved slowly away from the melt. This process is called tailing (fig. 1.6, b). The crystal is pulled faster and the diameter is becoming smaller. In the last step the crystal is being removed and the system has to be cooled down slowly (fig. 1.6, c).
From the physical point of view the fluid flow in the melt and the resulting heat transport is the most important phenomenon in the Cz crystal growth process. Fig. 1.7 illustrates the available flows in the melt, i.e. buoyancy

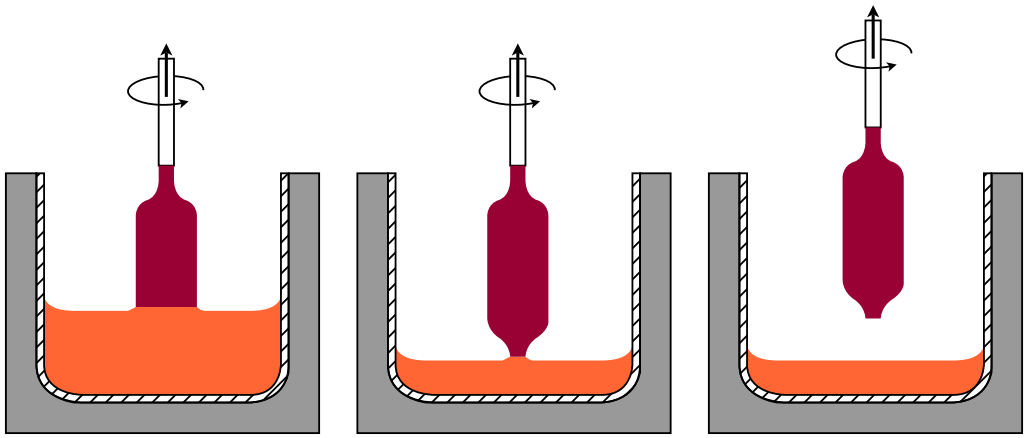

(a) growing process (b) tailing process (c) removing and cooling process

Figure 1.6: Sketch of last three principle steps in a Cz crystal growth run.

driven flow, flow caused by rotational forces and the thermocapillary flow (Marangoni flow) [27] at the melt surface caused by the temperature dependence of the surface tension and the temperature differences at the melt surface.
The electromagnetic field of the RF coils (see fig. 1.2) induces heat in the metalic parts, i.e. iridium crucible and afterheater. Due to the non-uniform heating of the crucible and the melt, there is a temperature difference across the melt. The hot melt is lighter than cold melt with the consequence of different fluid densities. According to the Archimedian principle, this leads to buoyancy, which induces a convection. This type of convection is called free, natural or buoyancy driven convection/flow (fig. 1.7, a).

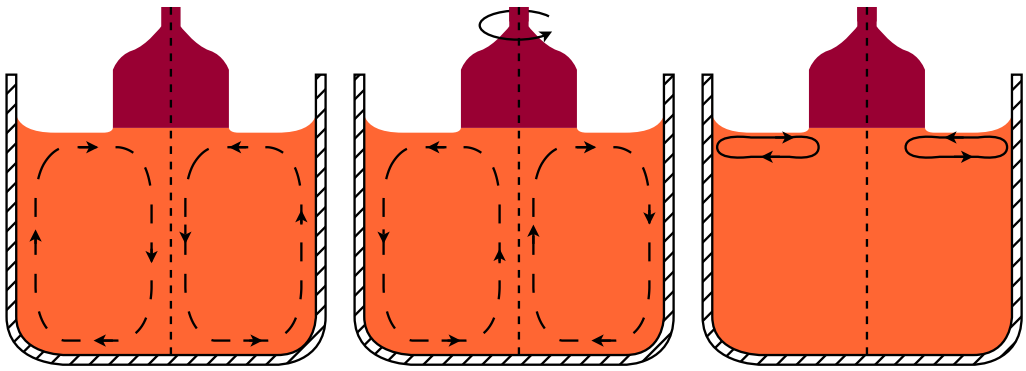

(a) flow due to buoyancy (b) flow due to rotation (c) Marangoni flow

Figure 1.7: Cz melt flow mechanisms.

Due to the melt viscosity, the crystal rotation generates shear forces in the

melt, so that the melt is forced to move in the azimuthal direction (azimuthal flow). Additionally, the rotation induces centrifugal forces, which drive the melt radially outward. This is called forced convection (fig. 1.7, b).
Along the free melt surface (interface between melt and gas) a fluid motion exists caused by the Marangoni effect [27], which occur due to a surface tension gradient. Since the melt with higher surface tension exerts a higher force to its surrounding than the melt with lower surface tension, the surface tension gradient causes a flow away from regions of lower surface tension. This gradient can be caused by concentration or temperature differences. The latter dominates for the surface tension of crystal melts. The resulting flow is called Marangoni convection (fig. 1.7, c). However, the flow pattern near the free melt surface is more complex, since the melt-gas interface is not planar and additionally there are heat losses.
The mass and heat transfer in the melt is affected by a combination of these mechanisms and is characterized by the melt flow pattern. This pattern influences directly the quality of the crystal, its shape, size and the growth rate [28, 29]. Therefore the hydrodynamic flow in the melt is very important and is under intensive research since many years [30–32]. Also for semiconductors, especially silicon, melt flow has been investigated, but can be very different from oxide melt flow [33, 34].
Beside the arrangement of the crystal growth setup, applied temperature distributions and the flow pattern, also the shape of the melt-crystal interface influences significantly the quality of the grown single crystal [35–38]. A deflected interface, convex or concave, can generate dislocations and other crystal defects as well as thermal stresses in the crystal during cooling, which lead to cracks and facets. Almost flat melt-crystal interfaces lead to best quality single crystals grown by the Cz technique, therefore it is important for crystal growers to find the corresponding operating conditions [39]. Sometimes the crystal suddenly changes its shape and forms a spiral. Spiral growth can take place on microscopic level [40–44] and on macroscopic level [45–49].
Rare earth scandates like $DyScO_3$ are often affected by such spiral growth [1, 5, 6, 30, 50], which is called cork screw growth also. The research in the present work has been concentrated mainly on the analysis of the onset of such spiral patterns during the growth of rare earth scandates.
The economy and the technological requirements of the industry force the crystal growers to find the best operating conditions resulting in single crystals of large size and best physical properties for a certain application. Using the Cz technique the adjustable parameters are the rotation rate of the crystal/crucible, pulling rate, temperature distribution, pressure, dopant profiles and of course the geometry of the Cz arrangement, especially the shape and the relative height of the RF coils and the setup of the insulation.

1.3 Numerical simulation in crystal growth

A very complex interaction of different fluid flow phenomena (free convection, forced convection and Marangoni convection) in the Cz melt strongly affect the quality and size of the grown crystal [17, 27]. Especially the physical behaviour close to the solidification interface, i.e. melt-crystal interface is complicated, since there the incorporation of atoms in the lattice of the crystal takes place (see fig. 1.8).

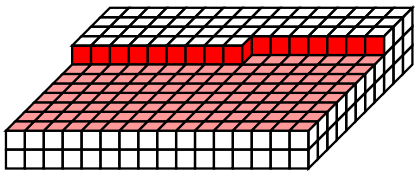

Figure 1.8: Crystal growth model after Kossel and Stranski [7, 8].

Therefore, the understanding of thermal conditions in the melt, crystal and gas atmosphere and the heat and mass transport in the melt is absolutely necessary for the optimization of the Cz crystal growth process. Good single crystal quality means avoiding crystal stresses, a high degree of lattice perfection, an uniformity of dopant distribution in the lattice as well as low defect and impurity density. These all depends strongly on the melt fluid flow and the thermal field in the Cz system. Since the transport of heat, mass and impurities is determined by the melt convection, it is important to be understood by the crystal grower. An interaction of crystal growers and scientists doing numerical simulation is a prerequisite for an optimization of the Cz crystal growth process. The crystal grower should have a good understanding of the fluid flow and other physical phenomena in the melt and the computational analyst should have a good understanding of the technological part of the Cz process.
Since it is a non-trivial task to perform experimental in-situ observations of the fluid flow and other physical phenomena during a real Cz crystal growth process, it is mandatory to use the methods of numerical simulation. Fig. 1.9 shows an example of calculated isotherms in a $DyScO_3$ melt. Under low temperature operating conditions ($\leq 500°C$) it is possible to use small particles (tracers) of almost identical density as the melt in order to visualize the melt flow [51–53]. For high melting temperatures as for rare earth scandates ($\approx 2100°C$) this is impossible. Beside the high temperatures, which reduce drastically the range of available materials for experimental utilities, the observation of the Cz process is difficult because of the good thermal insulation (ceramics) of the Cz crucible (see fig. 1.2), which is necessary for an uniform

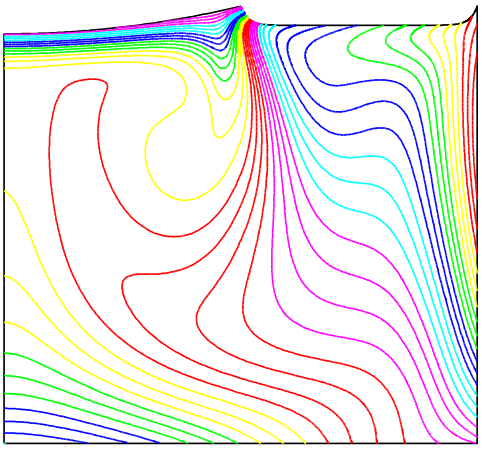

Figure 1.9: Example of isotherms in a dysprosium scandate ($DyScO_3$) melt with deformed melt-crystal interface as well as deformed free melt surface.

temperature distribution. The consequence is that despite of a large number of experiments carried out to understand the transport phenomena during the last decades [16, 30, 32, 54–60], the knowledge about the involved physical mechanisms during the melt convection is still insufficient, especially for state-of-the-art crystal melts like rare earth scandates.
The economy motivates the science to present quick solutions for current problems and to deliver single crystals of best crystallographic perfection and largest size, since the demand for single crystals is increasing steadily. The hope of solving the energy crisis using photovoltaic facilities based on semiconductors and reducing the power consumption of light emitting devices as well as the need for special oxide crystals for sensor and optoelectronics and for epitaxial application is actual more than ever. Therefore for the prediction and understanding of transport phenomena during crystal growth the numerical simulation must be used to support the crystal growers. The experimental difficulties at high temperatures, the large amount of parameter combinations and the costs of an unsuccessful growth process force the crystal grower to use results of numerical simulation. It can provide detailed information about the melt flow, heat generation and mass transfer and lead so to an improvement of the Cz process. This information can be partly qualitative and partly quantitative. Therefore accurate modelling is necessary and is a challenging problem due to the enormous complexity of the Cz process. Furthermore, the lack of accurate physical properties of special novice materials like rare earth scandates makes the simulation of its Cz process more difficult. During the simulation of melt fluid flow and temperature distribution the global mathematical problem, which determines the

Cz mechanism, contains variables which are partly or at all interdependent. They represent the temperature, pressure, melt flow velocity, heat quantity and other variables. Furthermore the simulation is determined by crystal rotation, pulling rate, different system geometries and other parameters, as well as by boundary conditions like heat radiation and temperatures at different model locations. The state-of-the-art numerical simulation of the Cz process must incorporate all these dependencies. The task is the optimization of Cz crystal growth enhancing the quality of the grown crystal.
Since there are several parameters in the simulation process the computational efforts can be very large for a realistic simulation [61, 62]. Therefore, in this work bifurcation theories [63–66] were used in order to reduce the range of possible parameter values. This way the parameter spaces, which are physically and technologically not meaningful, were excluded. This reduces the computational time considerably. As far as known, the analysis of the spiralling process of rare earth scandates by applying the hydrodynamic stability analysis is new in this field.

1.4 Heat and mass transfer

1.4.1 Heat Transfer

A temperature difference between two points causes heat transport. There are three important heat transfer mechanisms, which are conduction, convection and radiation [67, 68]. Conduction and convection are corresponding to a temperature in a medium (e.g. fluid). Thereby, heat transport due to conduction occurs across a stationary fluid. By contrast, convection occurs in a fluid, which is in motion. Thermal radiation is heat transfer by electromagnetic waves. There is external and internal thermal radiation. The latter is important in materials with very high melting point, especially (e.g. rare earth scandates) [6, 69, 70]. In general a mixture of all three heat transfer mechanisms occur at the same time.

Heat radiation

Radiative heat transfer is based on energy transport through electromagnetic waves. Every body whose temperature exceeds the absolute zero irradiates heat. The Stefan-Boltzmann law (1.2) describes this emission of electromagnetic waves, which carry energy away from an emitting body.

$$q = \sigma\epsilon(T^4 - T_a^4) \tag{1.2}$$

Here, ϵ is the emissivity, $\sigma = 5.67 \cdot 10^{-8} W/m^2K^4$ is the Stefan-Boltzmann constant, T is the body temperature and T_a is the surrounding temperature. A body can irradiate as well as receive radiation energy, so that net transfer of energy is given from higher to lower temperatures. Since the growth of rare earth scandates is done at a temperature around $2000 \circ C$, the portion of transferred energy by radiation is very high ($q \propto T^4$).

Heat conduction

Conductive heat transfer is based on the transfer of energy by vibrations at atomic level. In a medium with a temperature gradient, there is a flow of heat energy from regions of high temperature to regions of low temperature. This is known as conduction heat transfer and is described by Fourier's law 1.3.

$$q = -\kappa \nabla T \tag{1.3}$$

(1.3) describes the heat flux vector $\vec{q}$ for a given temperature T and thermal conductivity κ, which is an important material property during the simulation of crystal growth processes. In heat transfer analysis of incompressible fluids κ is often expressed as thermal diffusivity χ, which is the thermal conductivity divided by the volumetric heat capacity. (1.4) gives this relation, where c is the specific heat and ρ is the density.

$$\chi = \frac{\kappa}{\rho c} \tag{1.4}$$

Convective heat transfer

Convective heat transfer is a mechanism of heat transfer, which occurs due to the motion of a fluid. For a fluid at constant pressure and density, the heat transfer equation is given as

$$\chi \nabla^2 T - \vec{v} \cdot \nabla T = 0\,. \tag{1.5}$$

Two types of convection are mainly distinguished. Free convection is characterised by a fluid motion driven by buoyancy. Forced convection takes place when external forces (e.g. rotational forces) cause a fluid motion. In general both types of convection occur at the same time (mixed convection). Convective heat transfer is always connected with mass transfer, since there is always fluid motion.

1.4.2 Navier-Stokes equations

Navier-Stokes equations (1.6) describe the motion of a fluid element [68, 71, 72].

$$\underbrace{\overbrace{\rho\frac{\partial\vec{v}}{\partial t}}^{\text{unsteady acceleration}} + \overbrace{\rho\vec{v}\cdot\nabla\vec{v}}^{\text{convective acceleration}}}_{\text{momentum changes per element}} = \underbrace{\rho\vec{f}}_{\substack{\text{other external}\\ \text{forces}}} - \underbrace{\overbrace{\nabla p}^{\text{pressure gradient}} + \overbrace{\nabla(\mu\nabla\vec{v})}^{\text{viscous forces}}}_{\text{stress divergence}} \quad (1.6)$$

Equation (1.6) is valid for incompressible flow of Newtonian fluids with certain viscosity and gives the equilibrium between accelerated unit mass (left-hand side) and external forces acting on this unit (right-hand side). The vector $\vec{f}$ represents external forces, such as gravity and centrifugal forces, but also electromagnetic Lorentz forces, if the fluid contains charge carriers. Gravitational forces cause natural convection, which is driven by buoyancy and damped by the viscous forces in the moving fluid. Thereby, the viscosity dissipates kinetic energy and the buoyancy force releases internal energy.
The Boussinesq approximation of (1.6) is commonly used in numerical analysis of fluid flow. It neglects the effects of density differences $\Delta\rho$ in fluids due to spatial temperature differences. This is only allowed, if $\Delta\rho$ is sufficiently small (max. 1%) compared to the overall density of the fluid, which is given for many flows arising in nature and engineering [71]. In all terms of equation (1.6) a mean density ρ_0 is applied, except where in the term multiplied by the gravitational vector g (buoyancy term) [68]. The gravity amplifies the density differences, so that they cannot be neglected. In the gravity term the state equation (1.7) for density is applied. T_0 is a reference temperature at which ρ_0 is measured, β_T is the thermal expansion coefficient and g is the gravitational constant.

$$\rho = \rho_0(1 - \beta_T(T - T_0)) \quad (1.7)$$

Based on (1.7) non-dimensional quantities are defined describing external forces on fluid elements. The Rayleigh number Ra is a measure for the buoyancy driven convection and is defined in (1.8).

$$Ra = Gr\,Pr = \frac{g\beta}{\nu\chi}T_m R^3 \quad (1.8)$$

R is the characteristic length, χ is the thermal diffusivity and ν is the kinematic viscosity. Ra can be expressed as the product of the dimensionless numbers Gr and Pr. The Grashof number Gr (1.9) describes the ratio of buoyancy to viscous forces acting on the fluid.

$$Gr = \frac{g\beta T_m R^3}{\nu^2} \quad (1.9)$$

The Prandtl number $Pr = \nu/\chi$ is the ratio of kinematic viscosity to thermal diffusivity. It is a measure for heat transport in the fluid.

1.4.3 Continuity equation

The continuity equation describes the mass conservation and its differential form is given as 1.10.

$$\frac{\partial \rho}{\partial t} + \nabla \cdot (\rho \vec{v}) = 0 \tag{1.10}$$

Here, ρ is the density of the fluid, t is the time and $\vec{v}$ is the fluid velocity. The continuity equation simplifies for the incompressible fluid ($\rho = constant$) to 1.11.

$$\nabla \cdot \vec{v} = 0 \tag{1.11}$$

1.4.4 Marangoni convection

This convection type depends strongly on surface tension γ of a medium and therefore occurs mainly in a thin layer close to the interface of two media (e.g. crystal melt / gas). Concretely, it occurs when a gradient of fluid surface tension exists. This gradient can be caused by concentration or temperature differences. The Marangoni effect [27] due to temperature differences is called thermocapillary convection, also. It is based on the shear stress balance at the media interface as shown in (1.12).

$$\mu_1 \frac{\partial u_1}{\partial z} - \mu_2 \frac{\partial u_2}{\partial z} = \frac{\partial \gamma}{\partial x} = \frac{\partial \gamma}{\partial T} \frac{\partial T}{\partial x} \tag{1.12}$$

For the majority of pure liquids the temperature dependence of γ is negative [73]. The Marangoni convection causes a fluid flow (mass transfer) from regions of low γ (hot fluid) to regions of high γ (colder fluid).

1.4.5 Stream function and streamline

Streamlines are used as geometrical utility for the visualization of fluid flow in 2D. Thereby, the velocity vector $\vec{v} = (u, v)$ of the velocity field is tangential to the streamlines [66–68]. Therefore, they show the travelling direction of a flow element at any point in time. Fig. 1.10 shows two competing eddies in a Cz melt and illustrates how streamlines are plotted.
It can be seen, that

$$\frac{v}{u} = \frac{dy}{dx} \tag{1.13}$$

is the slope of a streamline.

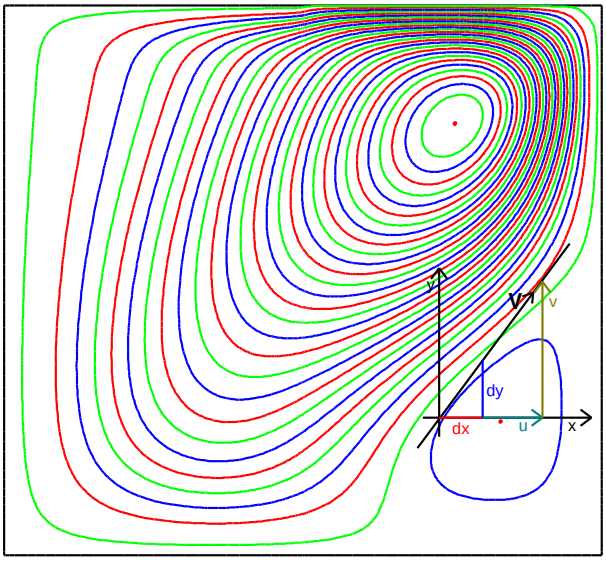

Figure 1.10: Example of a streamline field of a melt flow in the Czochralski (Cz) crucible and a velocity vector along a streamline.

A scalar function whose contour lines define the stream lines is called the stream function ψ. It is defined in order to meet the physical phenomena. It was defined as

$$u = \frac{\partial \psi}{\partial y} \ , \ v = -\frac{\partial \psi}{\partial x} \ , \text{ so that } d\psi = \frac{\partial \psi}{\partial x} dx + \frac{\partial \psi}{\partial y} dy = -v dx + u dy \ . \quad (1.14)$$

Streamlines are paths of constant ψ. The difference between ψ values at any two points is the volumetric flow rate (flux) through a line connecting these two points and fulfills the 2D continuity condition (1.10, 1.11).

1.5 Numerical analysis

Numerical analysis is dealing with the study and construction of algorithms for problems of continuous mathematics. This science predates the invention of modern computers by many centuries, e.g. linear interpolation has been used BC [74, 75]. Many important algorithms [76] like Newton's method, Gaussian elimination or Euler's method remind one that many great mathematicians of the past had used numerical analysis.
Computations were performed by hand, thus value tables were generated and stored in large books containing important formulas and other numerical data. Since the invention of powerful computers the numerical analysis

has strengthened its position in all fields of engineering, physical and mathematical sciences.
Closed analytical solutions are available for simple mathematical problems. More complicated problems, which arise in crystal growth, like the heat transport equation or Navier-Stokes equations do not have in general an analytical solution, and therefore only a numerical solution can be obtained.
Numerical analysis distinguishes between direct and iterative methods for solving systems of equations. Direct methods are supposed to compute the solution in a finite number of steps, while iterative methods do not terminate the computation in a finite number of steps. The main difference between these two methods is that the first would compute the exact solution if it is applied in infinite precision arithmetic, while the iterative method only converges to the exact solution in an infinite number of steps. Gaussian elimination or the QR factorization for solving linear equation systems are examples for direct methods [76]. Iterative methods like Newton's method, the Jacobi iteration or the Cholesky decomposition are applied to very large problems [76, 77]. The generalized minimum residual method (GMRES) or the conjugate gradient method (CGM) are direct methods in principle, because after a very large number of steps the exact solution can be obtained. However, practically these methods are used as iterative methods, because the approximation of the solution is acceptable after several iterations [68, 76].
Practically, continuous problems must be discretized in such a way that the solution of the discretized problem finally approaches the solution of the continuous problem. Thereby, the discretization is applied to the time and space domain. A good example is the solution of ordinary differential equations and more complicated partial differential equations, which always lead to solving a large system of linear equations [78, 79] For example, the Navier-Stokes equations are first discretized and then transformed into a finite dimensional subspace (e.g. Krylov subspace). This process can be performed by the finite difference (FDM), finite volume (FVM) or finite element (FEM) method [76, 77, 79].
In the process of solving a numerical problem many difficulties can arise and influence the solution. Therefore the study of the generation and propagation of errors in a numerical system is important. Roundoff, truncation as well as discretization errors can influence drastically the solution. The applied method must be numerically robust and stable, and the solution is supposed to be discretization independent [76]. Therefore it is important to understand the internals of the applied numerical method for an effective interpretation of the obtained numerical solution.
Numerical analysis is a great help for modelling systems, for which simple

analytic solutions are not available. Thereby, the verification and model validation of applied numerical methods are of crucial importance.
The solution structure of the fluid flow in a Czochralski (Cz) melt can be very complicated. Multiple solutions (see fig. 1.11) are possible and are not simple to detect [1, 30]. This solutions can be stable, unstable or oscillatory (see also fig. 2.5 in subsection 2.1.3). The latter is assumed to trigger the crystal spiral growth.

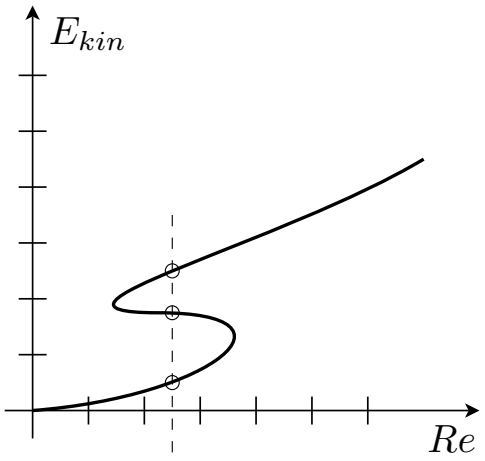

Figure 1.11: Example of multiple solutions (rotational Reynolds number Re vs. kinetic energy E_{kin} of the Cz melt flow).

Conventional software packages for modelling and simulation of fluid flow processes contain generic modules, which often perform direct numerical simulation only, detecting steady states, which may not reflect realistic solutions. Additionally, often such packages introduce special stabilizing elements (e.g. numerical viscosity, upwinding) [78, 79], which make the whole method numerically more robust, but applicable only for weak non-linearities. Both is dangerous, because important information of the solution space can get lost, thus the results of numerical simulation, especially of generic software packages, must be considered critically. Multiple solutions can be detected by a deep analysis of the solution structure only. Thereby, bifurcation analysis and path following algorithms can help considerably [63, 65, 66].

1.5.1 Finite difference vs. finite element method

The finite element method (FEM) [76, 78, 79] is applied for solving partial differential equations (PDE) approximately. The approximation replaces the PDE by simpler functions (interpolation functions) over used finite elements

(e.g. 1st or 2nd order polynomials). FEM is applied in many disciplines including fluid dynamics [68].
Another method for solving ordinary and partial differential equations is the method of finite differences (FDM) [76, 79], which is the most simple numerical method. The problem domain is discretized in a finite number of grid points. At each grid point the derivatives are approximated by differences, so that the PDE equations are replaced by a system of difference equations. The FDM method can be applied to almost all problems, but the main restrictions of this method encounter when modelling irregular geometries or setting special boundary conditions [68, 79].

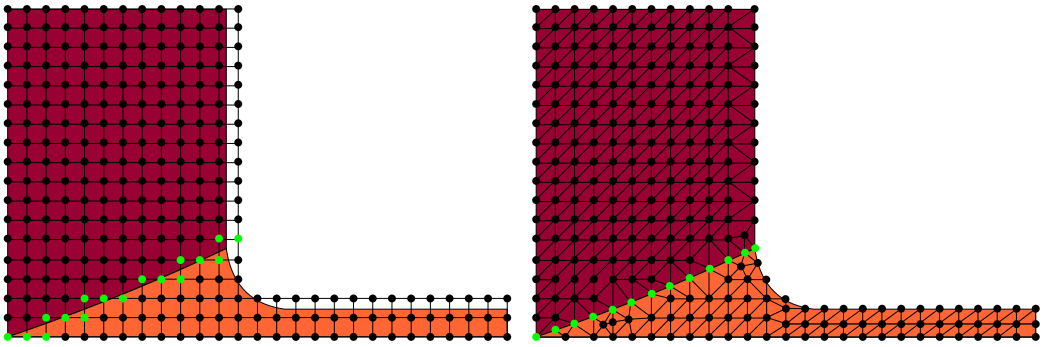

Figure 1.12: Finite difference (left) and finite element (right) discretization of the Czochralski (Cz) phase interface melt/crystal.

In contrast to the FDM method, which arranges the domain as an array of grid points, the FEM method [78] is modelling the problem domain with many subregions (elements) of any size, which are interconnected at interface points (nodes, nodal points or boundary points). This allows for representing very complex shapes. Fig. 1.12 shows a cutout of the Czochralski (Cz) melt-crystal phase interface comparing FDM and FEM grids.
The main problem with finite difference grids occurs on deformed boundaries (see fig. 1.12 (left)), so that the grid cannot modell the domain boundary exactly (aliasing effect) [79]. The big advantage of the FEM grid is that it can help itself with a wide variety of elements (e.g. triangle or rectangle), which can be assembled user-defined, so that the approximation is much better then with the FDM grid (see fig. 1.12 (right)). Therefore in the current work the FEM method was used for approximation of the Cz process under consideration. The degree of approximation depends on the size and number of elements in the grid and on the used interpolations functions, which at least have to satisfy the requirement for continuity of the function itself and its derivatives across adjoining element boundaries. The main procedure steps of applying the FEM-method is given in the following [78].

1. **Continuum discretization**

   First, the continuous domain describing a problem is divided into elements. The type of the elements (e.g. L3/2, T6/3 or Q9/4) and the number of elements depend on the degree of the geometrical deformation and on the physical processes, which have to be analysed. Different element types may be mixed. The resolution of the numerical analysis depends strongly on the grid size. Wrong grid size can cause wrong results. On the other hand the solution has to be grid independent. Especially, when the solution changes rapidly in a domain, the number of finite elements has to be increased in order to resolve this part of the domain. Thus, the analyst has to balance the grid properties with the demanded solution precision. In the present work the advanced FEM package ENTWIFE [80] was used for numerical simulations. It allows for a very flexible discretization with more than 50 different element types.

2. **Assignment of interpolation functions**

   Depending on the type of the used element certain interpolation functions are applied, which are usually polynomials, because of their simple integration and differentiation, respectively. The polynomial degree depends on the used element types. In ENTWIFE the interpolation functions for each element type are predefined, but can be also user defined.

3. **Generation of local matrix equations**

   The matrix equations for each element have to be determined exploring the properties of each element. For this purposes the *direct*, the *variational* or the *weighted residuals* approach can be used [79]. In the present work the latter approach has been applied, since it averages the variation from the solution, so that the approximation is better on average then that of the first two approaches.

4. **Assembling the global system matrix**

   All the local matrix equations of each element have to be assembled to a global matrix describing the behaviour of the overall system. Thereby, the nodal values at the boundary nodes (element interfaces) must be the same.

5. **Setting constraints**

For completing the global matrix, boundary conditions must be set. Boundary conditions can be described by functions, distributions, generalized fluxes, nodal laws and other user defined types. The ENTWIFE package supports many possibilities for setting the boundary conditions [81]. Results of previous computations can be used as initial values.

6. **Invoking the solver**

   In this step the unknowns of the steady state or time dependent problem, which are part of the global linear equation system are determined by solving this equation system. Usually iterative solvers (e.g. Newton-method, CGM) are applied [68, 76]. ENTWIFE supports a iterative Newton-Raphson solver. Thereby, the iterations can be solved with the direct solver MUMPS (MUltifrontal Massively Parallel Solver) [82]), which is very fast, but needs a huge main memory. In contrast, iterative methods need less main memory.

1.5.2 Galerkin method and weak form

There are many Galerkin class methods [76, 79], which differ in the applied approximation method, and are used to convert a continuous operator problem to a discrete problem. In the present work this are partial differential equations (e.g. Navier-Stokes equations). The Galerkin method is the basis for the finite element method and is used to transform a *strong form* formulation into a *weak form* formulation of a PDE. This is needed by the ENTWIFE preprocessor called ENTCODE (see. subsection 1.5.4). For sufficient often differentiable function f defined on the open set S the strong form would be (1.15).

$$L(x, \partial) f(x) = 0, \ \forall x \in S \tag{1.15}$$

After multiplication with every smooth test function ϕ with compact support in S and integration a weak solution (1.16) would be the result.

$$\int_S f(x) L(x, \partial) \phi(x) dx = 0, \ \forall x \in S \tag{1.16}$$

For the axisymmetric case, which was considered for calculations in chapter 2 and 4, all variables are independent of the azimuthal coordinate, i.e. φ (see (1.17)).

$$f = f(r, z), \qquad f = \vec{v}, T, p \tag{1.17}$$

For the transition from the strong form to the weak form, first the governing equations and boundary conditions have to be written in cylindrical coordinates (r, φ, z). In case of the fluid flow these are the Navier-Stokes equations (1.18, 1.19) with the Boussinesq approximation (1.20).

$$u\frac{\partial u}{\partial r} + w\frac{\partial u}{\partial z} - \frac{v^2}{r} = -\frac{1}{\rho}\frac{\partial p}{\partial r} + \nu(\Delta u - \frac{u}{r^2}) \tag{1.18}$$

$$u\frac{\partial v}{\partial r} + w\frac{\partial v}{\partial z} - \frac{uv}{r} = \nu(\Delta v - \frac{v}{r^2}) \tag{1.19}$$

$$u\frac{\partial w}{\partial r} + w\frac{\partial w}{\partial z} = -\frac{1}{\rho}\frac{\partial p}{\partial z} + \nu\Delta w + g\beta(T - T_0) \tag{1.20}$$

Here, $\Delta = \nabla^2 = \frac{1}{r}\frac{\partial}{\partial r}(r\frac{\partial}{\partial r}) + \frac{1}{r^2}\frac{\partial^2}{\partial \varphi^2} + \frac{\partial^2}{\partial z^2}$ is the Laplacian operator, u,v,w are flow velocity components, p is the hydrodynamic pressure, ρ is the density, g the gravitational accelleration, ν is the kinematic viscosity, T is the temperature and T_0 is the reference temperature, respectively.
By integration of (1.18−1.20) and multiplying with weighting function Φ the weak form becomes (1.21).

$$\begin{aligned} &\int\int \left[u\frac{\partial u}{\partial r} + w\frac{\partial u}{\partial z} - \frac{v^2}{r} + \frac{1}{\rho}\frac{\partial p}{\partial r} + \nu(\Delta u - \frac{u}{r^2})\right]\Phi_u r dr dz \\ &\quad + \int\int \left[u\frac{\partial v}{\partial r} + w\frac{\partial v}{\partial z} - \frac{uv}{r} - \nu(\Delta v - \frac{v}{r^2})\right]\Phi_v r dr dz \\ &+ \int\int \left[u\frac{\partial w}{\partial r} + w\frac{\partial w}{\partial z} + \frac{1}{\rho}\frac{\partial p}{\partial z} + \nu\Delta w + g\beta(T - T_0)\right]\Phi_w r dr dz = 0 \end{aligned} \tag{1.21}$$

1.5.3 Approaches in bifurcation methods

From a graphical point of view bifurcation means a branching of a structure (see. fig. 1.13). But why is it suggestive to apply the bifurcation in mathematics, which describes physical problems arising in crystal growth?
In systems, which can be described using linear dynamics (e.g. ordinary differential equations), all solutions can be built from fundamental solutions. But, there are no fundamental solutions in non-linear dynamics. In most cases no analytic solution is possible and thus there is no a-priori knowledge about the solution structure. In fact dynamic systems often show a complex solution manifold and ambiguity. Therefore it is not reasonable to obtain an overview of the global solution of a non-linear system using the direct numerical simulation [30]. Additionally, the direct numerical simulation can miss important solution branches of the non-linear dynamic system. So, before starting a deep analysis of a system it is important to detect parameter

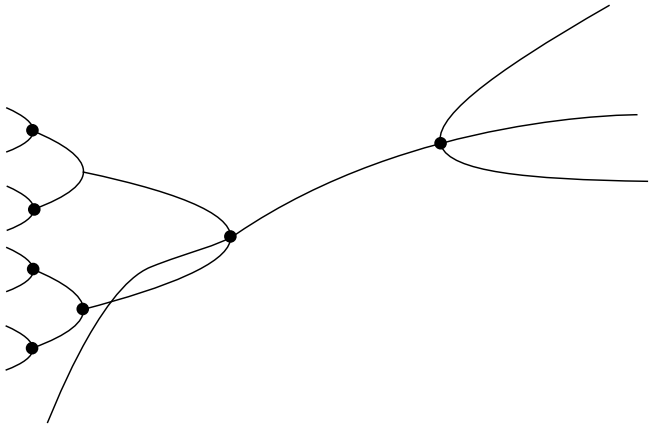

Figure 1.13: Sketch of a bifurcation example.

values, which lead to system instability, in order to decrease computational efforts. This analysis can be performed using bifurcation methods [63, 65, 66, 83] and should help to answer the following questions:

- What is the qualitative solution behaviour of the system?
- Which and how many invariant sets do occur?
- Which of them are un/stable?
- How behave invariant sets while changing the control parameter(s) of the system?

Bifurcation and branching processes correspond to a qualitative change of the system [84]. Further examples are the electrical membrane potential of nerves or fluttering of a flag, but the undesired spiral patterns during crystal growth [1, 30], also.
The mathematics behind bifurcation analysis is very complex and complicated [63, 65, 85]. There are different types of local bifurcation, which are listed below:

- saddle node bifurcation / fold bifurcation
- transcritical bifurcation
- pitchfork bifurcation
- period doubling bifurcation / flip bifurcation
- Hopf bifurcation
- Neimark bifurcation / secondary Hopf bifurcation.

Local bifurcations can be analysed entirely by changes of the local stability properties, i.e. changes of equilibria/fixed points, periodic orbits or other invariant sets of parameters which exceed critical thresholds. By contrast, the global bifurcations occur when larger invariant solution sets of the system

compete with each other [83]. They cannot be detected purely through a stability analysis of the fixed points. This work was mainly dealing with the analysis of Hopf bifurcation, fixed points and limit cycles [63, 65, 85, 86] in chapters 2 and 4. There are two types of Hopf bifurcation, supercritical (fig. 1.14) and subcritical bifurcation (fig. 1.15).

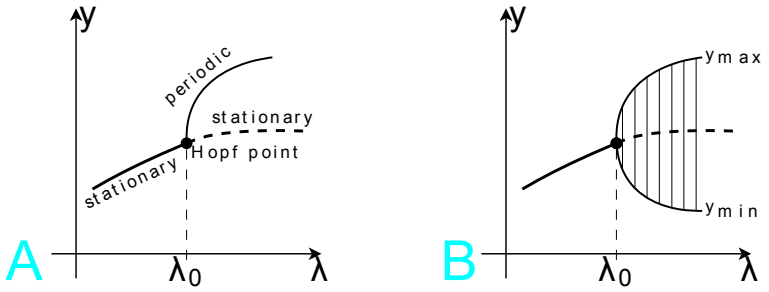

Figure 1.14: Sketch of different supercritical Hopf bifurcations [87].

y is representing the solution of the dynamical system (e.g. the kinetic energy of the Cz melt flow) and λ is the control parameter (e.g. the rotational Reynolds number Re). λ_0 is a critical threshold value of the system. The type of the bifurcation depends on the change direction of the control parameter [83]. Defining an increasing control parameter λ "supercritical" means that the solution orbits occur after the onset of bifurcation and "subcritical" means that the solution orbits occur before the onset of bifurcation.

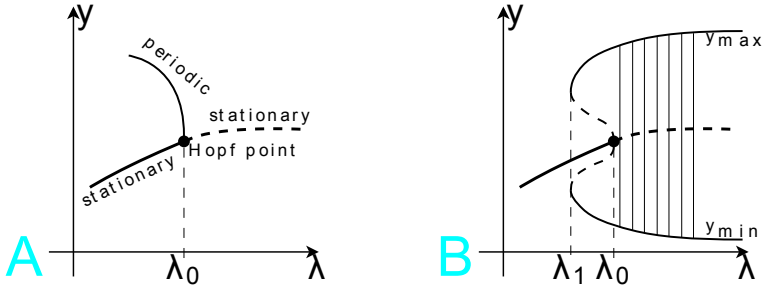

Figure 1.15: Sketch of different subcritical Hopf bifurcations [87].

In fig. 1.14 (A) the branch of stationary solutions extends itself beyond the critical value λ_0, which is not stable for $\lambda > \lambda_0$. The point for $\lambda = \lambda_0$ is called Hopf bifurcation point. Applying an analysis of the stability of systems equilibrium, which leads to an extensive eigenvalue problem, the bifurcation point and its type is found [30, 31, 65]. At this point the Jacobian has at least one pair of eigenvalues with a zero real part [65]. At the Hopf point a branch of periodic solutions arises, i.e. periodic orbits. These are

illustrated as vertical lines in fig. 1.14 (B). In the phase space the periodic orbits form a paraboloidal similar shape. Decreasing the control parameter λ both branches merge at the Hopf point to one stationary solution and the amplitude of the periodic orbits vanishes.
Fig. 1.15 (A) shows the subcritical case for which locally no stable solution exist for $\lambda < \lambda_0$. But, globally this local situation of fig. 1.15 (A) often extends itself to the case in fig. 1.15 (B). The branches of unstable periodic orbits bend back and so boost the stability for $\lambda > \lambda_1$. For $\lambda_1 < \lambda < \lambda_0$ the system is even "bistable". The analysis of such multiple solutions occurring during the Cz crystal growth was done in chapters 2 and 4.

Methodology for computing continuation diagrams

The ENTWIFE software package (see section 1.5.4) allows for calculating solution paths using the pseudo-arclength method introduced in [88]. Considering the nonlinear system

$$\boldsymbol{F}_h\left(\boldsymbol{x}_h, \lambda\right) = \boldsymbol{0} \qquad \boldsymbol{x} \in \mathbb{R}^N, \lambda \in \mathbb{R}, \tag{1.22}$$

where is assumed, that $\boldsymbol{F}_h$ is the result of the discretization of a nonlinear partial differential equation (PDE). The subscript $_h$ which denotes the discretization of a system is not used in the following for easier reading of equations. A solution set S given by

$$S := \left\{(\boldsymbol{x}, \lambda) \in \mathbb{R}^{N+1} \ : \ \boldsymbol{F}\left(\boldsymbol{x}, \lambda\right) = \boldsymbol{0}\right\} \tag{1.23}$$

is calculated by finding a discrete set of points on S. Taking $(\boldsymbol{x}_0, \lambda_0)$ as an initial guess, a point close to $(\boldsymbol{x}_0, \lambda_0)$ can be computed by the Newton's method, if ${\boldsymbol{F}_{\boldsymbol{x}}}^0 = \boldsymbol{F}_{\boldsymbol{x}}\left(\boldsymbol{x}_0, \lambda_0\right)$ is nonsingular. In this case $\boldsymbol{F}\left(\boldsymbol{x}, \lambda_1\right) = \boldsymbol{0}$ is solved, where $\lambda_1 = \lambda_0 + \Delta\lambda$ with a steplength $\Delta\lambda$. According to the implicit function theorem the Newton's method will converge for sufficiently small $\Delta\lambda$. At a fold point on S this simple method will fail [65]. This is the reason why the pseudo-arclength method is introduced in [88]. Considering an arc on S (see fig. 1.16) smooth and containing either regular points or fold points, there is an unique tangent vector $\boldsymbol{\tau}$ at each point of this arc. Letting t be a parameter describing the arc with $(\boldsymbol{x}(t), \lambda(t)) \in S$, the unit tangent at $(\boldsymbol{x}_0, \lambda_0)$ is denoted by $\boldsymbol{\tau}_0 = \left(\frac{d\boldsymbol{x}}{dt}(0), \frac{d\lambda}{dt}(0)\right) := \left[\boldsymbol{c}^T, d\right]^T$. The differentiation of $\boldsymbol{F}\left(\boldsymbol{x}(t), \lambda(t)\right) = \boldsymbol{0}$ with respect to t results in 1.24.

$$\boldsymbol{F}_{\boldsymbol{x}}\left(\boldsymbol{x}(t), \lambda(t)\right) \frac{d\boldsymbol{x}}{dt}(t) + \boldsymbol{F}_{\lambda}\left(\boldsymbol{x}(t), \lambda(t)\right) \frac{d\lambda}{dt}(t) = \boldsymbol{0} \tag{1.24}$$

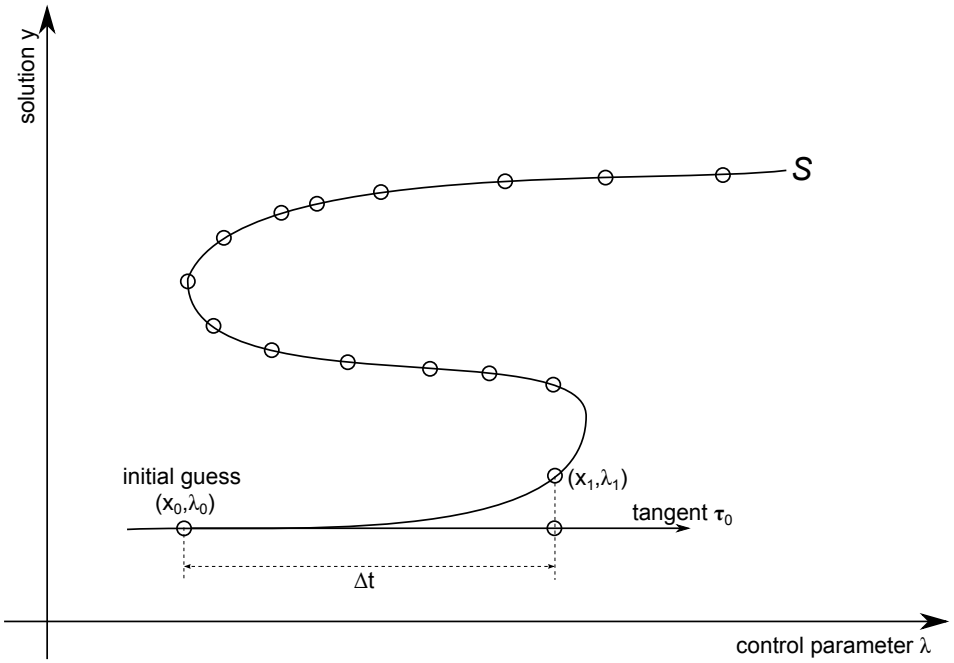

Figure 1.16: Solution set S with a tangent.

Using the unit tangent vector $\boldsymbol{\tau}_0$ and 1.24 an extended system can be defined as

$$\boldsymbol{H}\left(\boldsymbol{y},t\right)=\left[\begin{array}{c}\boldsymbol{F}(\boldsymbol{x},\lambda)\\ \boldsymbol{G}(\boldsymbol{x},\lambda,t)\end{array}\right]=\boldsymbol{0}, \tag{1.25}$$

where is $\boldsymbol{y}=(\boldsymbol{x},\lambda)\in\mathbb{R}^{N+1}$ and $\boldsymbol{G}(\boldsymbol{x},\lambda,t)=\boldsymbol{c}^T(\boldsymbol{x}-\boldsymbol{x}_0)+d(\lambda-\lambda_0)-\Delta t$ is a plane perpendicular to the unit tangent vector $\boldsymbol{\tau}_0$ in a distance $\Delta t=(t-t_0)$ from t_0 (see fig. 1.16). 1.25 is a projection of $(\boldsymbol{x},\lambda)$ onto the tangent vector $\boldsymbol{\tau}_0$ at $\boldsymbol{y}_0=(\boldsymbol{x}_0,\lambda_0)$, so that $\boldsymbol{H}_{\boldsymbol{y}}(\boldsymbol{y}_0,t_0)=\left[\begin{array}{cc}\boldsymbol{F}_{\boldsymbol{x}}{}^0 & \boldsymbol{F}_\lambda^0\\ \boldsymbol{c}^T & d\end{array}\right]$. Since $\boldsymbol{\tau}_0\perp\boldsymbol{G}$ and $\boldsymbol{\tau}_0\perp\left[\boldsymbol{F}_{\boldsymbol{x}}{}^0,\boldsymbol{F}_\lambda^0\right]$, $\boldsymbol{H}_{\boldsymbol{y}}(\boldsymbol{y}_0,t_0)$ is nonsingular and according to the implicit function theorem there exist solutions for $\boldsymbol{H}(\boldsymbol{y},t)=\boldsymbol{0}$ for t close to t_0. For sufficiently small Δt the Newton's method will converge resulting in results which are points in the plane $\boldsymbol{G}$. Because this solution path method is taking the length along the tangent vector $\boldsymbol{\tau}_0$ at the point $(\boldsymbol{x}_0,\lambda_0)$ as a parameter, it is called pseudo-arclength continuation [88]. In summary it is a "predictor/corrector-method" approaching along the tangent vector $\boldsymbol{\tau}$ with steps of the length Δt to predict a point $(\boldsymbol{x},\lambda)$, which is corrected by solving 1.25 by Newton's method. The applied pseudo-arclength continuation is described more detailed in [65] and in references cited therein.

The fig. 1.17 is used to explain the methodology for computing continuation diagrams with the ENTWIFE software package. It plots the solution of the system (e.g. Czochralski melt flow) against values of a control parameter. Typically, for Czochralski melt flow it is the rotational Reynolds number corresponding to the crystal rotation rate and the temperature difference over the free melt surface corresponding to the thermal gradients in the melt.
Due to the strong non-linearity of a Czochralski melt flow system, usually it is not possible to compute a continuation diagram with a single run of ENTWIFE. The solution "a" is carried out for a very small control parameter, where the system is slightly non-linear, only. The subsequent solutions are then computed with a fixed parameter step size ending the first software run in the solution "b". There the solver fail to converge for higher values indicating either a too large parameter step or a limit point.

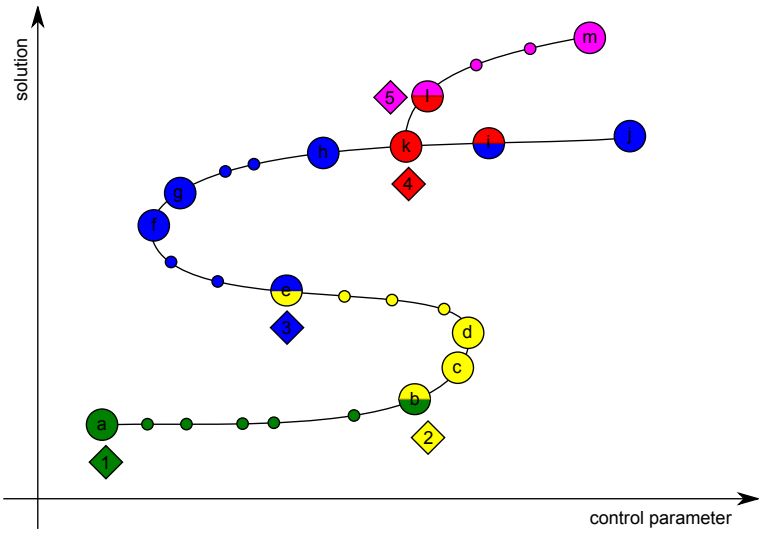

Figure 1.17: Sketch of computing a continuation diagram.

In the second software run the solution "b" is recomputed using the pseudo-arclength continuation [65, 89, 90]. The parameter step size is adjusted automatically. In this way the solutions "b" to "e" are obtained. The Jacobian determinant was positive for solutions "a" to "c", but it changes its sign to negative for solutions "d" to "e". This indicates a change in the stability of the solution, i.e. a limit point is located between solutions "c" and "d".
During the third run the solution at "e" is restarted with the pseudo-arclength continuation algorithm and solutions "e" to "j" are obtained. The sign of the Jacobian determinant changes from negative to positive between "f" and "g". This is corresponded with a change of stability and a limit point close to "f". Further change in sign of the Jacobian determinant occures between "h" and

"i", which is connected to a possible bifurcation of a new branch of solutions. Therefore the solution "p" is used as initial guess for the ENTWIFE algorithm for locating bifurcation points. This converges at the bifurcation point at "k". In the last software run the solution is restarted at "k" and the solution "l" is found. Subsequently, the continuation algorithm computes the solutions "l" to "m".

1.5.4 The ENTWIFE software package

In the present work ENTWIFE [80, 81, 91] was used for numerical calculations. It is a finite-element (FEM) software package for solving systems of second-order differential equations (problems of laminar fluid flow and heat transfer) and is written in FORTRAN. In addition to a built-in equation library relating to fluid flow and heat transfer processes, ENTWIFE accepts user defined equations, which allow for solving any set of user supplied equations of the above mentioned type. This is an important advantage in contrast to other similar software packages, which can only solve built-in equations.
ENTWIFE supports the analysis of nonlinear problems that may show bifurcation phenomena. Different solution branches, various bifurcation points, and paths of bifurcation points can be computed. The stability of previously computed solutions using eigenvalue techniques can be examined. The main features of the ENTWIFE package are listed below:

- mixed physics modelling of non-linear systems in one, two or three dimensions
- grid generation includes local refinement, deletion, redistribution, bisection, element re-numbering and matching to complicated boundaries
- over 50 different finite element types
- different time-stepping algorithms including Crank-Nicolson and Gear's method
- bifurcation algorithms including the determination of Hopf-Points (periodic orbits)
- many output options including plots of vectors, tensors, contours, streamlines and pathlines in 2D and 3D as PostScript files.

ENTWIFE is used in connection with the pre-processor ENTCODE, which provides an interface to algebra packages (Mathematica [92] and Maple [93]). It allows to work with almost any set of equations written as weak form. The external algebra package helps for generating FORTRAN subroutines,

which determine the corresponding Jacobian, which is needed by the Newton-Raphson iteration within the ENTWIFE package. Fig. 1.18 shows the principle procedure for application of the ENTWIFE package.

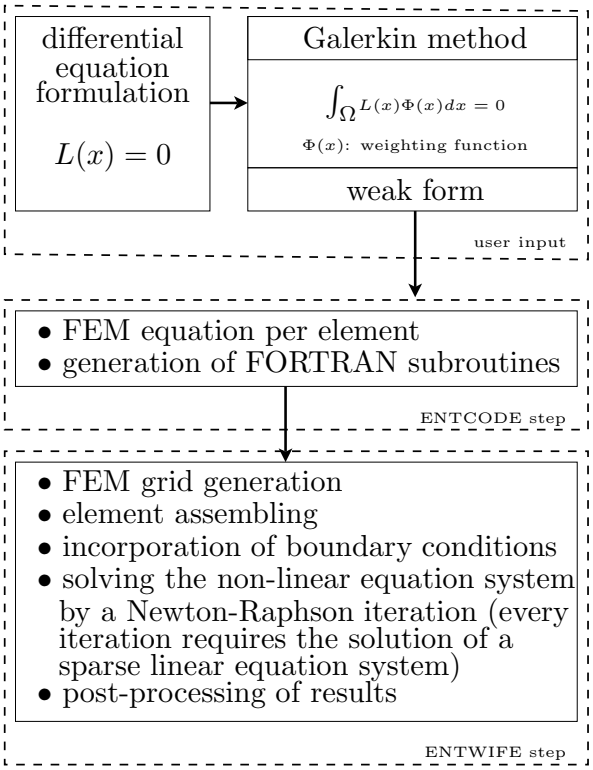

Figure 1.18: Principle ENTWIFE procedure.

ENTWIFE (release 7.3) runs under different UNIX based operating systems, e.g. Solaris or Linux. After copying and uncompressing the ENTWIFE package, it has to be recompiled for the target platform. For this purpose the best compiler optimization switches should be set, because this way the performance can be increased considerably. This depends strongly on the used hardware, especially the kind of cache and main memory management. Setting proper compiler switches about 3-5 times faster simulation runs could be performed. Detailed installation instructions of ENTWIFE can be found in [91].
ENTWIFE is controlled by an input data file, which has a logical tree-like structure using the special free-format structured input language TGIN [94]. The input data is divided into commands and keyword data. Commands correspond to options and keyword data correspond to numerical data input for a given option. Thereby, the command may have subcommands and the

order of commands is important.
Very detailed description of all ENTWIFE features can be found in [81]. Beside many advantages the main disadvantage of ENTWIFE is the missing graphical user interface, which makes the modelling step as well as the interpretation step of calculated results uncomfortable. The input data files can be very large, especially for complex geometries and if a deep interpretation of results is needed. But the fact, that all names of commands and keywords are self-explanatory makes the generation of input files easier. The main advantage of ENTWIFE is the extension possibility. So, it is extended with an interface to the MUMPS solver (MUltifrontal Massively Parallel Solver) [82], which makes the solution of large problems very efficient. The disadvantage of this solver is the need of very large main memory size, which increases rapidly with the grid size and number of processors.
In this work ENTWIFE was used for the calculation of all governing equations of the modelled problems. The discretized equations were solved using a Newton-Raphson method [79] in connection with the direct solver MUMPS. For time dependent equations the Crank-Nicolson algorithm [79] as well as Gear's method [95], which provides adaptive time-stepping, was used.

Chapter 2

Numerical analysis of a simplified crystal growth process

2.1 Verification of the applied numerical code

Before modelling a real Czochralski (Cz) system using $DyScO_3$ properties, the applied numerical code had to be verified. For the studies performed in this work the influence of a baffle, of the solid/liquid interface form, of the free surface form or of other parts of a real Czochralski setup (see fig. 1.2 in chapter 1) are important. However, for verifying the applied numeri-

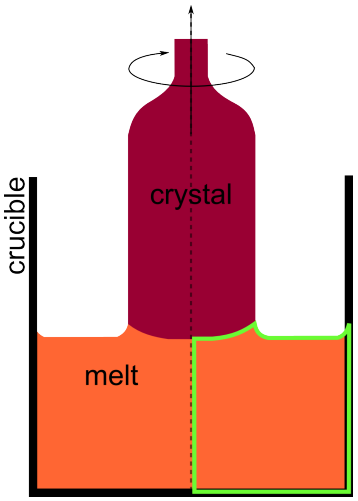

Figure 2.1: Simplification of the Czochralski (Cz) process by exploiting the axial symmetry.

cal code the model was simplified. Fig. 2.1 shows the simplification of the Cz process. Only the melt domain was considered. By exploiting the axial symmetry of the setup only one half of this domain had to be taken into account (green marked domain in fig. 2.1). Furthermore, the melt has been considered as a rectangle. The simulated hydrodynamic model of the Cz melt flow is shown in fig. 2.2. It considers flow in a non-uniformly heated cylindrical crucible, driven by buoyancy convection, thermocapillary convection and crystal rotation, governed by the Navier-Stokes equations in the Boussinesq approximation, the continuity and the temperature equation, respectively (see [30, 96]). Boundary conditions were set for the symmetry axis, the melt-crystal interface, the free melt surface, the crucible wall and the crucible bottom as well. The right part of fig. 2.2 shows an example of the applied grid containing 24x24 Q9/4 elements. However, grids with up to 200 elements of the same type in each direction were applied. Using non-equidistant distribution the density of elements was higher at the symmetry axis, at the crucible bottom, at the melt/crystal interface and at the free melt surface in order to increase the spatial accuracy there. Further

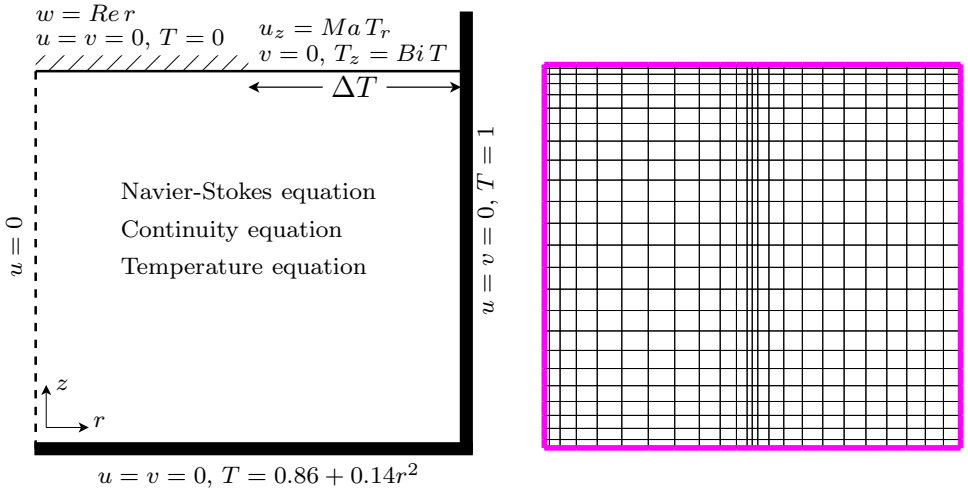

Figure 2.2: Simplified Cz model with corresponding boundary conditions and applied grid (right).

simplifications of the model were flat solid/liquid interface and flat free melt surface. Effects of radiative heat transfer were not considered in this model. The parabolic boundary condition of the temperature at the bottom of the crucible was derived from experimental measurements [35]. The used dimensionless parameters were the Grashof number Gr (2.1), the Prandtl number Pr (2.2), the modified Marangoni number Ma (2.3), the Marangoni number

Mn 2.4, the rotational Reynolds number Re (2.5), the Biot number Bi (2.6) and the aspect ratio Ar (2.7) of the crucible height H to its radius R.

$$Gr = \frac{g\beta\Delta T R^3}{\nu^2} \tag{2.1}$$

$$Pr = \frac{\nu}{\chi} \tag{2.2}$$

$$Ma = \frac{\left|\frac{d\sigma}{dT}\right| \Delta T R}{\eta\nu} \tag{2.3}$$

$$Mn = Ma\, Pr \tag{2.4}$$

$$Re = \frac{\omega R^2}{\nu} \tag{2.5}$$

$$Bi = \frac{h\, R}{\lambda_m} \tag{2.6}$$

$$Ar = \frac{H}{R} \tag{2.7}$$

The model in fig. 2.2 considers a melt flow with kinematic viscosity ν, density ρ and thermal diffusivity χ in a cylindrical crucible $0 \leq r \leq R$, $0 \leq z \leq H$, where r,z are cylindrical coordinates. The temperature dependence of the surface tension $\gamma = \frac{d\sigma}{dT}$ was assumed to be linear. For the non-dimensionalization scalings of (2.8) were applied. Additional scalings R^2/ν and $\rho(\nu R)^2$ for time and pressure, respectively, were used.

$$r := \frac{r}{R} \quad z := \frac{z}{R} \quad u := \frac{uR}{\nu} \quad T := \frac{T - T_m}{T_c - T_m} = \frac{T - T_m}{\Delta T} \tag{2.8}$$

The Grashof and Marangoni number were defined using the temperature difference ΔT (measured in K) between the crucible wall and the crystal with the crucible radius chosen as the characteristic length (see (2.8)). This way it was easier to alter the crystal radius as was done in the recent experiments of Teitel, Schwabe and Gelfgat [97]. For each model boundary certain conditions for the flow velocity and the melt temperature have to be fulfilled. At the symmetry axis the r-component and at the melt free surface the z-component of the velocity vector vanishes. At other boundaries the r- and the z-component were zero. At the liquid/solid interface, i.e. melt/crystal interface, the crystal, which was vertical to the melt surface, was being rotated and has influenced the melt flow velocity in the φ-direction. At this boundary the condition for the temperature was normalized to zero, while their maximum was located at the crucibles wall ($r = 1$). For the crucible bottom an experimentally determined parabolic temperature distribution was

set. The influence of the thermocapillary convection at the free melt surface was modelled by the Marangoni number. All other influences which are available at the free melt surface, such as gas convection and other energy dissipative influences were described comprehensively by the Biot number. This boundary condition $\frac{\partial T}{\partial z} = Bi\,T$ at the free melt surface assumes that the ambient temperature is equal to the temperature at the melt/crystal interface. This assumption is wrong for real crystal growth conditions, but it corresponds to the model experiments done in [35]. For the verification of the numerical code properties of a sodium nitrate ($NaNO_3$) melt, which are well known [35], were used (see tab. 2.1). Defining $\Delta T = T_c - T_m$ as the temperature difference between the crystal and the crucible wall, and using the material and geometric data given in [35], the governing parameters were $Pr = 9.2$, $Ar = 0.92$, $R_c = 0.5$ (crystal to crucible radii ratio), $Bi = 0.1$, $Gr = 1.90476 \cdot 10^5\,\Delta T$ and $Ma = 5.8571 \cdot 10^2\,\Delta T$ (see tab. 2.1). Here ΔT was measured in K. In the following calculations the dimensional temperature difference ΔT was considered as a critical parameter, since both important parameters, Grashof and Marangoni number, depend on ΔT (see (2.1) and (2.3)). An additional critical parameter was the rotational Reynolds number Re, which corresponds to the crystal rotation rate Ω. The applied numerical

Property	**Symbol**	**Value**	**Units**
melting point	T_m	307	K
density	ρ	1.904	$g\,cm^{-3}$
temperature dependence of ρ	$d\rho/dT$	$-1.25 \cdot 10^{-3}$	$g\,cm^{-3}\,K^{-1}$
dynamic viscosity	η	$2.78 \cdot 10^{-2}$	$g\,cm^{-1}\,s^{-1}$
kinematic viscosity	ν	$1.46 \cdot 10^{-2}$	$cm^2\,s^{-1}$
surface tension	σ	119	$g\,s^{-2}$
temperature dependence of σ	$\gamma = \frac{d\sigma}{dT}$	$-5.1 \cdot 10^{-2}$	$g\,s^{-2}\,K^{-1}$
specific heat capacity	c_p	1.88	$J\,g^{-1}\,K^{-1}$
thermal diffusivity	χ	$1.58 \cdot 10^{-3}$	$cm^2\,s^{-1}$
vol. expansion coefficient	β	$6.6 \cdot 10^{-4}$	K^{-1}
thermal conductivity (melt)	λ_m	$5.65 \cdot 10^{-3}$	$W\,cm^{-1}\,K^{-1}$
thermal cond. (solid $\approx$ 200°C)	λ_s	$7.5 \cdot 10^{-3}$	$W\,cm^{-1}\,K^{-1}$
Prandtl number	Pr	9.2	–
Marangoni number	Ma	$5.8571 \cdot 10^2\,\Delta T$	–
Grashof number	Gr	$1.90476 \cdot 10^5\,\Delta T$	–
Biot number	Bi	0.1	–

Table 2.1: Sodium nitrate ($NaNO_3$) melt properties taken from [35].

approach was based on a finite element discretization containing up to 200 x 200 nonuniform quadrilateral elements with biquadratic interpolation for

the velocity and temperature field and bilinear interpolation for the pressure (Q9/4 elements). The advanced FEM package ENTWIFE [80] has been used for solving this problem. The calculated results were compared with results of the Israeli research group for the same model problem, but using another numerical code (see [1]). This approach uses a finite volume code, which was also of second order accuracy and had used staggered and stretched grids with up to 1000x1000 nodes. Both codes allows for direct calculation of steady flow states and time-dependent solutions. For the following calculations the parameters listed in table 2.2 and the simple grid shown in fig. 2.2 were used.

Description	**Symbol**	**Value**	**Units**
crucible radius	r	38	mm
crucible height	h	60	mm
crystal radius	r_c	19	mm
melt height	h_m	55.2	mm
normalized melt height	H	0.92	–
normalized crucible radius	R	1.0	–
crucible aspect ratio	Ar	0.92	–
crystal to crucible radii ratio	R_c	0.5	–
gravity	g	9.81	m/s^2
crystal rotation	Ω	0..30	1/min
angular frequency	$\omega = 2\pi{\cdot}\Omega$	0..188	1/min
rotational Reynolds number	$\approx 100 \cdot \Omega$	0..3000	–

Table 2.2: Operating parameters used for calculations of the sodium nitrate ($NaNO_3$) melt flow.

2.1.1 Steady state simulations

The parameters temperature difference across the free melt surface ΔT, which is incorporated into the Grashof and Marangoni number, and the rotational Reynolds number Re influence the driving forces of the melt flow. Therefore these parameters were varied during the following calculations. Fig. 2.3 shows calculated steady state melt flows for $\Delta T = 1.0K$ and $Re = 0$ (a), $Re = 1000$ (b) and $Re = 5000$ (c). The frames in the left column of fig. 2.3 are contour plots of the stream function. The frames in the middle column show the isotherms in the melt and the frames in the right column show the distribution of the azimuthal velocity. The left border of each frame corresponds to the symmetry axis. All lines are equidistant between the max-

imum and minimum values. These steady state results were also calculated by the Israeli research group (see [1]) applying the finite volume method on a 200x200 streched grid. The results shown in fig. 2.3 are qualitatively the

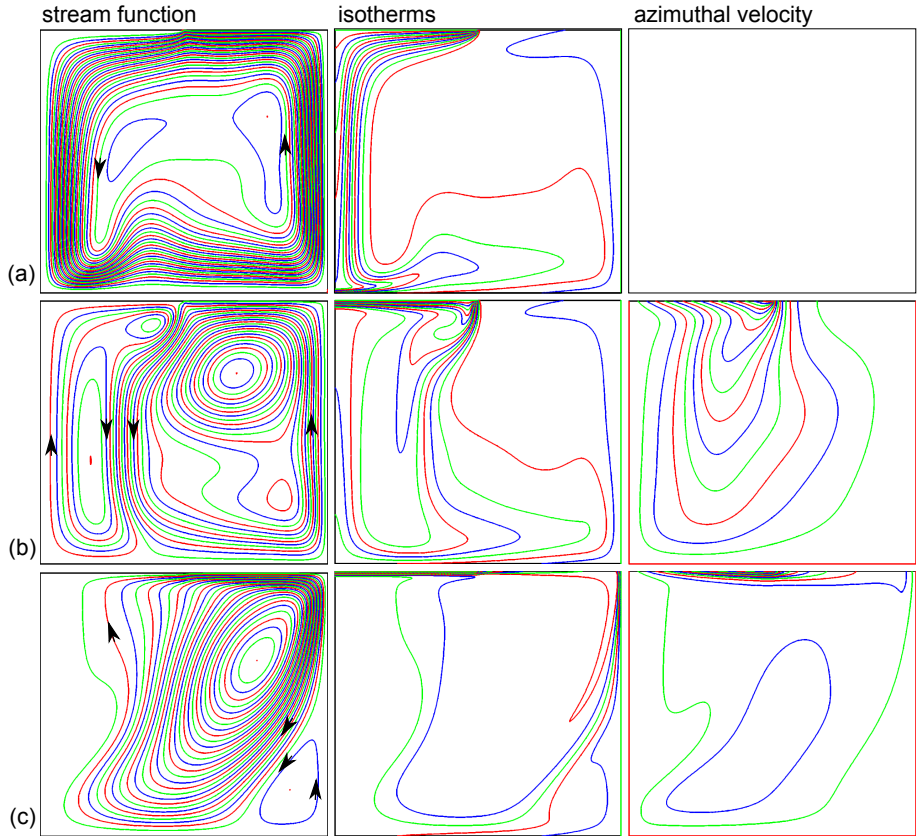

Figure 2.3: Streamlines, isotherms and azimuthal velocity for $\Delta T = 1K$ and (a) $Re = 0$, (b) $Re = 1000$ and (c) $Re = 5000$.

same compared to the results of the Israeli research group [1], which indicate that the two independent codes (FVM, FEM) deliver the same results for the same problem. Tab. 2.3 is showing a quantitative comparison of the characteristic melt flow properties. These are the minimum and maximum values of the stream function at their locations $\Psi_{min/max}(r, z)$, the minimum and maximum values of the radial velocity at the cross section $r = 0.5$, i.e. at locations $u_{min/max}(r = 0.5, z)$, the minimum and maximum values of the axial velocity at the cross section $z = 0.5\,Ar$ at their locations $w_{min/max}(r, z = 0.5\,, Ar)$, the total kinetic energy of the melt flow E_{kin} (2.9), the Nusselt numbers at all boundaries Nu_{bottom} (2.10), Nu_{wall} (2.11), $Nu_{crystal}$ (2.12) and $Nu_{surface}$ (2.13). Here, H is the melt height, R the crucible radius and R_c the radius of the crystal. The maximum and minimum values of the temperature are 0

and 1 and of the azimuthal velocity are 0 and Re, respectively.

$$E_{kin} = 2\pi \int_0^{HR}\int_0^{} \left(u^2 + v^2 + w^2\right) r dr dz \tag{2.9}$$

$$Nu_{bottom} = \int_0^R \left[\frac{\partial T}{\partial z}\right]_{z=0} r dr \tag{2.10}$$

$$Nu_{wall} = \int_0^H \left[\frac{\partial T}{\partial r}\right]_{r=1} dz \tag{2.11}$$

$$Nu_{crystal} = \int_0^{R_c} \left[\frac{\partial T}{\partial z}\right]_{z=H} r dr \tag{2.12}$$

$$Nu_{surface} = \int_{R-R_c}^R \left[\frac{\partial T}{\partial z}\right]_{z=H} r dr \tag{2.13}$$

$$Nu_{bottom} + Nu_{wall} + Nu_{crystal} + Nu_{surface} = 0 \tag{2.14}$$

It is seen that results obtained by the two codes are reasonably close. However, they did not coincided even within the second decimal digit. This indicates the influence of different discretization types, which also has affected the stability results shown later. When the crystal has not been rotated ($Re = 0$, fig. 2.3 (a)) the flow was driven by buoyancy and thermocapillary forces, which created an anti-clockwise convection. This anti-clockwise motion would be created by each of the two forces separately, so that the two driving mechanisms enhance each other. This flow pattern was characterized by an intensive descending flow near the axis. This region is interpreted sometimes as a "cold jet" and is a source of the experimentally observed so-called "cold plumes" and "cold jet" instabilities [35, 97]. There is also a velocity boundary layer near the crucible wall. These two regions with rapid variation in the velocity and temperature made the calculations very demanding with respect to the numerical accuracy. With the increase of crystal rotation the action of centrifugal forces could be observed, which had the tendency to create a circulation in the clockwise direction, opposite to the thermally induced convective circulation (fig. 2.3 (b)). With $Re = 1000$ the domain was splitted into two parts, the clockwise one located below the crystal, which was driven mainly by the centrifugal force, and the anti-clockwise one located below the free surface, which was driven mainly by buoyancy and thermocapillary forces. In this case the total kinetic energy and the total heat transfer through the crucible were both reduced compared to the case

of a non-rotating crystal (see tab. 2.3). Regions of a rapid variation of the velocity and temperature also have disappeared, which made the numerical calculations less demanding. It follows from tab. 2.3 that results obtained by the two codes were closer at $Re = 1000$ and $Re = 5000$ than at $Re = 0$. This seemingly surprising result was a consequence of a smearing of the bound-

Finite volume code (Israeli research group), stretched grid 200x200

Re	**0**	**1000**	**5000**
Ψ_{min}	-1.510	-2.070	-1.206
(r_{min}, z_{min})	$(0.8100, 0.3263)$	$(0.6900, 0.6797)$	$(0.8652, 0.1610)$
Ψ_{max}	0.0	0.7079	26.71
(r_{max}, z_{max})	–	$(0.1770, 0.4600)$	$(0.7500, 0.6087)$
$u_{min}(r = 0.5)/z_{min}$	$-36.55/0.9183$	$-33.94/0.9183$	$-145.8/0.05774$
$u_{max}(z = 0.5)/z_{max}$	$14.63/0.08736$	$11.83/0.08736$	$475.5/0.9075$
$w_{min}(z = 0.5)/r_{min}$	$-231.8/0.0$	$-35.52/0.2631$	$-157.5/0.8577$
$w_{max}(z = 0.5)/r_{max}$	$15.76/0.9477$	$124.4/0.0$	$192.9/0.4039$
E_{kin}	80.92	54.83	4262.0
Nu_{bottom}	1.575	1.499	0.7685
Nu_{wall}	1.246	1.185	7.306
$Nu_{crystal}$	-2.784	-2.647	-8.053
$Nu_{surface}$	-0.036	-0.037	-0.0215

Finite element code (German research group), 120x120 biquadratic elements

Re	**0**	**1000**	**5000**
Ψ_{min}	-1.502	-2.130	-1.203
(r_{min}, z_{min})	$(0.7904, 0.3246)$	$(0.6701, 0.6802)$	$(0.8696, 0.1597)$
Ψ_{max}	0.0	0.7102	24.85
(r_{max}, z_{max})	–	$(0.1798, 0.4501)$	$(0.7450, 0.6195)$
$u_{min}(r = 0.5)/z_{min}$	$-36.61/0.9013$	$-33.10/0.9104$	$-146.3/0.0611$
$u_{max}(z = 0.5)/z_{max}$	$15.02/0.0842$	$11.88/0.0860$	$478.3/0.9092$
$w_{min}(z = 0.5)/r_{min}$	$-232.2/0.0$	$-35.40/0.2603$	$-155.5/0.8595$
$w_{max}(z = 0.5)/r_{max}$	$15.78/0.9502$	$126.4/0.0$	$193.7/0.4014$
E_{kin}	83.92	55.89	4280.1
Nu_{bottom}	1.580	1.502	0.757
Nu_{wall}	1.231	1.155	7.352
$Nu_{crystal}$	-2.785	-2.634	-8.093
$Nu_{surface}$	-0.026	-0.023	-0.016

Table 2.3: Characteristic values for steady state flows at $\Delta T = 1K$ and different rotational Reynolds numbers Re.

ary layer and the "cold jet" region by rotation. At a very large Reynolds number the centrifugal force was dominant and the circulation has rotated clockwise (fig. 2.3 (c)). The flow pattern was similar to a so-called rotating disk − cylinder flow [98, 99]. At large rotation rates a dramatic change could be also observed in the shape of the isotherms caused by the strong effect of thermal convection. The total kinetic energy and the total heat transfer through the melt volume were dramatically increased. Obviously, this case should be considered as an extremum for the usual parameter values of oxide crystal growth. However, it is important for understanding the stability properties of the flow, as well as being another representative case for numerical benchmarking. Note also that the boundary layers developing near the crucible wall (2.3 (c)) again have required greater demands on the numerical computations.

2.1.2 Stability diagram by direct numerical simulation

Fig. 2.4 shows an example of the grid dependence study. With the help of the direct numerical simulation (DNS starts from an initial guess in order to obtain a steady state or time-dependent solution), which is very time consuming, two stability diagrams of the $NaNO_3$ melt flow in the Cz crucible were calculated for two different FEM grids. Every point on this curves shows

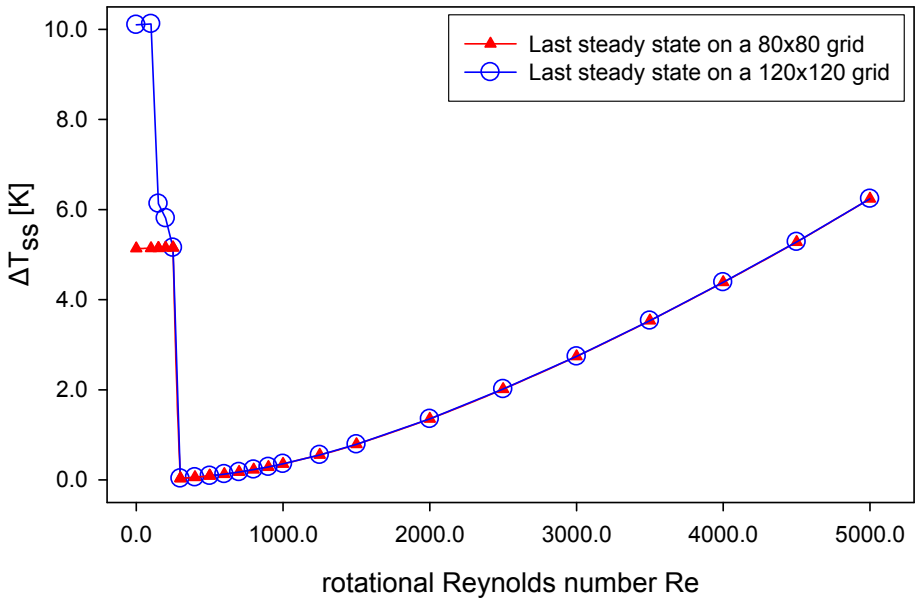

Figure 2.4: Grid dependence of the numerical solution for $NaNO_3$ melt flow applying a 80x80 and a 120x120 FEM grid, respectively.

the last converged steady state solution for a certain parameter combination on a given grid. It can be seen that for small rotational Reynolds numbers Re the numerical simulations of this kind are strongly grid dependent. Apparently, this is the effect of steep velocity and temperature gradients near the crucible axis and the boundary layer close to the crucible wall. To retain the numerical accuracy finer grids have to be used for small Re. The calculations for larger Re converge at coarser grids because the boundary layers smear due to the influence of the larger centrifugal force inhibiting the thermal flow.

2.1.3 Path following and multiplicity

The calculation of stability diagrams applying the direct numerical simulation is very time consuming. The main problem is, that it can happen that important information about the solution structure can be missed. However, it can give the first overview of the possible solutions. More reliable and much faster can be the introduction of path following techniques (see [65, 96]). Fig. 2.5 shows the comparison of path following results for the control

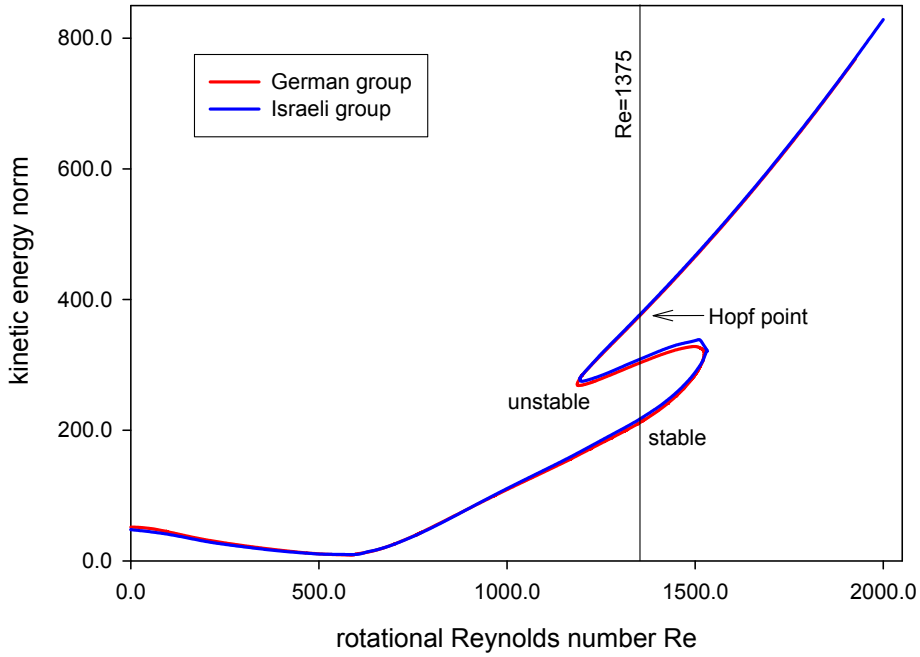

Figure 2.5: Continuation diagram for the control parameter Re for $\Delta T = 0.27K$.

parameter rotational Reynolds number Re. As solution the kinetic energy

norm (2.9) is plotted. The steady flows at melt free surface temperature difference $\Delta T = 0.27K$ and Re varied between 0 and 2000 were compared. The value of $\Delta T = 0.27K$ has been chosen, because there has been observed an oscillatory solution. Furthermore, also in [100] was shown experimentally, that oscillatory melt flow is possible for low ΔT. The first observation of fig. 2.5 shows that the path following curve is in very good agreement with the curve of the Israeli Group (see [1]). For $Re < 1200$ and $Re > 1600$ a single steady state solution exists. In the interval $1200 \leq Re \leq 1600$ two turning (limit) points can be observed. Within this interval the solution was not unique. Thus, for $Re = 1375$ (shown by a vertical line in fig. 2.5) the first solution with the smallest kinetic energy was stable, the next one was unstable and the third solution belonges to a Hopf bifurcation point, i.e. onset of an oscillatory instability, which we assume to be responsible for the onset of crystal spiral growth. It should be mentioned that multiple solutions appear for the values of Re characteristic for real crystal growth process ($10 \,..\, 20\, rpm$). For instance, $Re = 1375$ corresponds to the crystal rotation with the rotation rate of approximately $12\, rpm$ (see eq. (2.5)). It should also be mentioned that the value of $\Delta T = 0.27K$ was much smaller than that applied during the oxide crystal growth, since the thermal gradients are much higher (e.g. melting point of $DyScO_3 \approx 2000\,^{\circ}C$). Finally, it is stressed that the existence of multiple steady states and the dependence of the final state on the initial conditions is well-known for model fluid convection and rotating flow. Several examples can be found in the review paper [101]. To the best of our knowledge, the multiplicity of flow solutions of the CZ configuration has been reported for the first time.

2.1.4 Stability limits and unsteady flows

Stability curves corresponding to the oscillatory instability of steady state flows with respect to the axisymmetric perturbations are shown in fig. 2.6. The results (red curve) of the stability study were compared with results

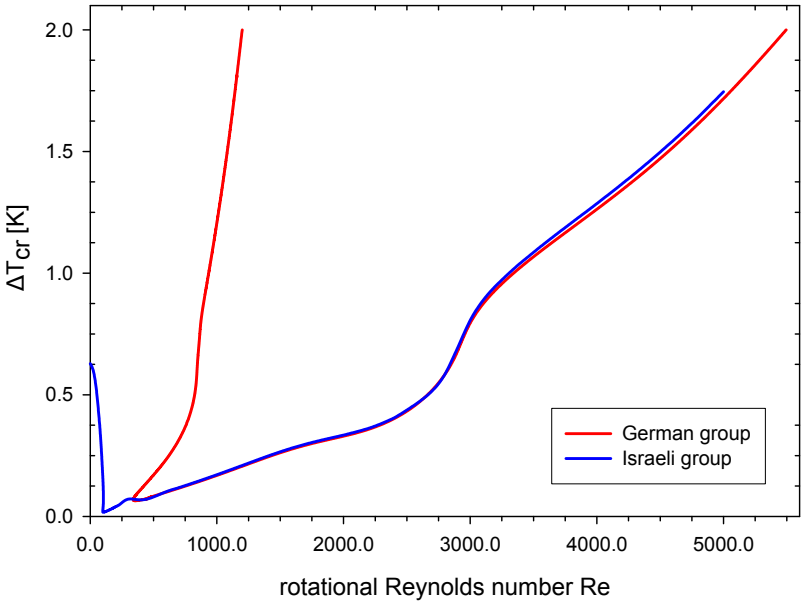

Figure 2.6: Stability curves for the critical temperature difference ΔT vs. rotational Reynolds number Re (published in [1]).

(blue curve) of the Israeli research group (published in [1]). Results corresponding to the three-dimensional perturbations can be found in [96]. Here the focus has been set mainly on the comparison exercise, which was started from the axisymmetric instability. The stability diagram in fig. 2.6 shows the critical temperature difference ΔT_{cr} for different rotational Reynolds numbers Re. Below the stability curve the melt flow was linearly stable and was unstable above the curve. The curves were plotted through calculated Hopf bifurcation points in which the leading eigenvalues of the linearized stability problem have appeared as conjugate complex pairs having zero real parts. Hopf bifurcation points are origins of oscillatory solution branches (periodic orbits). Good agreement could be obtained for $Re > 400$, which is very important since these Re are close to the real oxide crystal growth conditions, where crystal rotation rates vary between 5 and 25 rpm ($Re = 5000$ corresponds to $\approx 50\,rpm$, see eq. (2.5)). For small Re (< 400) the results disagree. In [1], the reasons for this disagreement were not completely resolved. It was stressed that calculations at zero and small Re are more difficult, which was

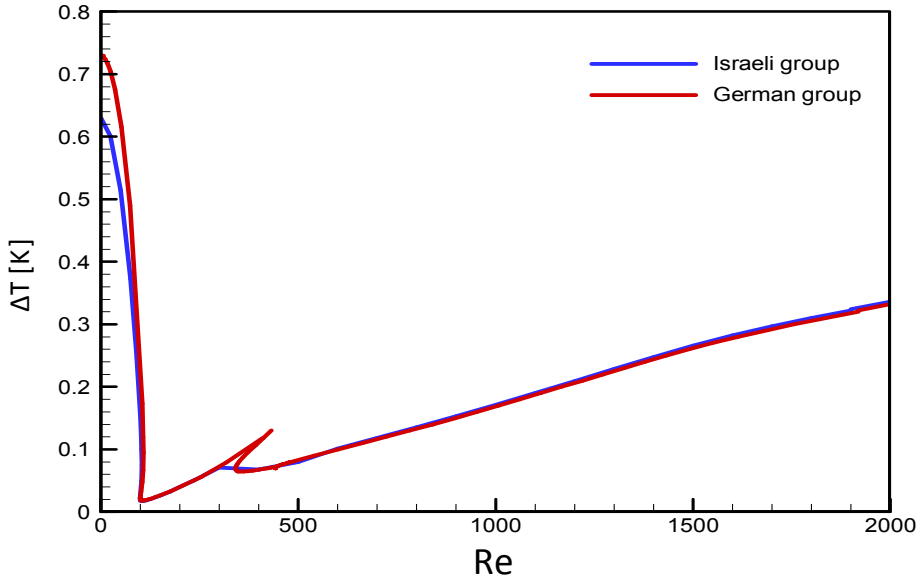

Figure 2.7: Stability curves for the critical temperature difference ΔT vs. rotational Reynolds number Re.

also reflected in the disagreement at that time. Possible reasons for the disagreement were grid dependence of different numerical approaches (FVM vs. FEM) or missing the most dangerous eigenvalues. The latter can occur, if the numerical approach does not find the eigenvalue λ with the largest real part $Real\,[\lambda(k)]$, where k is the wavenumber of the linear stability eigenproblem [96], e.g. if not enough wavenumbers k has been considered or approximative methods for eigenvalue analysis (e.g. Arnoldi method) has been used. It has been carried out that during the computation of the red curve the most dangerous eigenvalues were not found for small rotational Reynolds number Re, which was the main problem for the disagreement of results shown in fig. 2.6. Fig. 2.7 shows the new results (red curve), which are now in good agreement with the results of the Israeli group (blue curve) for $Re < 400$ (additional red curve), also. The red curve was calculated in two steps. The right part of the red curve ($Re > 400$) was computed decreasing the parameter Re. The left part of this curve ($Re < 400$) is calculated increasing the parameter Re. The intersecting set of both parts results in the red curve, which only disagree from the blue curve near $Re = 400$ and close to the axis. We assume that different grid dependence of different discretization types is the reason for this local disagreement. Especially, close to the axis, where the boundary layer flow is strong, grids have to be very fine.

2.1.5 Comparison of transient simulations

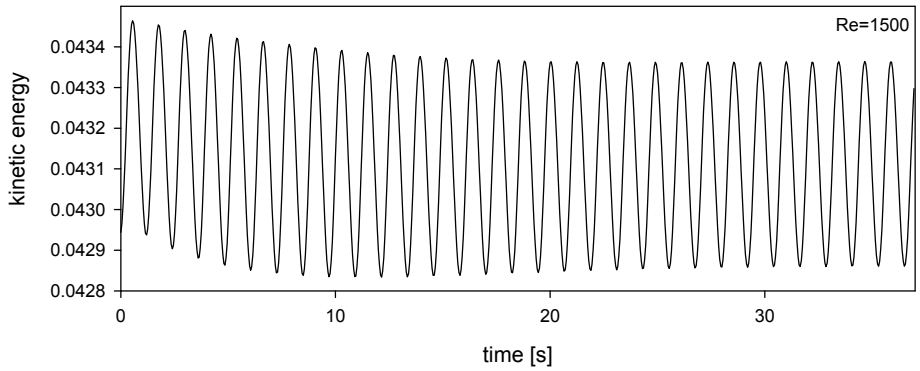

Figure 2.8: Transient simulation for $Re = 1500$ and constant $\Delta T = 0.27K$.

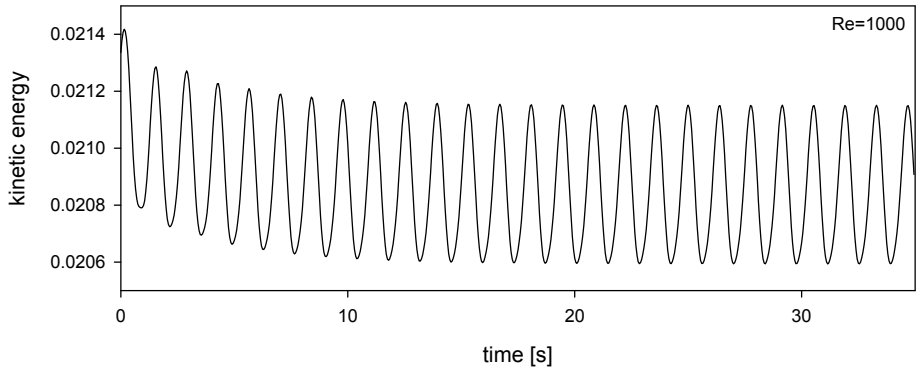

Figure 2.9: Transient simulations for $Re = 1000$ and constant $\Delta T = 0.27K$.

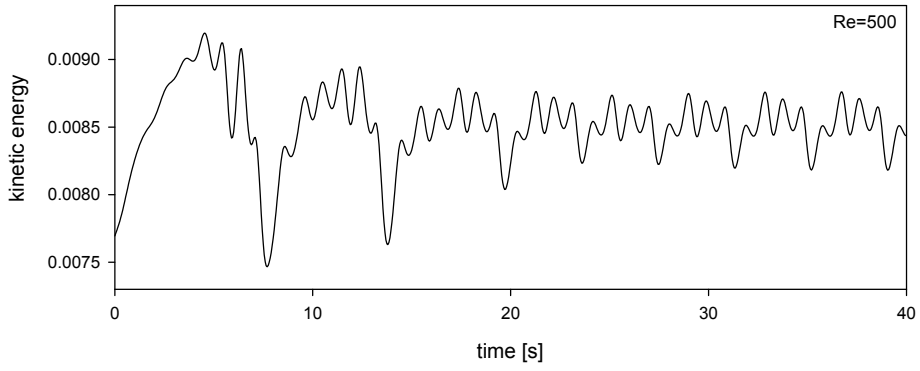

Figure 2.10: Transient simulations for $Re = 500$ and constant $\Delta T = 0.27K$.

In carrying out time dependent calculations one also has to consider the time step dependence. The Israeli group applied constant time steps [1]. Possible

effects of a too large time step were shown in [1], also. A too large time step leads to a time-asymptotical periodic solution that overestimates the oscillation amplitude and also affects its period.

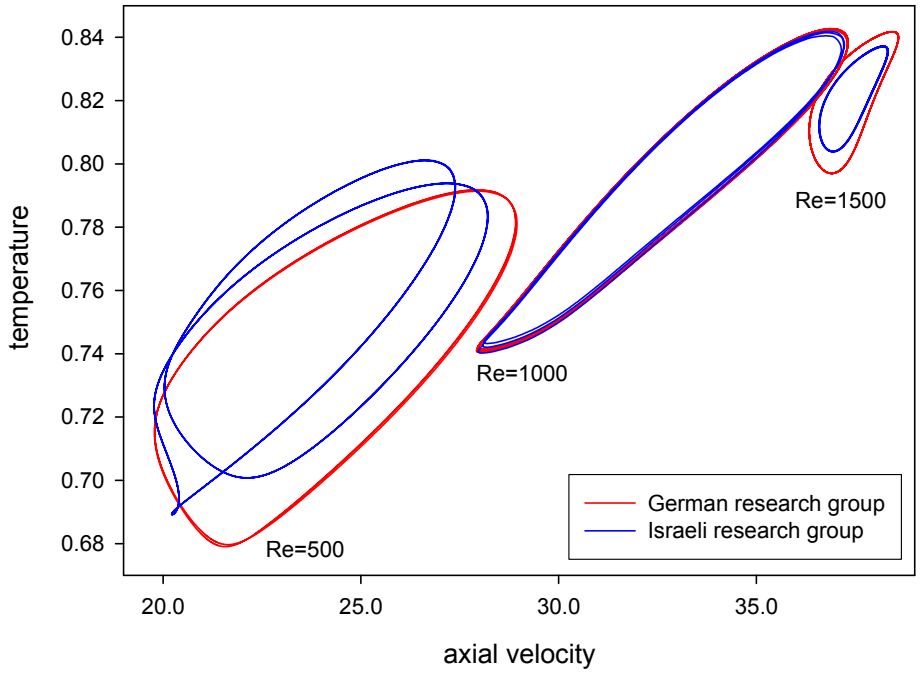

Figure 2.11: Phase plots for different rotational Reynolds numbers (Re) at a position close to the solid liquid interface ($r = 0.13$, $z = 0.8$) for $\Delta T = 0.27K$.

With the increase of ΔT or Re it is necessary to reduce the time step further. In the present work an automatic time stepping algorithm (Gear scheme [95]) has been applied instead of constant time steps. This algorithm starts with an initial time step which depends on how "good" the previous steady state solution was from which the transient calculations is supposed to be started. During the calculation this algorithm adapts the applied time step to the extrapolated development of the solution in time. If a calculation failes, the algorithm reduces the time step and repeats the calculation until the transient solution converges. Figures 2.8−2.10 show the results of time dependent simulations. Starting from oscillatory unstable state at the rotational Reynolds number $Re = 1500$, Re was reduced to the values 1000 and 500. For $Re = 1500$ and $\Delta T = 0.27K$ (fig. 2.8) the oscillations became sinusoidal after a certain period of time. With the decrease of Re to 1000 (fig. 2.9) sinusoidal oscillations could be still observed. In spite of the visible decrease in the total kinetic energy, the relative amplitude of oscillations has remained almost unchanged. Further decrease of Re to the value of 500 (fig. 2.10)

again has led to a decrease in the total kinetic energy.
In order to compare time dependent results phase plots were used. They show changes of the temperature and the axial velocity at a certain point over several oscillation periods (fig. 2.11). The phase plots of both research groups coincided for $Re = 1000$, and have agreed only qualitatively for $Re = 500$ and $Re = 1500$. It shows again that the grid dependence issue should be carefully checked when governing parameters are varied in large intervals. The Israeli research group have used FVM elements, which have only linear approximation and the German research group have used FEM elements with quadratic approximation. Another interesting observation was the oscillatory state at $Re = 500$, which stood in conflict with the predicted stability diagram in fig. 2.6 (red curve) [1]. But, it supports the updated results of fig. 2.7. However, as shown in [30], this happens because of the simultaneous existence of stable steady state along with the oscillatory one. Therefore it is important to search for the most dangerous eigenvalue during bifurcation studies.

2.2 Deeper analysis of the solution nature

After verifying the applied numerical tools, a deeper analysis of possible solutions had been done. When dealing with fluid dynamics in crystal growth, it is unavoidable to deal with very strong non-linear effects. The operating conditions in crystal growth of high melting temperature oxides (e.g. rare earth scandates) resulting in a melt flow caused by large driving forces (forced, natural and Marangoni convection) are mainly responsible for that high non-linearity. Different phenomena like spiral growth could be connected to melt flow instabilities. Therefore it is important to understand the nature of the solution structure of the melt flow. During the code verification process some results concerning the melt flow instability were carried out, already (see 2.1). Fig. 2.12 shows a diagram containing steady state solutions calculated in a direct numerical simulation (DNS). This solutions were supposed to be the last steady state solutions for a given parameter set (Re, ΔT), because there was no convergence when increasing the parameters. It had been found that the domain with the highest tendency to hydrodynamical instabilities for the $NaNO_3$ melt (see fig. 2.2) was located between rotational Reynolds numbers Re 500 and 1500. These values correspond to real crystal rotation rates of $5\,rpm$ and $15\,rpm$, respectively. From the experimental point of view this parameter interval is critical, especially during the seeding process. For $Re < 500$ thermal forces are dominant and for $Re > 1500$ rotational forces dominate the melt flow. In between both forces are in competition and made the solution structure more complex. Therefore

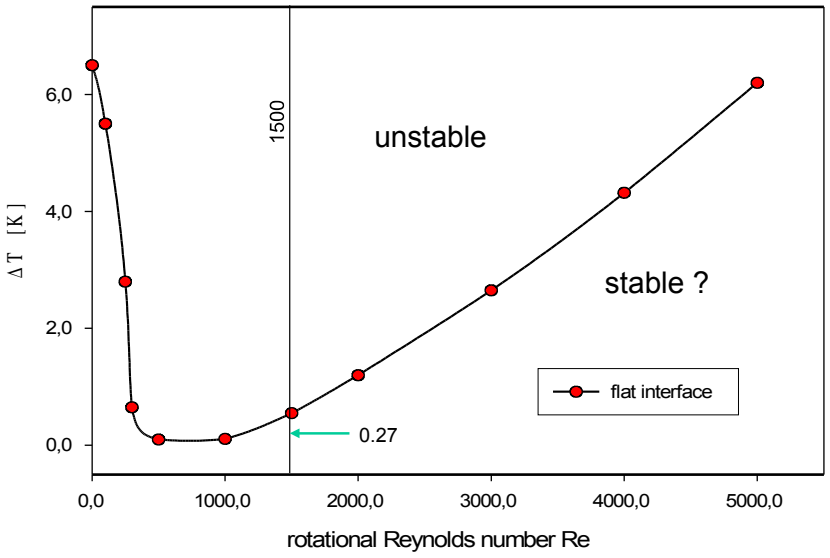

Figure 2.12: Direct numerical simulation of $NaNO_3$ melt flow in a CZ-crucible.

the tendency to melt flow instabilities was higher there. One would think that the curve in fig. 2.12 shows clearly the border between stable (below the curve) and unstable regions (above the curve). But, it had been found that below this curve the solution was not unambiguous. For parameters $Re = 1500$ and $\Delta T = 0.27$ a 2D oscillatory solution had been detected, also. Consequently, every steady state solution should be checked against its stability. Conventional DNS can miss such solutions and let one believe that the diagram in fig. 2.12 is globally valid. Branch following techniques can help to find such solutions much faster and more reliably [65]. Fig. 2.13 shows a Hopf bifurcation diagram for the control parameter Re. As solution the temperature difference along the melt free surface ΔT is plotted. The approach [65] used to calculate this bifurcation diagram has much better convergence properties than a Newtonian solver. For the latter usually $|R_h - R| \leq ch^2$ holds, where h is the size of the largest element in the applied mesh. In the applied Hopf bifurcation algorithm one expects the solution to converge with order of h^2, but at bifurcation points it shows a superconvergence [65] for the critical parameter with the order of $|R_h - R| \leq ch^4$. Superconvergence can occur at fold points and other symmetry breaking bifurcation points [65, 102, 103], also. Every Hopf bifurcation point on the green curve in fig. 2.13 can be the origin of periodic orbits. These are domains where oscilla-

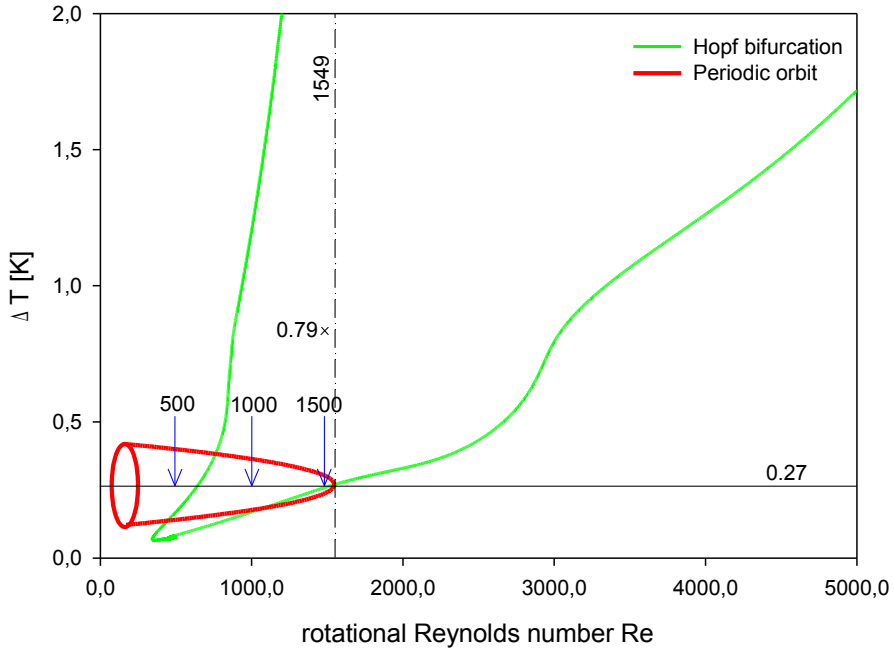

Figure 2.13: Bifurcation diagram after detecting Hopf points.

tory solutions can occur. For example, such a Hopf point had been found for parameters $Re = 1549$ and $\Delta T = 0.27$. The red paraboloid starting at $Re = 1549$ should indicate that there was the origin of a periodic orbit. This example of bifurcation was of subcritical type. The phase portrait in fig. 2.14 had confirmed that the oscillatory solution amplitude was decreasing if one is closer to the Hopf bifurcation point, where the periodic orbit may start. In the Hopf bifurcation diagram (fig. 2.13) several solutions had been analysed for $\Delta T = 0.27K$ and it had been found, that for decreasing Re the amplitude of the oscillation was increasing, which was confirmed by the shape of periodic orbits. This correlation is shown in fig. 2.11, where three phase maps were plotted for $Re = 500, 1000,$ 1500 and $\Delta T = 0.27K$. These results were obtained from transient calculations at a point close to the solid/liquid interface. For increasing Re the amplitude decreased. Diagrams in fig. 2.12 and 2.13 predict more unstable melt flow for high ΔT values. In fact, increasing the temperature difference ΔT for $Re = 1500$ the system is less stable. The phase diagram (fig. 2.15) for $Re = 1500$ and $\Delta T = 0.79K$ has shown that more than one frequency is present. Fig. 2.16 has confirmed this fact. The oscillations of the vertical velocity component were periodic, but exhibits more than one frequency. Fig. 2.17 shows results of the frequency

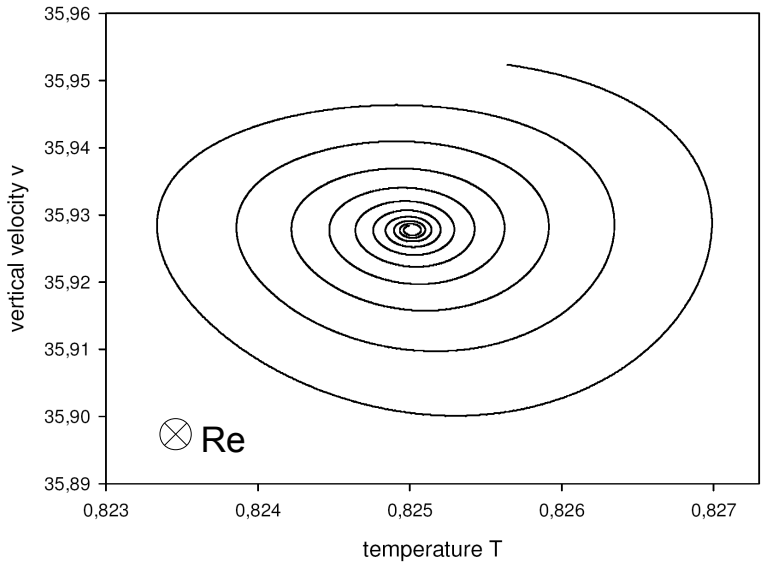

Figure 2.14: Phase portraits for $\Delta T = 0.27K$ at $v, T(0.13, 0.8)$ while varying Re.

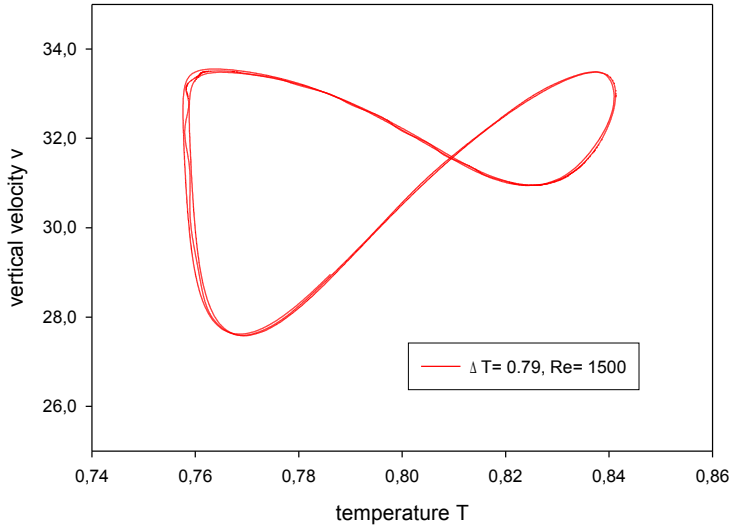

Figure 2.15: Phase diagram for a less stable melt flow.

analysis of transient simulation results for different ΔT and $Re = 1500$. For $\Delta T = 0.171K$ the oscillation was periodically stable. Increasing ΔT to $0.5K$ the oscillation was still periodically stable, but there was a first indication for an additional frequency. Further increase of ΔT has led finally to an unsta-

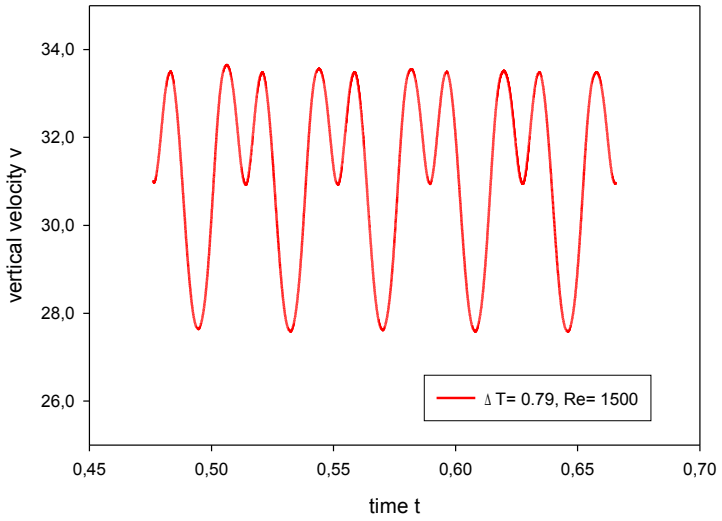

Figure 2.16: Oscillation diagram showing mixed frequencies of the vertical velocity.

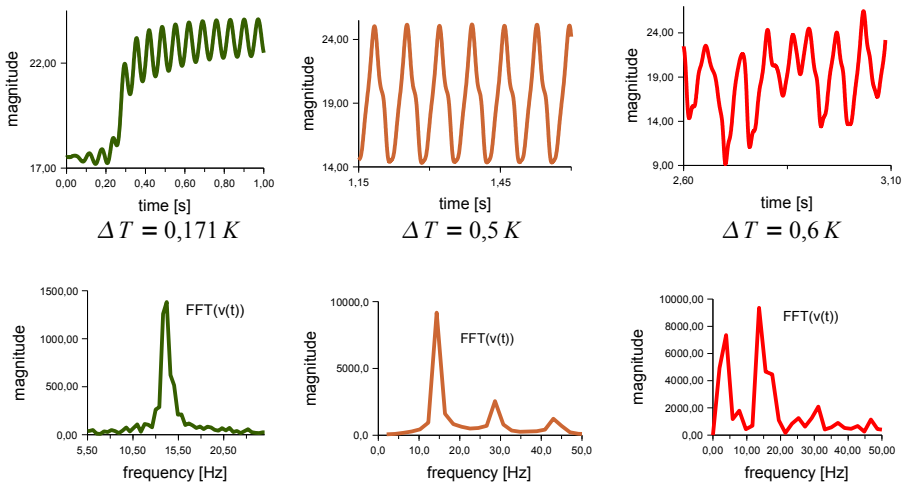

Figure 2.17: Transient simulation for different ΔT and frequency analysis.

ble state, whose oscillation was not periodic anymore. Therefore the onset of hydrodynamical instability for $Re = 1500$ must happen between $\Delta T = 0.5K$ and $0.6K$. Fig. 2.18 shows a path following diagram for $\Delta T = 1.0K$. The control parameter was Re and for the solution the total kinetic energy E_{kin} was plotted. Obviously, for negative Re the solutions were symmetric with respect to the zero axis. This shows that the governing equations were imple-

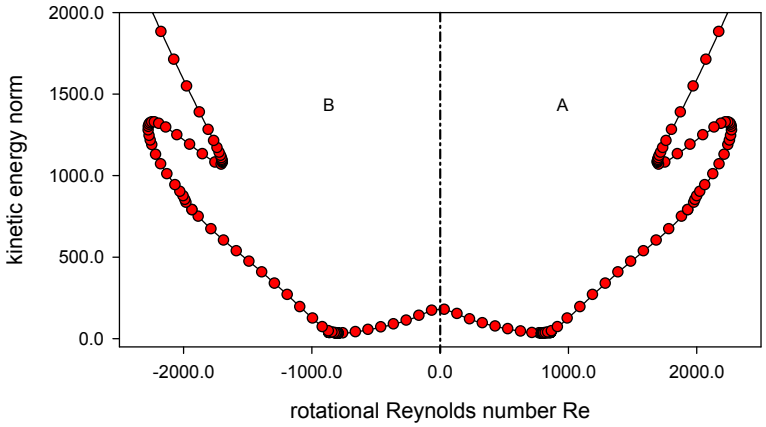

Figure 2.18: Continuation diagram for control parameter Re for $\Delta T = 1.0K$.

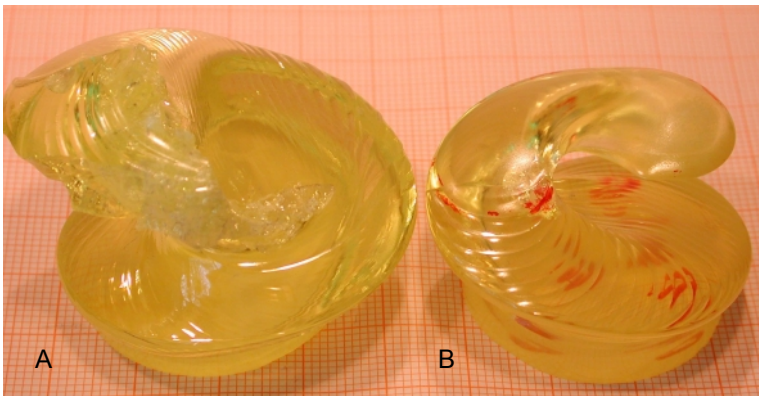

Figure 2.19: $DyScO_3$ crystals grown with opposite rotation directions. The formed spirals show opposite turns.

mented correctly, since the problem was axially symmetric. It corresponds to an opposite crystal rotation direction during the growth process. Experiments in which the crystal rotation direction has been changed confirm this behaviour. Fig. 2.19 shows two crystals grown with opposite crystal rotation direction. The crystal (fig. 2.19 (A)) has been rotated clockwise. The other crystal (fig. 2.19 (B)) has been rotated anti-clockwise. Obviously, the change of the crystal rotation direction has caused a change of the spiral turn.

Beside the solution symmetry in fig. 2.18 the curve shows a S-like shape between $Re \approx 1500$ and $Re \approx 2500$. This solution range shows limiting points, where the solution behaviour has changed. In fig. 2.20 and fig. 2.21 it is shown more detailed. The path following diagram in fig. 2.20 was calculated for $\Delta T = 0.27K$ and in fig. 2.21 for $\Delta T = 0.5K$. Between the LLP and RLP 3 solutions exist and outside this interval one solution, only. Exactly on

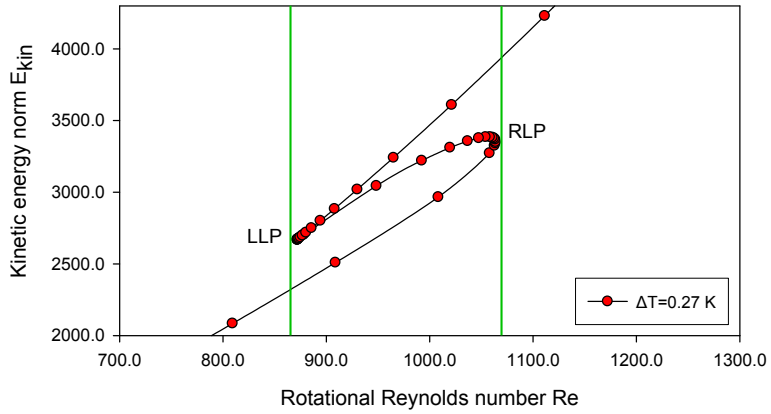

Figure 2.20: Multiplicity of solutions for $\Delta T = 0.27K$. (LLP: left limiting point, RLP: right limiting point)

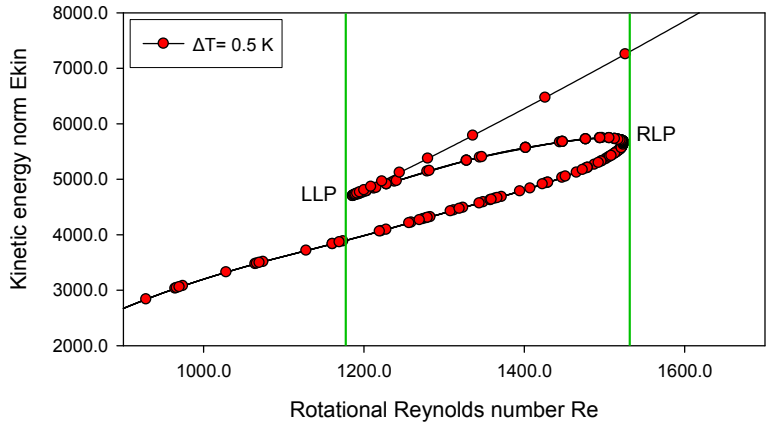

Figure 2.21: Multiplicity of solutions for $\Delta T = 0.5K$. (LLP: left limiting point, RLP: right limiting point)

both limiting points two solutions exist for the same value of Re. Comparing the path following diagrams for $\Delta T = 0.27K$ (fig. 2.20) with diagrams for $\Delta T = 0.5K$ (fig. 2.21) and $\Delta T = 1.0K$ (fig. 2.18) it can be seen that the S-like solution branch was shifted to the right, i.e. to higher Re. Because of the solution multiplicity, this region is interesting, since there melt flow instability can occur. So, for increasing ΔT unstable solution branches are shifted to regions of higher Re. A further result is, that the interval with multiple solutions had expanded for higher ΔT. For $\Delta T = 0.27K$ the region between LLP and RLP was about $Re = [870, 1070]$, for $\Delta T = 0.5K$ it was about $Re = [1200, 1500]$, and for $\Delta T = 1.0K$ it was about $Re = [1700, 2300]$, i.e. the unstable interval becomes wider.

2.3 Summary and concluding remarks

Before analysing a real Czochralski crystal growth process in chapter 4 the numerical tools were verified using a simplified crystal growth model in this chapter. It has only been considered the rectangular melt domain as the axisymmetric case. The material properties of a well-known material ($NaNO_3$) has been taken from literature [35]. The melt flow was simulated using a hydrodynamic model. It considers a flow, driven by buoyancy convection, thermocapillary convection and crystal rotation, governed by the Navier-Stokes equations in the Boussinesq approximation, the continuity equation and the temperature equation, respectively. Steady state simulations have been performed for different rotational Reynolds numbers and $\Delta T = 1.0K$. They have been compared quantitatively with results carried out in [1]. A first indication for an unstable flow could be observed and it has been carried out a stability diagram by direct numerical simulation. However, this is not reliable, because it is strongly grid dependent especially for low rotational Reynolds numbers and it can miss important solutions. Therefore, more complex continuation and bifurcation techniques have been applied for a deeper analysis of the melt flow solution structure. It could be shown that multiple solutions can occur for the same control parameter. Thereby, unstable solutions and stable steady states are possible. However, also stable oscillatory solutions are possible, which could be missed by the direct numerical simulation. Hopf-Bifurcation results have been carried out, which show possible origins of periodic orbits. Also, transient simulation results have shown that oscillatory solutions exists, but also solutions with mixed frequencies, which are more complex.

Chapter 3

Gaining important physical properties of the $DyScO_3$ melt

Rare earth scandate crystals $ReScO_3$ (Re=La, Ce, Pr, Nd, Sm, Eu, Gd, Tb and Dy) can be grown from the melt at temperatures of about 2100 °C. The needs of thermal insulation of the whole system are very high in order to reach the melting point and to control the thermal gradients, which are required by the Czochralski (Cz) method. The consequence is that in-situ system observations are practically almost impossible or very hard to perform (see fig. 3.1). Therefore numerical investigations using a mathematical model of the real system can be very helpful. However, numerical models need some physical properties of the considered real system (e.g. density, viscosity, thermal expansion coefficients, thermal conductivity). Most material properties of high melting oxides are not referenced in the literature or they are incomplete and inaccurate. Because the accuracy of qualitative and quantitative results of numerical simulations depend on the used physical properties, corresponding measurements were performed in an adapted Cz configuration at a temperature around the melting point of $DyScO_3$ (2060 °C).

3.1 Measurement setup

For the measurements the IKZ Cz-equipment (Cyberstar - OXYPULLER 20-03, [104]) was used. Fig. 3.1 shows a sketch of the principle measurement setup. The system was heated inductively at f=10 kHz with a RF generator (Hüttinger - STG 50/10 [105]). Due to the high melting temperature an iridium crucible was used. However, it was operated at the upper thermal limits of this material. It was important to control the temperature distribution in the crucible in order to melt the material homogeneously, without local

overheating of the crucible. Therefore the whole system was insulated within an enclosure.

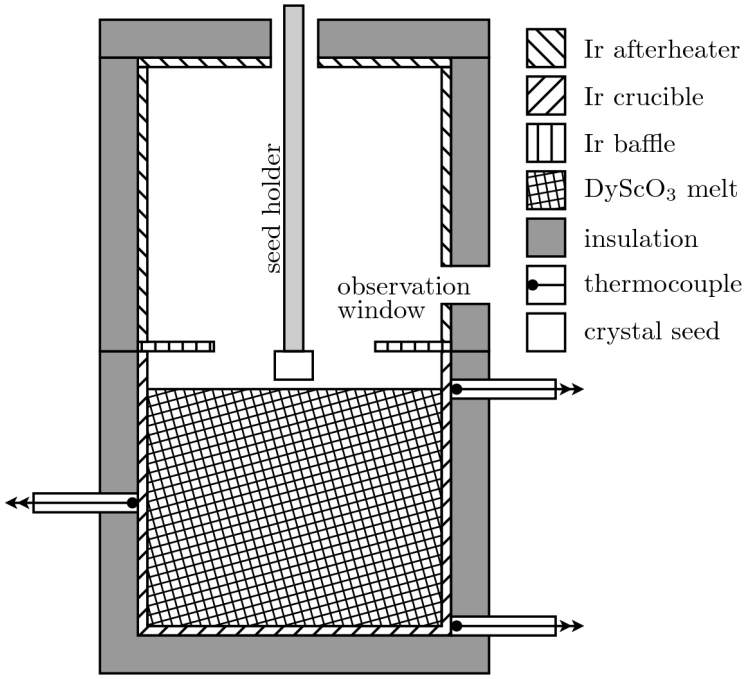

Figure 3.1: Sketch of the typical Czochralski (Cz) crystal growth arrangement, which was adopted for the measurements of physical properties of the $DyScO_3$ melt. (Ir: iridium, $DyScO_3$: dysprosium scandate)

Fig. 3.1 also shows an iridium baffle and active afterheater, which were used to control the temperature gradients during the crystal growth process. The crystal seed was fixed by the crystal seed holder. Depending on the type of measurement the crystal seed was replaced (see fig. 3.1) by tools needed for the measurement. The principle setup arrangement was the same and was located in a water cooled steel chamber, which was evacuated and filled with a quasi inert gas (e.g. N_2 or Ar). The chamber allows for leading through 6 wires used to connect the thermocouples inside to the digital recorder outside with built-in measurement unit for voltage (LOGOSCREEN™ cf / 6 Channels [106]). During the measurements the melt surface was observed with a camera system through a 8x12 mm window in the insulation and afterheater, respectively.

3.2 Temperature measurement outside and inside the iridium crucible

The setup arrangement of fig. 3.1 was used for measuring the temperature distribution outside the iridium crucible at 3 equidistant positions. The measurement was performed during the whole Cz crystal growth process (growth rate was about 1 mm/h) using Ir / Ir40%Rh thermocouples (see fig. 3.2).

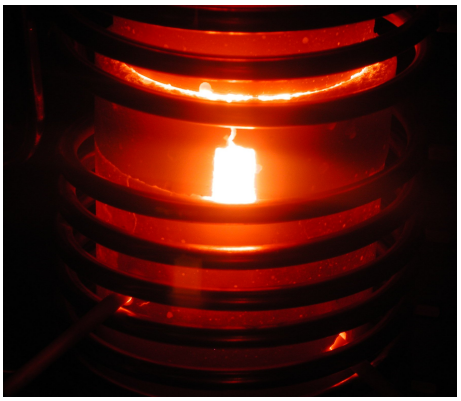

Figure 3.2: Temperature measurement during a Czochralski (Cz) crystal growth process, the dysprosium scandate ($DyScO_3$) melt is visible through the observation window.

This thermocouples have smaller thermovoltage (10.74 mV at 2000 °C) than W5%Re / W26%Re thermocouples (33.67 mV at 2000 °C) [107], but the latter were not chemically stable in the environment applied. Although, the chamber was evacuated and filled with N_2 or Ar, respectively, these thermocouples have oxidized during the measurement. Apparently, there was still a small O_2 portion in the atmosphere. Probably, the porous insulation ceramic has freed small portions of O_2 and the evaporating gas from the melt contained oxygen, too. Beside the smaller thermovoltage, another disadvantage of Ir-based thermocouples was its mechanical instability, especially after the heating up and cooling down process they become very brittle. In this case minimal vibrations can lead to cracking the thermocouples making the experimental handling difficult. The temperature outside the crucible at the bottom was about 90 K smaller than the melt temperature (see fig. 3.5). The main problem during temperature measurement was the bad thermomechanical connection between the thermocouples and crucible wall.
The results of the temperature measurement at the outer crucible wall during a Cz growth of DyScO3 are shown in fig. 3.3. As expected, the temperature

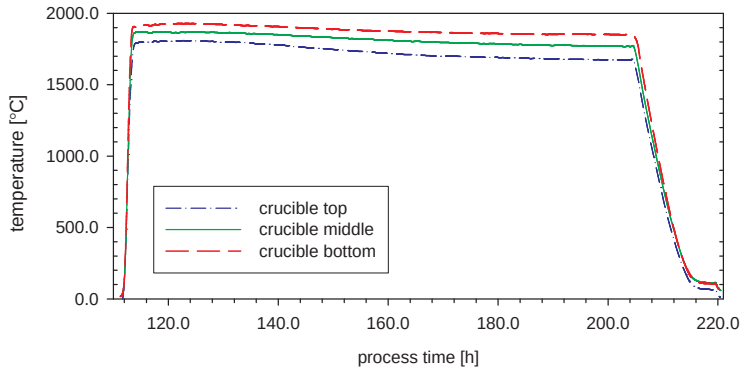

Figure 3.3: Temperature measurement at the outer crucible wall during Cz growth of $DyScO_3$.

is lowest at the top of the crucible and highest at about 10 mm above its bottom, which is in agreement with the calculations presented in [108]. It was impossible to measure internal melt temperature changes from outside the crucible, because the crucibles thermal conductivity smoothes the relatively small thermal changes in the melt. The axial temperature gradient at the outer crucible wall was about 25 K/cm.
Furthermore, the result in fig. 3.3 can be split into 3 parts. These are heating up and melting process of the oxide substances, the growth process and the cooling down process. The automatic growth control has reduced the generator power during the growth process, because the melt level was dropping (less melt had to be heated) and the grown crystal has closed the baffle hole (less heat loss at the free melt surface).

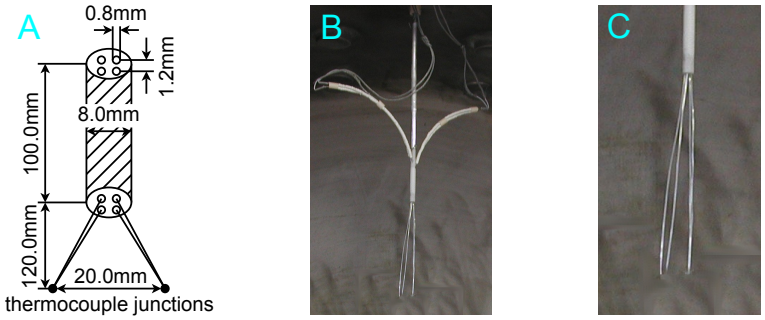

Figure 3.4: Sketch of the 4-hole alumina pipe carrying the 4 thermocouple wires for 2 thermocouples (A). Installed and connected thermocouples (B) with detailed view (C).

After measuring the temperature outside the crucible the vertical temperature distribution was measured inside the $DyScO_3$ melt. Two self made Ir / Ir40%Rh thermocouples (see fig. 3.4) were deployed and moved down to the melt surface. After touching the melt surface, it was further immersed into the melt. The main problem here was the insulating holder for the thermocouples, which should be stable at high temperatures (around 2000 °C). Due to thermal expansion of the thermocouple wires it could short-circuit and it could not be guaranteed that the thermocouples were immersed absolutely vertical. Fig. 3.5 shows the measured temperature distribution at the outer crucible wall at three different fixed locations (three black curves) and the temperature distribution during the vertical translation process of the two inner thermocouples (blue and magenta curve). In fig. 3.5 sections A and B corresponded to the heating up process, but in A a steeper ramp was applied. In sections A and B all thermocouples are fixed. In C could be observed that $DyScO_3$ was molten completely, thus the generator power was fixed and the two inner thermocouples (blue and magenta curve) were moved down (starting from afterheater top position). The inner thermocouple translation process was continued in sections D and E. The three outside thermocouples (black curves) are fixed in sections D-E, also. In section D

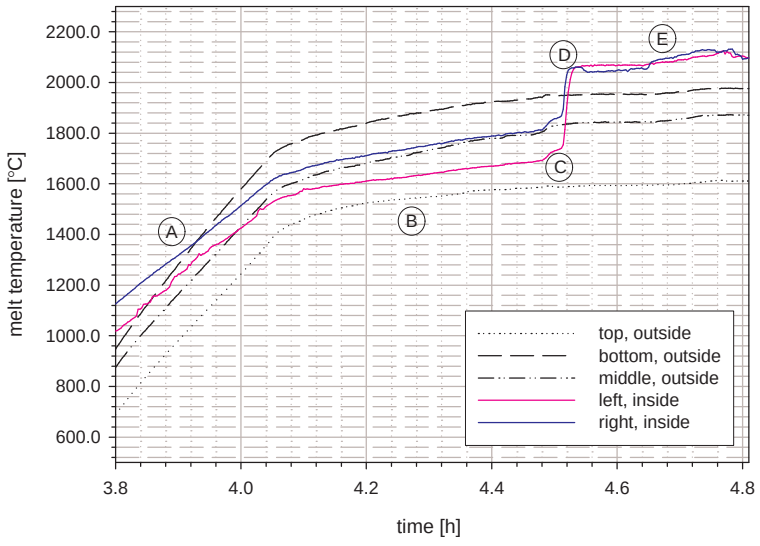

Figure 3.5: Temporal temperature distribution at three fixed locations at outer crucible wall and at two variable locations inside the afterheater and melt, respectively. (A, B: heating up process, C: melting point exceeded / start of the thermocouple translation, D: thermocouples touched the melt surface, E: thermocouples about 10 mm above the crucible bottom

the thermocouples touched the melt surface. Because the melt is coldest at the free surface, the temperature measured there was assigned to the melting point of $DyScO_3$, which is about 2060 °C. In [109] the proposed phase diagram for the system $Sc_2O_3 - Dy_2O_3$ predicts a melting point of about 2100 °C. The thermocouples were immersed into the melt to a position about 10 mm above the crucible bottom (fig. 3.5, E). The difference between the values measured by the two inner thermocouples was a consequence of slightly different height of the thermocouples and thermocouple junction surfaces. A possible non-symmetric immersion of the thermocouple (due to thermal expansion of Ir wires) could be another reason.

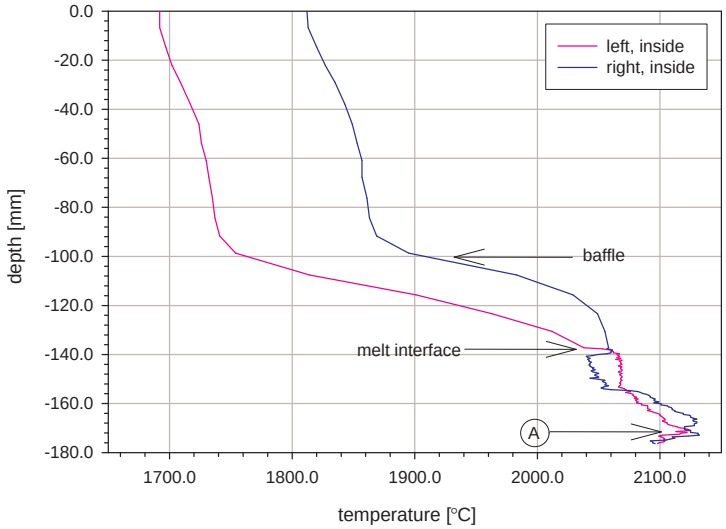

Figure 3.6: Vertical temperature profile starting from top of the afterheater (depth=0.0 mm) and ending at (A) in the melt about 10 mm above the iridium crucible bottom (generator power was fixed).

Fig. 3.6 shows the vertical temperature profile in the melt. The temperature distribution in the afterheater inner space was approximately linear. Around the thermocouple depth of about 100 mm the baffle was reached and the vertical temperature gradient became steeper. After immersion into the melt the temperature has increased up to a maximum value (at about 15 mm above the crucible bottom) and has decreased then, because of the heat loss of the crucible bottom. This results are in agreement with the calculations done in literature [108]. The temperature profiles were strongly coupled to the coil geometry. A small change of the coil geometry (e.g. coil height related to the crucible) changed the electromagnetical coupling and generated a different

modulation of the generator for different coil geometries. Therefore it was impossible to work with absolute temperatures. This is also the reason why the "liquid" state of the melt must be identified through the observation window for each new crystal growth process.

3.3 Electrical conductivity

The same setup as in section 3.2 for vertical temperature distribution inside the $DyScO_3$ melt was used to measure the electrical conductivity of the $DyScO_3$ melt. The thermocouple wires were connected with a voltage and current controlled source assuming a constant DC electrical current I and measuring the voltage drop V across the "internal resistor" R_i at the melt surface (see fig 3.7). Usually the 4-electrode method [110] is much more reliable than the used two point method. This could not be applied, because of the restrictions of the measurement setup and the very high operating temperatures (about 2100 °C). The electrical conductivity of the $DyScO_3$ melt

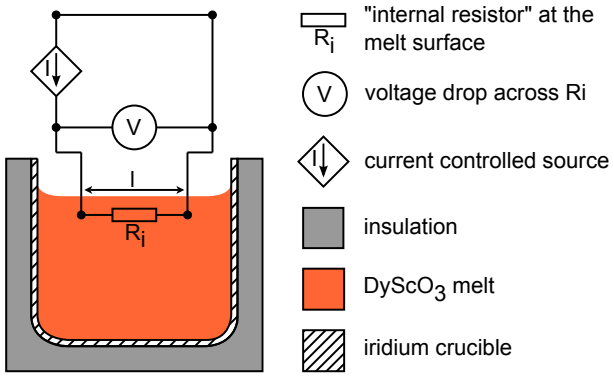

Figure 3.7: Setup for measuring the electrical conductivity of the $DyScO_3$ melt.

was measured close to the melting point at the melt surface (tab. 3.1). While neglecting side effects (e.g. parasitic resistivities, thermo-electric voltage) the electrical conductivity $\kappa = \rho^{-1}$, considering the specific resistance $\rho = R \cdot l$ of the one dimensional melt of length l between the two thermocouples, of the $DyScO_3$ melt was of order $10^{-7}\Omega^{-1}cm^{-1}$. Thereby, a combination of electronic and ionic charge transport was assumed, which has to be analysed in future. The averaged electrical conductivity was $2.1 \cdot 10^{-7}\Omega^{-1}cm^{-1}$, with an error of about 5 %.

Current [μA]	Voltage [V]	Resistance [MΩ]
1.15	2.63	2.29
1.23	2.92	2.37
1.52	4.08	2.68
2.04	5.04	2.47
2.52	5.68	2.25
5.03	12.36	2.46

Table 3.1: Measured electrical resistivity of the $DyScO_3$ melt at the melt surface.

3.4 Surface tension

For measuring the surface tension of the $DyScO_3$ melt the Wilhelmy plate method [73] was applied. The wetting property of the melt was used for measuring a weight force during pulling a small plate out of the melt. A small iridium plate with defined dimensions (20x10x1 mm) was deployed and connected to the crystal seed holder. Then the plate was immersed into the melt slowly (1mm/min.). After the plate was completely immersed into the melt, the plate temperature had to be adjusted to the melt temperature. Then, the plate was pulled slowly out of the melt and the weight force was measured, which is maximum when the melt disconnects from the plate (fig. 3.8). Fig. 3.8 also shows a photo of the Wilhelmy plate above the solidified

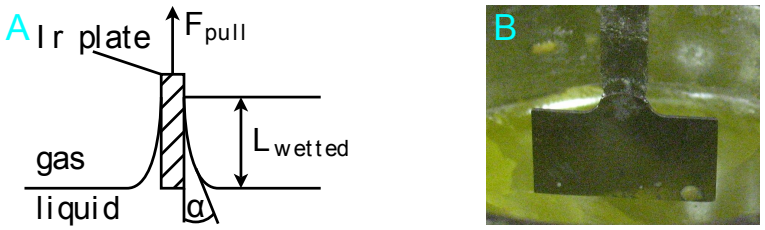

Figure 3.8: Principles of the Wilhelmy plate method (A). Installed Wilhelmy plate above the "frozen" melt (B).

melt. The surface tension of the melt was calculated as, $\sigma = F_g \cdot (L_w \cdot cos\alpha)^{-1} = m \cdot g \cdot (L_w \cdot cos\alpha)^{-1}$, where m is the mass of the melt attached to the plate, g is the gravitational acceleration, L_w is the length of the wetted plate area and α is the contact angle. The iridium plate was wetted completely and the contact angle α was about zero, thus the $cos(\alpha)$ term could be neglected. $L_w = 21.0\,mm$ resulted from twice L_{wetted} plus the thickness of the iridium plate, which was about $1.0\,mm$. The surface tension was measured for three different temperatures and the values for several measurements could be reproduced at constant temperature. The results are shown in tab. 3.2.

m [g]	**Δm [g]**	**P_{RF} [%]**	**T_{out} [°C]**	**T_{melt} [°C]**	**σ [N/m]**
3.043	0.015	40.8	1980.0	2070.0	1.421
3.034	0.015	41.0	1990.0	2080.0	1.417
3.025	0.01	41.2	2003.0	2093.0	1.413

Table 3.2: Measured values using the Wilhelmy plate method. m: mass, Δm: standard deviation of m, P_{RF}: generator power, T_{out}: temperature at the outer crucible wall, σ: calculated surface tension of $DyScO_3$.

The temperature in the melt was not measured during the surface tension experiment, because of the restrictions in the measurement setup (see fig. 3.1), but only the temperature at the outer iridium crucible wall. In section 3.2 the temperature in the melt was measured, which was about 90 K larger than outside the crucible. Because the geometry has not been changed, i.e. the relative height of the crucible to the RF coils, the generator power P_{RF} represents the same heat generation in the crucible and so the same temperature in the melt. The relative change of the temperature with the RF power has been reproduced around the melting temperature of $DyScO_3$, which was about 2060 °C. The temperature dependence of the surface tension was about $-3.48 \cdot 10^{-4} N/m \cdot K$ in the measured temperature range. The

IKZ-measurements					
Property	**Units**	**$DyScO_3$**	**GGG**	**Nd:YAG**	**$LiNbO_3$**
σ	N/m	1.421	1.285	0.709	0.317
T_σ	°C	2070	1753	1975	1283
$d\sigma/dT$	$N/m \cdot K$	$-3.48 \cdot 10^{-4}$	$-2.76 \cdot 10^{-4}$	$-7.5 \cdot 10^{-5}$	$-8.05 \cdot 10^{-5}$
T_{range}	°C	2070-2093	1753-1840	1975-2035	1283-1519
Data taken from literature					
Property	**Units**	**Al_2O_3**[111]	**GGG**[16]	**YAG**[112]	**$LiNbO_3$**[113]
σ	N/m	0.7	0.7	0.781	0.297
T_σ	°C	2043	1750	1970	1300
$d\sigma/dT$	$N/m \cdot K$	$-6 \cdot 10^{-5}$	–	$-3.5 \cdot 10^{-5}$	$-7.85 \cdot 10^{-5}$
T_{range}	°C	–	–	1970-2070	1275-1345

Table 3.3: Comparison of measured surface tension σ and its temperature dependence $d\sigma/dT$ with corresponding values of other oxide melts taken from the literature. The error bound for the IKZ measurements was about 1 %. ($DyScO_3$: dysprosium scandate, GGG: gadolinium gallium garnet, $Nd:YAG$: neodymium doped yttrium aluminium garnet, $LiNbO_3$: lithium niobate, Al_2O_3: sapphire, YAG yttrium aluminium garnet)

surface tension of $DyScO_3$ at 2070 °C was $1.421 N/m$, about 2 times larger than the surface tension of sapphire, which is known to be $0.7 N/m$ [111]. The temperature dependence of the surface tension of $DyScO_3$ melt was one order of magnitude larger than corresponding values of other high melting oxide substances, which are known from literature (see tab. 3.3). Thus the measurements had to be verified by measuring the surface tension of another high melting oxide, i.e. gadolinium gallium garnet (GGG) (see tab. 3.4). Although GGG had an about 300 K lower melting point, the observations

m [g]	**Δm [g]**	**P_{RF} [%]**	**T_{out} [°C]**	**T_{melt} [°C]**	**σ [N/m]**
2.75	0.015	56.9	1663.0	1753.0	1.285
2.72	0.01	57.9	1706.0	1796.0	1.271
2.70	0.015	58.9	1750.0	1840.0	1.261

Table 3.4: Measured values using the Wilhelmy plate method. m: mass, Δm: standard deviation of m, P_{RF}: generator power, T_{out}: temperature at the outer crucible wall, σ: calculated surface tension of GGG.

have shown that it has a very similar flow pattern on the melt surface (see fig. 3.9) caused by the Marangoni convection. Obviously, it has a very

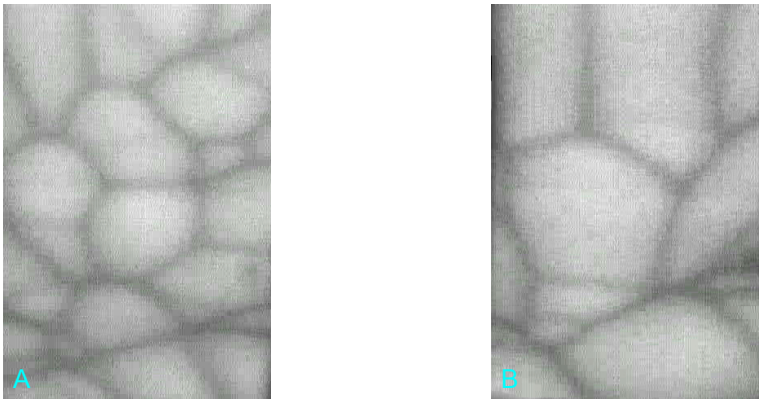

Figure 3.9: Photos of a typical surface tension driven flow pattern at the melt surface of dysprosium scandate $DyScO_3$ (A) and gadolinium gallium garnet GGG (B) close to the melting point. The scaling of the photos is the same.

similar sensitivity of the surface tension with respect to temperature changes compared to the $DyScO_3$ melt. Therefore the surface tension dependence of GGG and $DyScO_3$ melt on temperature should be of the same order of magnitude. Tab. 3.3 allows for a comparison of the surface tension and its temperature dependence of some other oxide melts referenced in the literature

[16, 111–113]. The measured surface tension of lithium niobate ($LiNbO_3$) melt was similar to that in the literature and also its temperature dependence was close to the referenced in [113]. It must be noted that the yttrium aluminium garnet (YAG) melt in IKZ measurements was neodymium (Nd) doped. However, the surface tension value was close to the value of undoped YAG melt referenced in [112]. Also, the thermocapillary coefficient of $Nd:YAG$ was of the same order as published in [112]. The surface tension of the gadolinium gallium garnet (GGG) melt was about 70% larger than the published value in [16]. However, it must be noted, that the GGG melt surface tension in [16] is estimated from Al_2O_3 melt. Unfortunately, no value for comparison could be found for the thermocapillary coefficient. Also, no comparison value from the literature could be found for the $DyScO_3$ melt. Because of similar melting point the measured surface tension of the $DyScO_3$ melt has been compared with surface tension properties of a sapphire melt referenced in [111].

3.5 Viscosity

Viscometry offers many methods for measuring the viscosity of fluids, e.g. glass capillary, U-tube, rotational, vibrational/oscillating or bubble viscometer [73, 114, 115]. However, at very high temperatures ($\approx 2000\,°C$) the range of applicable materials is very restricted. Therefore the dynamic viscosity of the $DyScO_3$ melt was measured using an industrial rotary viscosimeter (Rheotest® RN 3.1 [116]) equipped with a special adapter for the IKZ Cz crystal puller. The basic method of measuring the dynamic viscosity using a rotary viscosimeter is to rotate a body with well defined geometry (e.g. coned cylinder [116]) in a fluid. The rotation rate and the torque were measured. This allows for a calculation of the dynamic viscosity by detecting the shear stress and the shear gradients [115]. Standardized rotary bodies do not exist for very high temperatures (around 2000 °C). Therefore a body made from iridium was used, i.e. an used iridium crucible with a diameter of 40 mm, a height of 36 mm and a wall thickness of 1.5 mm. At the bottom of this crucible a long iridium rod was welded. This rotary body was connected via the seed rod to the viscosimeter. The main problem here was the centring and vertical alignment of the rotary body. Fig. 3.10 shows a sketch (A) and a photo (B) of the self made rotary body and the corresponding setup arrangement (C). Two holes of 1 mm diameter in the rotary body are for letting out the gas during immersion into the melt. Another problem was the relatively large mass of the rotary body, which had to be warmed up to the same temperature as the melt, otherwise the melt would be "freezing"

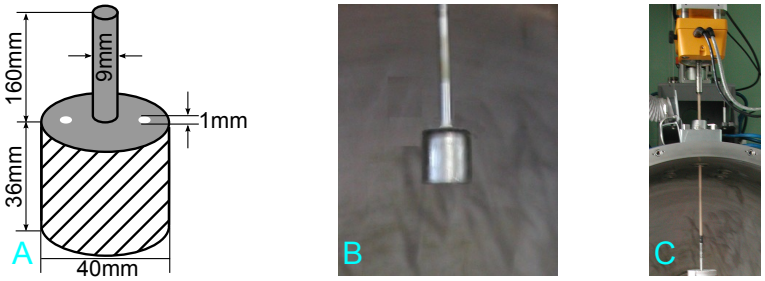

Figure 3.10: Sketch (A) and photo (B) of the self made iridium rotary body. Setup arrangement with installed viscosimeter (C).

during immersion into the melt. However, the aim was to measure the dynamic viscosity as close as possible to the melting point of $DyScO_3$. At the same time the measurement was operating at the upper thermal limits of the iridium parts in the setup. Especially the mechanical stability of the crucible containing the melt was critical because it became more and more "soften" and porous with increasing temperature > 2000 °C and could leak or crack at all. This was dangerous, especially when rotating the body within the melt. Because a rotary body with a well defined geometry was not available, it was impossible to calculate the dynamic viscosity directly. But the relation of the measured torque to the rotation rate is proportional to a constant value SC (system constant), which represents the relationship of the shear stress and velocity gradient. Therefore the SC had to be determined for applied geometry using a fluid with known density and dynamic viscosity, which was in the range expected for the crystal melt. This calibration was the first step adapting the setup to the applied geometry (rotary body, crucible containing the fluid). The iridium crucible should not be contaminated with the

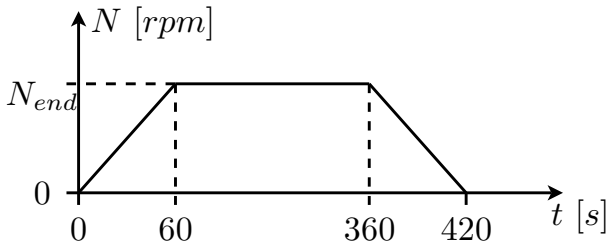

Figure 3.11: Temporal signal ramp of the applied rotation rate of the rotary body with end rotation rate $N_{end} = 10, 30\ rpm$.

calibration fluid (special mineral oil [116]), therefore the same crucible made from aluminium was used. The SC was determined for two selected rotation rates of the rotary body ($N_{end} = 10, 30\ rpm$) applying a temporal signal

ramp shown in fig. 3.11. After the calibration process the dynamic viscosity of the $DyScO_3$ melt was measured. The values for torque M and rotation rate N were measured every 0.2 seconds during a period of time as shown in fig. 3.11. Tab. 3.5 contains the averaged values of the measurements in the time interval [80s; 350s]. The temperature was measured simultaneously

ID [m]	SC [1/m^3]	M [mNm]	N_{end} [1/min]	η [mPas]	error [%]
$1/3 \cdot h_{rb}$	35286.8176	0.0146	10.0082	51.4765	2.5
$1/3 \cdot h_{rb}$	35286.8176	0.0211	10.0078	74.3972	2.4
$1/3 \cdot h_{rb}$	35286.8176	0.0157	10.0030	55.3837	2.6
$1/3 \cdot h_{rb}$	**35286.82**	**0.017**	**10.006**	**59.952**	**2.5**
$1/2 \cdot h_{rb}$	30282.5605	0.0190	9.9992	57.5415	2.8
$1/2 \cdot h_{rb}$	30282.5605	0.0194	9.9923	58.7934	2.4
$1/2 \cdot h_{rb}$	30282.5605	0.0194	10.0075	58.7041	2.6
$1/2 \cdot h_{rb}$	**30282.56**	**0.019**	**9.999**	**57.543**	**2.6**
$2/3 \cdot h_{rb}$	25301.7035	0.0203	10.0082	51.3204	2.4
$2/3 \cdot h_{rb}$	25301.7035	0.0203	10.0082	51.3204	2.6
$2/3 \cdot h_{rb}$	25301.7035	0.0204	1.0119	51.5541	2.5
$2/3 \cdot h_{rb}$	**25301.70**	**0.020**	**10.009**	**50.558**	**2.5**
$1/3 \cdot h_{rb}$	45966.7797	0.0326	29.9953	49.9584	1.7
$1/3 \cdot h_{rb}$	45966.7797	0.0344	29.9967	52.7144	1.3
$1/3 \cdot h_{rb}$	45966.7797	0.0347	30.0029	53.1631	1.5
$1/3 \cdot h_{rb}$	**45966.78**	**0.034**	**29.998**	**52.099**	**1.5**
$1/2 \cdot h_{rb}$	37847.5888	0.0385	30.0043	48.5641	1.6
$1/2 \cdot h_{rb}$	37847.5888	0.0376	30.0135	47.4143	1.4
$1/2 \cdot h_{rb}$	37847.5888	0.0401	30.0004	50.5889	1.5
$1/2 \cdot h_{rb}$	**37847.59**	**0.039**	**30.006**	**49.192**	**1.5**
$2/3 \cdot h_{rb}$	30124.4307	0.0487	29.9912	48.9163	1.5
$2/3 \cdot h_{rb}$	30124.4307	0.0472	29.9378	47.4942	1.6
$2/3 \cdot h_{rb}$	30124.4307	0.0472	29.8794	47.5871	1.1
$2/3 \cdot h_{rb}$	**30124.43**	**0.048**	**29.936**	**48.302**	**1.4**

Table 3.5: Measured and averaged torque M and rotation rate N_{end} of the rotary body for immersion depths ID=1/3, 1/2 and 2/3, related to the height of the rotary body $h_{rb} = 36mm$ (η: dynamic viscosity).

outside the crucible close to the crucible wall. The system was heated up in approx. 5 h to a temperature close to the melting temperature. The used generator was power controlled and could be modulated from 0 to 100% in 0.1% steps. The generated heat in the iridium parts of the system depends strongly on the used setup (e.g. number of RF coil windings, position of

the RF coil), therefore it is impossible to heat up the system to a certain temperature setpoint. Thus the generator power P_{RF} had to be fine tuned by observing the $DyScO_3$ surface through a small window. The observation window is a heat sink and cools the surface. Therefore the coldest location in the melt is the surface close to the observation window. This way it could be assured that the substance was completely molten when the last solid "island" on the surface disappeared. At this point the melt temperature was a few K above the melting point, and the rotary body was moved down slowly (about 1 mm/min.) and was stopped close above the melt surface letting it adapt to a temperature close to the melting temperature of $DyScO_3$. Then one third (immersion depth $ID = 1/3 \cdot h_{rb}$) of the rotary body was dipped slowly (1mm/min.) into the melt. The rotary body had a relatively large heat capacity and it transferred heat away, so the melt was "freezing". Again, the generator power P_{RF} had to be increased. The body was rotated with $N_{end} = 10, 30\ rpm$ (see fig. 3.10, left) and the torque was measured. This process was repeated for immersion depth $ID = 1/2 \cdot h_{rb}$ and $ID = 2/3 \cdot h_{rb}$. The rotary body has conducted more heat for larger ID, because the interaction surface was larger. Therefore with increasing ID also P_{RF} had to be increased to prevent the melt from solidifying. The complete immersion of the used rotary body was impossible, because the melt was "freezing" in spite of increasing P_{RF}. For each end rotation rate N_{end} and for each ID the torque M and rotation rate N_{end} were measured three times. The dynamic viscosity η was calculated as $\eta = M \cdot N^{-1} \cdot SC$, where M is the measured torque, $N = N_{end}$ is the measured rotation rate and SC is the calculated system constant from calibration with an oil with known η ($\eta_{oil} = 77.61\, mPa \cdot s = 77.61\, g/m \cdot s$). In tab. 3.5 the measured

IKZ-measurements					
Property	**Units**	**$DyScO_3$**	**GGG**	**Nd:YAG**	**$LiNbO_3$**
η	mPas	49.86	–	62.0	42.5
Data taken from literature					
Property	**Units**	**Al_2O_3**[16]	**GGG[16]**	**YAG**[55, 112]	**$LiNbO_3$**[113]
η	mPas	2.72	40.0	46.0	38.0

Table 3.6: Comparison of the dynamic viscosities η measured at IKZ with values taken from literature.

values were averaged. The values were much more reliable (the variation was smaller) for larger ID. This is reasonable, because the interaction area became larger. Also, they were more reliable for higher N, because the used viscosimeter was more accurate at higher N. The calculated η became smaller

with larger ID, because P_{RF} had to be increased to prevent the melt from freezing and thus the melt temperature has increased as indicated by the thermocouples outside the crucible. Additionally, η was influenced by the melt meniscus ($3-4\,mm$ high), which has increased the effective immersion depth of the rotary body. However, this influence was smaller for larger ID and could be neglected, because it was compensated by the system constant SC, which was determined in a system with similar meniscus height. The measurement of η was performed about $10-30\,K$ above the melting point of $DyScO_3$. Because of the large variation of values for $N_{end}=10\,rpm$, for the calculation of an averaged $\eta=\overline{\eta}$ only the mean values of tab. 3.5 (bold values) for $N_{end}=30\,rpm$ were taken into account. This was compared in tab. 3.6 to dynamic viscosities of other oxide melts taken from the literature [16, 55, 112, 113].

3.6 Density

The melt density is very important for the real crystal growth (automatic crystal growth control), but also for numerical simulations of the melt flow. Therefore the $DyScO_3$ melt density was determined.
The density $\rho_s \approx 6.79 g/cm^3$ of the solid phase was calculated from the measured weight of a defined volume. This result had been confirmed by other measurements ($\rho_s \approx 6.922 g/cm^3$) [117] using a more accurate method. Due to the very high temperature, especially the melt density measurement is not trivial. No special density measuring equipment (e.g. pycnometer or oscillating U-tube [73, 118]) was available. Therefore the density of the liquid phase was determined from the decrease of the melt level, which was visible after solidification (see fig. 3.12), and the meniscus height where the melt was sticking to the crucible inner wall. Assuming the mass of $DyScO_3$ had not changed after the melting process (i.e. no evaporation or other mass exchange), the density ρ_l of the liquid phase was estimated as

$$\rho_l = \rho_s \frac{V_s}{V_l} = \frac{m}{V_l}\ , \tag{3.1}$$

where subscript l denotes liquid and s the solid phase of $DyScO_3$. m is the mass of the solid phase, which was assumed to be the same as the mass of the liquid phase. V_s and V_l are the volumes of the solid and liquid phase, respectively. Five $DyScO_3$ melts were analysed and it could be found that $\rho_l \approx 6.12 g/cm^3$, which is about 10 % lower than ρ_s.

Figure 3.12: Solidified $DyScO_3$ melt with visible meniscus depth.

3.7 Summary and concluding remarks

The lack of physical properties for oxide materials with high melting point ($\approx$ 2000 °C) and the importance of these properties for numerical simulations were the motivation to perform measurements for obtaining some of these properties for a $DyScO_3$ melt. The IKZ Cz-equipment for growing oxide single crystals had been used for this experiments. The temperature on the melt surface could not be reliably measured using optical measuring equipment, i.e. pyrometer and/or IR camera system. The main problem was the evaporation of substances from the oxide melt, which condensed on the observing window and/or the fibre optics of the IR camera system, so that the heat radiation has been falsified. Therefore the temperature measurements had been done using self made Ir/Ir40%Rh thermocouples. Temperature measurement close to the outer crucible wall could not detect temperature fluctuations in the melt, but a vertical temperature gradient of 25 K/cm was measured during a real Cz crystal growth process outside the crucible wall. The measurement inside the $DyScO_3$ melt yielded the vertical temperature profile in the melt showing that the maximum melt temperature was located about 15 mm above the crucible bottom. The temperature measurement inside the melt had not been done during a real crystal growth process.
The same setup was used to measure the electrical conductivity of the melt. This yielded a value in the order of $10^{-7}\Omega^{-1}cm^{-1}$, but should be analysed more detailed because of the simple measurement setup used.
The Wilhelmy plate method had been applied for measuring the surface tension σ of $DyScO_3$ melt. The result was $\sigma \approx 1.421$ N/m measured at about 10 K above the melting temperature of $DyScO_3$. Its temperature dependence was approx. $-3.48 \cdot 10^{-4} N/m \cdot K$ in the temperature range $2070 - 2093$ °C,

which was larger than values of other oxide melts referenced in the literature [16, 111–113]. For comparison also σ measurements were made for a GGG melt. The surface tension of the GGG melt close to the melting point of about 1750 °C was 1.285 N/m with a temperature dependence of about $-2.76{\cdot}10^{-4} N/m{\cdot}K$ in the temperature range 1753-1840 °C. These values were similar to those of the $DyScO_3$ melt and that seems to be reasonable, because the flow pattern at the melt surface caused by the Marangoni convection was very similar and therefore the sensitivity for changes of σ must be about the same.
The dynamic viscosity of $DyScO_3$ melt had been measured using a rotary viscosimeter. This measurement yielded an averaged dynamic viscosity of about 49.86 $mPa \cdot s$, which was similar to the values of other oxide melts published in the literature [16, 16, 55, 112, 113]. For the viscosity measurement a rotary body was used with relatively large heat capacity, which caused "freezing" during its immersion into the melt. Therefore, in the future a smaller rotary body should be used. The density of the $DyScO_3$ solid phase was determined to be about $\rho_s \approx 6.79 g/cm^3$, and was about 10 % larger than the density of the liquid phase $\rho_l \approx 6.12 g/cm^3$. This was estimated using the melt level decrease inside the crucible, which was visible after solidification of the melt. The presented measurements had not been performed using special high precision equipment. However, the obtained physical properties of $DyScO_3$ melt should help getting more accurate numerical simulation results during the analysis of spiral crystal growth.
Finally one has to recognise that taking data of material properties from literature should be done with care. Some of them are only estimated and there are different values available for the same material. A collection of such data from literature together with those presented in the current work is given in tab. 3.7. Measurements for other important physical properties of $DyScO_3$ (e.g. thermal conductivity or heat capacity) should be done in the future. Nevertheless, these properties are needed for the numerical simulations, and are estimated for it (see tab. 3.7).

IKZ-measurements					
Property	**Units**	**$DyScO_3$**	**GGG**	**Nd:YAG**	**$LiNbO_3$**
T_{melt}	°C	2060	–	–	–
ρ_s	g/cm^3	6.79	–	–	–
ρ_l	g/cm^3	6.12	–	–	–
σ	N/m	1.421	1.285	0.709	0.317
T_σ	°C	2070	1753	1975	1283
$\frac{d\sigma}{dT}$	N/mK	$-3.48 \cdot 10^{-4}$	$-2.76 \cdot 10^{-4}$	$-7.5 \cdot 10^{-5}$	$-8.05 \cdot 10^{-5}$
η	mPas	49.86	–	62.0	42.5
α	1/K	$8.4 \cdot 10^{-6}$ [5]	–	–	–
β	1/K	$4.0 \cdot 10^{-5}$ (E)	–	–	–
λ_l	W/cmK	0.04 (E)	–	–	–
λ_s	W/cmK	0.3 (E)	–	–	–
c_p^l	J/gK	0.5 (E)	–	–	–
c_p^s	J/gK	0.65 (E)	–	–	–
ϵ_l	–	0.4 (E)	–	–	–
ϵ_s	–	0.3 (E)	–	–	–
κ	1/Ωcm	$2.1 \cdot 10^{-7}$	–	–	–
Data taken from literature					
Property	**Units**	**Al_2O_3**[111]	**GGG[16]**	**YAG**[55]	**$LiNbO_3$**[113]
T_{melt}	°C	2043	1750	1969 [112]	1253
ρ_s	g/cm^3	3.97 [58]	7.09 [119]	4.3	4.63 [120]
ρ_l	g/cm^3	3.05	5.65 [119]	3.6	3.631
σ	N/m	0.7	–	0.781 [112]	0.297
T_σ	°C	2043	1750	1970 [112]	1300
$\frac{d\sigma}{dT}$	N/mK	$-6.0 \cdot 10^{-5}$	–	$-3.5 \cdot 10^{-5}$ [112]	$-7.85 \cdot 10^{-5}$
η	mPas	2.72	40.0	46.0 [112]	38.0
α	1/K	$1.185 \cdot 10^{-5}$ [121]	–	–	–
β	1/K	$3.0 \cdot 10^{-5}$	$2.7 \cdot 10^{-5}$ [122]	$1.8 \cdot 10^{-5}$	$1.7 \cdot 10^{-4}$
λ_l	W/cmK	0.1	0.05	0.04	0.0309 [120]
λ_s	W/cmK	0.058 [58]	0.2	0.08	–
c_p^l	J/gK	1.26	0.586	0.8	1.02 [120]
c_p^s	J/gK	1.43 [58]	0.586	0.8	–
ϵ_l	–	0.33	0.3	0.3	0.3 [120]
ϵ_s	–	0.33	0.3	0.3	–
κ	1/Ωcm	–	–	–	–

Table 3.7: Measured and estimated (E) phys. properties compared to literature values (melting point T_{melt}, density ρ, surface tension σ, thermocap. coef. $d\sigma/dT$, σ-meas. temp. T_σ, dyn. visc. η, th. exp. coef. of crystal α and melt β, th. cond. λ, heat cap. c_p, emissivity ϵ, el. cond. κ) of some oxides, (s=solid, l=liquid).

Chapter 4

Numerical simulation of a real Cz crystal growth

The subject of chapter 2 of the current work was the analysis of the hydrodynamic stability of a sodium nitrate ($NaNO_3$) melt flow. This material was chosen, because its physical parameters are well known and it was studied extensively in the literature [35]. On the other hand it was a good reference for testing the two independent numerical tools of the German and Israeli research groups, respectively.
This chapter deals with the analysis of realistic Cz crystal growth concerning the hydrodynamic instability.

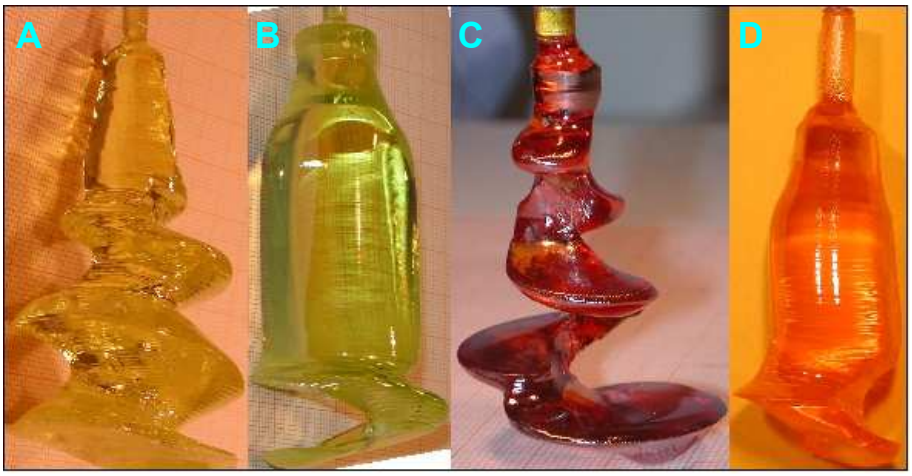

Figure 4.1: A: dysprosium scandate ($DyScO_3$) crystal showing extreme spiral growth, B: $DyScO_3$ crystal with later onset of spiral growth, C: samarium scandate ($SmScO_3$) with very distinctive spiral growth, D: $SmScO_3$ crystal with later onset of spiral growth.

In Fig. 4.1 examples of two state of the art materials can be seen having very high melting point ($\approx 2100\,^{\circ}C$) exhibiting spiral growth. It shows two rare earth scandate crystal materials, i.e. dysprosium scandate ($DyScO_3$) (A and B) and samarium scandate ($SmScO_3$) (C and D). Crystals A and C show an extreme and distinctive spiral growth, which were generated deliberately by growing with higher pulling rates. The two other crystals B and D also show spiral growth, but with later onset. Obviously, this onset must be connected with disturbances in the melt flow.
In order to simulate numerically realistic crystal growth of high melting point rare earth scandates appropriate physical parameters are needed. In chapter 3 the most important physical properties of $DyScO_3$ were determined experimentally, because no properties could be found in the literature or the physical properties of rare earth scandates were inaccurate or just estimated from other materials.

4.1 Simulation of Cz crystal growth including the RF induction heating

Here, the numerical analysis of the influence of the RF-heating configuration on the $DyScO_3$ melt flow is described. The term "configuration" means the variation of the RF-coil geometry, i.e. the relative height related to the crucible. Thereby, the electric parameters (current and frequency) are still controlled by the automatic growth unit of the crystal pulling machine.
The numerical simulation is done using the FEM package ENTWIFE [80] in three steps. In the first step the electromagnetic field has been calculated. Thereby, the in- and out-of-phase components $C(r,z)$ and $S(r,z)$ of the magnetic stream function ψ_B had to be calculated (see eq. (4.1)). This allows for a calculation of the generated heat density Q in metallic parts, i.e. iridium crucible and afterheater, in the next step. And in the last step the generated heat density $Q(r,z)$ (see eq. (4.2)) was used as a heat source in order to calculate temperature distribution and the melt flow. As long as the geometry is not changed, i.e. the geometry of coil and metallic parts (crucible and afterheater), the Q-distribution needs not to be recalculated. Other parameters like Grashof and Marangoni numbers or the Prandtl number can be changed, because they do not affect the initial heat source density Q. Fig. 4.2 shows the three steps applied in the following calculations. The steady states of the melt flow for different RF-heating configurations and different melt heights have been compared. Thereby, the focus was set on the analysis of possible hydrodynamic instabilities of the melt flow.

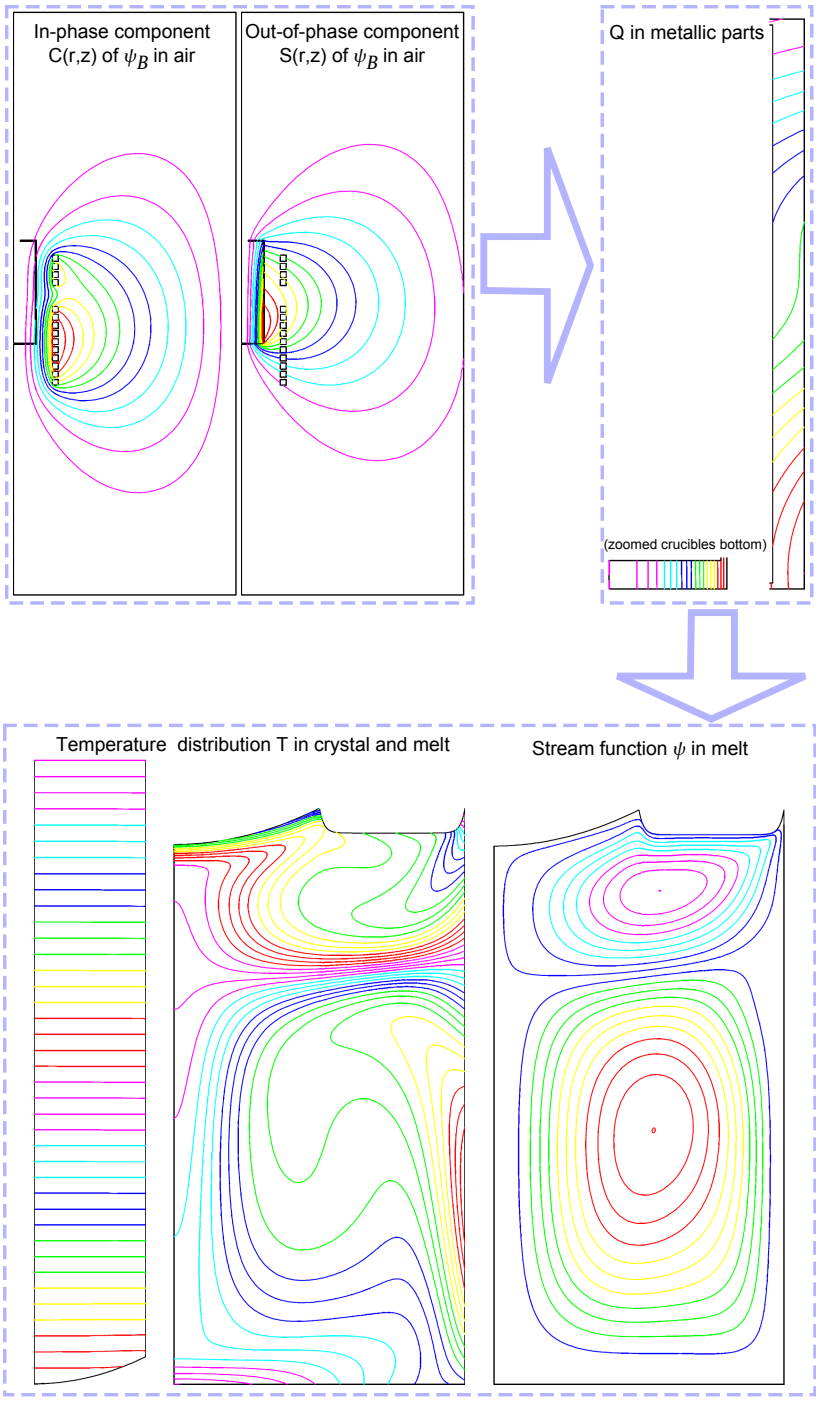

Figure 4.2: Principle steps of radio frequency (RF) coupling during the simulation of the melt flow. Calculating the in- and out-of-phase components $C(r, z)$ and $S(r, z)$ of ψ_B the heat density $Q(r, z)$ is computed. This is used in further calculations of temperature T and the stream function ψ.

4.1.1 Model problem and numerical method

The applied numerical model for the melt domain uses the same assumptions as the simple model in chapter 2. The model is axisymmetric and quasi steady state. It does not include internal and wall to wall radiation, but radiation boundary conditions at outside walls.
The induced heat density $Q(r,z)$ in the metallic parts, i.e. crucible and afterheater is calculated via the magnetic stream function ψ_B [54, 123–125] applying equation (4.1) and calculating the in-phase component $C(r,z)$ and out-of-phase component $S(r,z)$ of ψ_B.

$$\frac{\partial}{\partial r}\left(\frac{1}{r}\frac{\partial \psi_B}{\partial r}\right)+\frac{\partial}{\partial z}\left(\frac{1}{r}\frac{\partial \psi_B}{\partial z}\right)=\mu J \tag{4.1}$$

$$\text{where}\quad J=\begin{cases} J_0\cos\omega t & \text{in the coil} \\ -\frac{\sigma_c}{r}\frac{\partial \psi_B}{\partial t} & \text{in the conductors}\end{cases}$$

$$\text{with}\quad \psi_B = C(r,z)\cos(\omega t)+S(r,z)\sin(\omega t)$$

Thus, $Q(r,z)$ in the metallic parts is calculated using both components $S(r,z)$ and $C(r,z)$ (4.2).

$$Q=\frac{\sigma_c\omega^2}{2r^2}(C^2+S^2) \tag{4.2}$$

The flow in the melt and gas domain is governed by the Navier-Stokes equations applying the Boussinesq approximation (4.3). Conductive and convective heat transfer are described by (4.4) and (4.5). For the velocity components the continuity equation (4.6) holds .

$$\rho\vec{V}\cdot\nabla\vec{v}=-\nabla p+\mu\nabla^2\vec{v}+\rho\vec{g}(T-T_0)\beta \tag{4.3}$$

$$k\nabla^2 T_s+Q_s=0 \qquad s=\text{solid regions} \tag{4.4}$$

$$\frac{k}{\rho c_p}\nabla^2 T-\vec{v}\cdot\nabla T=0 \qquad \text{in melt and gas} \tag{4.5}$$

$$\nabla\cdot\vec{v}=0 \tag{4.6}$$

The thermocapillary convection at the free melt surface (melt/gas interface) is described by equation (4.7).

$$\mu_l\frac{\partial u_l}{\partial \hat{n}}-\mu_g\frac{\partial u_g}{\partial \hat{n}}=\frac{\partial\gamma}{\partial\hat{\tau}}=\frac{\partial\gamma}{\partial T}\frac{\partial T}{\partial\hat{\tau}} \tag{4.7}$$

The relation between the dimensionless melt flow velocity and the fluid stream function is given by eq. (4.8). This definition of the stream function is used for visualization of the melt flow. The non-dimensionalization of eq. (4.8) is done with $(U, V) = (u, v)/U_c$, where $U_c = \nu_l/R$.

$$U = \frac{1}{R}\frac{\partial \psi}{\partial Z} \qquad V = -\frac{1}{R}\frac{\partial \psi}{\partial R} \tag{4.8}$$

Furthermore, boundary conditions are set for the radiation heat loss from outer insulation surfaces using the Biot number Bi (4.13) and the radiation number Rad_i (4.14). Radiation heat loss on the melt surface is described by Rad_l (4.15). Heat transport at the melt/gas interface is described by the equations for the melt and gas flow. Internal radiation is not considered. At the afterheater top hole the temperature is set to the measured ambient temperature T_a. At crystal surfaces the radial and vertical velocity component vanishes ($u = v = 0$). The crystal rotation appears as boundary condition in the azimuthal velocity component ($w = r\,\omega_{crystal}$).
Fig. 4.3 on the right-hand side shows a sketch of the applied model geometry for calculating Q. The source of energy is the external generator, which supplies the RF coil with energy, i.e. electrical current with certain amplitude and a typical frequency of about $f = 10\,kHz$.
The electrical current is described by its density J (see equation (4.1)). The RF coil generates an electromagnetic field, which affects all metallic parts in the model. It mainly induces heat in the iridium crucible and afterheater, but also in the coil itself and in the steel chamber, which contains the Cz setup, via the strayed field. The gas (nitrogen) has no influence on the electromagnetic field due to its very small dielectric constant. The induced heat is calculated by solving the equation (4.1) and applying equation (4.2). For the calculation of Q the model does not contain melt, since the interaction of the electromagnetic field with the $DyScO_3$ melt can be neglected due to very bad electrical conductivity of the $DyScO_3$ melt. The simple measurement of the electrical conductivity of the $DyScO_3$ melt in chapter 3 confirms this (see tab. 3.1).
On the left-hand side of fig. 4.3 the applied FEM grid for calculating Q is shown. It contains up to 50000 T6/3 elements. The grid is coarse in the gas domain of the chamber, because the density of the electromagnetic field is relatively small there. On the other hand, around the iridium crucible and afterheater the grid has to be refined. Beside T6/3 elements with 6 triangle nodes, i.e. 6 quadratic and 3 linear nodes, also, Q9/4 elements with 9 quadratic nodes and 4 linear nodes has been used. An mapping algorithm is applied to fit the used elements to the complex geometry. Simulation results has shown, that for sufficient fine grid size the convergence of the solution

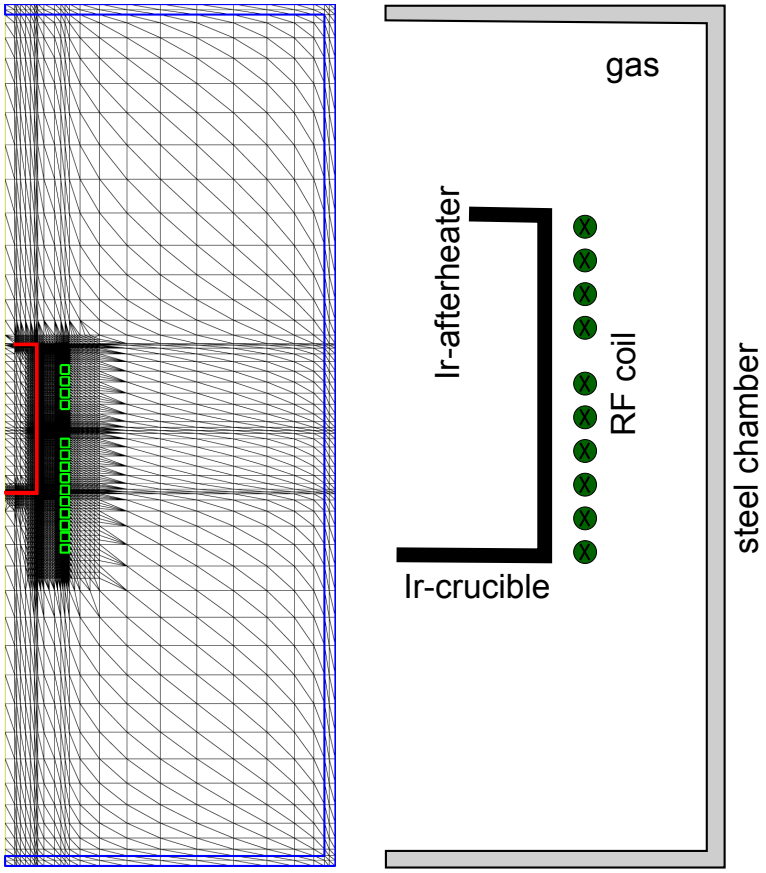

Figure 4.3: Sketch of the model geometry for calculating the heat density Q in metallic parts and the applied FEM grid.

was good enough with sufficient small residual values in both cases.
A sketch of the model geometry for calculating temperature distribution and flow in the melt and the gas is shown in fig. 4.4 (B). This axisymmetric model contains the crystal, the melt, the gas, the insulation and the metallic parts, i.e. iridium crucible and afterheater. The RF coil is shown in order to remember that this is the energy source for driving the Cz process. However, heat density Q was calculated first (see fig. 4.2) and then it was imported as boundary condition Q in the iridium crucible and the afterheater.
In fig. 4.4 (A) the applied FEM grid for calculating temperature distribution and flow in the melt and the gas is shown. It contains up to 65000 T6/3 elements. The grid is coarse in the insulation domain, but especially at interfaces (gas/liquid/solid) the grid has to be refined in order to resolve the boundary layers. Beside T6/3 elements with 6 triangle nodes, i.e. 6 quadratic and 3 linear nodes, also, Q9/4 elements with 9 quadratic nodes

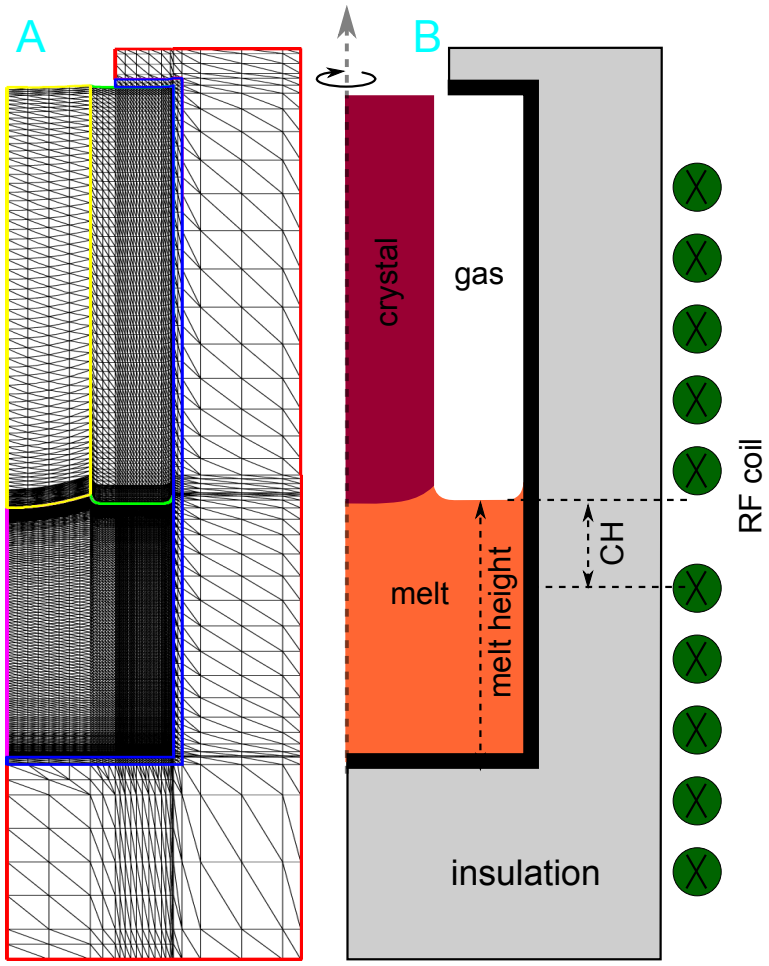

Figure 4.4: Sketch of the model geometry for calculating the temperature field and melt flow and the applied FEM grid (CH: relative coil height).

and 4 linear nodes has been used. Simulation results has shown, that for sufficient fine grid size the convergence of the solution was good enough with sufficient small residual values.
The advanced FEM package ENTWIFE [3] has been applied for numerical simulation. It uses a Newton-Raphson method combined with the direct solver MUMPS [82]).
Tab. 4.1 gives an overview about the applied operating parameters in the following simulations. The crucible radius $r = 29.25\,mm$ has been chosen as length scale and the $DyScO_3$ melting temperature as temperature scale. Another important parameter is the dimensionless rotational Reynolds number Re (4.12). For the $DyScO_3$ Cz process holds $Re \approx 0 - 330$ ($Re = 100 \approx 10\,rpm$).

Description	Symbol	Value	Units
crucible radius	r	29.25	mm
crucible height	h	58.0	mm
crucible wall thickness	w	1.5	mm
afterheater radius	r_{ah}	29.25	mm
afterheater height	h_{ah}	80.0	mm
afterheater wall thickness	w_{ah}	1.5	mm
afterheater top hole radius	r_{ah}	19.0	mm
chamber height	h_{ch}	800.0	mm
crystal radius	r_c	14.625	mm
melt height	h_m	10.0-54.0	mm
coil height relative to h_m	h_c	0-54.0	mm
crystal to crucible radii ratio	CCr	0.5	–
gravity	g	9.81	m/s^2
crystal rotation	Ω	0..30	1/min
angular frequency	$\omega = 2\pi \cdot \Omega$	0..188	1/min
rotational Reynolds number	$Re \approx 11 \cdot \Omega$	0..330	–

Table 4.1: Operating parameters used for calculations of geometry cases $1 - 5$.

The applied physical properties of the $DyScO_3$ melt and crystal, of the gas (N_2), of the metallic parts (crucible and afterheater) and of the insulation (ZrO_2 ceramic) are listed in tab. 4.2. The physical properties of the $DyScO_3$ melt are measured (see chapter 3) and some of them were estimated, because no corresponding values could be found in the literature. Other physical properties were taken from the literature (given in tab. 4.2). The main property is the melting temperature $T_m = 2060°C$. Other important properties like the kinematic viscosity ν (2.11) or the temperature dependence of the surface tension $d\sigma/dT$ are used implicitly through the parameters Grashof number Gr (4.9) and the Marangoni number Ma (4.11), respectively. The Prandtl number is given by the eq. (4.10).

$$Gr = \frac{g\beta T_m R^3}{\nu^2} \tag{4.9}$$

$$Pr = \frac{\nu}{\chi}, \quad \chi = \frac{k}{\rho c_p} \tag{4.10}$$

$$Ma = \frac{\left|\frac{d\sigma}{dT}\right| T_m R}{\eta\nu} \tag{4.11}$$

$$Re = \frac{\omega R^2}{\nu} \tag{4.12}$$

Property	Symbol	Value	Units
melting point	T_m	2333	K
density (crystal)	ρ_s	6.79	$g\,cm^{-3}$
density (melt)	ρ_l	6.12	$g\,cm^{-3}$
density (gas)	ρ_g	$3.5 \cdot 10^{-4}$ [126]	$g\,cm^{-3}$
dynamic viscosity (melt)	η	$4.986 \cdot 10^{-1}$	$g\,cm^{-1}\,s^{-1}$
dynamic viscosity (gas)	η	$4.0 \cdot 10^{-4}$ [126]	$g\,cm^{-1}\,s^{-1}$
kinematic viscosity (melt)	ν	$8.147 \cdot 10^{-2}$	$cm^2\,s^{-1}$
kinematic viscosity (gas)	ν	1.14 [126]	$cm^2\,s^{-1}$
surface tension	σ	1.421	$N\,m^{-1}$
temperature dependence of σ	$\gamma = \frac{d\sigma}{dT}$	$-3.48 \cdot 10^{-4}$	$N\,m^{-1}\,K^{-1}$
specific heat capacity (crystal)	c_p^s	0.5 (E)	$J\,g^{-1}\,K^{-1}$
specific heat capacity (melt)	c_p^l	0.65 (E)	$J\,g^{-1}\,K^{-1}$
specific heat capacity (gas)	c_p^g	1.14 [126]	$J\,g^{-1}\,K^{-1}$
thermal diffusivity (crystal)	χ_s	$1.3 \cdot 10^{-2}$	$cm^2\,s^{-1}$
thermal diffusivity (melt)	χ_l	$6.8 \cdot 10^{-2}$	$cm^2\,s^{-1}$
thermal diffusivity (gas)	χ_g	2.7 [126]	$cm^2\,s^{-1}$
vol. exp. coefficient (crystal)	α	$8.4 \cdot 10^{-6}$ [5]	K^{-1}
vol. exp. coefficient (melt)	β	$4.0 \cdot 10^{-5}$ (E)	K^{-1}
vol. exp. coefficient (gas)	β_g	$2.7 \cdot 10^{-3}$ [126]	K^{-1}
thermal conductivity (crystal)	λ_s	$3.0 \cdot 10^{-1}$ (E)	$Wcm^{-1}K^{-1}$
thermal cond. (melt)	λ_m	$4.0 \cdot 10^{-2}$ (E)	$Wcm^{-1}K^{-1}$
thermal cond. (gas)	λ_g	$1.1 \cdot 10^{-3}$ [126]	$Wcm^{-1}K^{-1}$
thermal cond. (insulation)	λ_i	$2.1 \cdot 10^{-2}$ [126]	$Wcm^{-1}K^{-1}$
thermal cond. (crucible)	λ_c	1.47 [126]	$Wcm^{-1}K^{-1}$
heat transfer coef. (insulation)	h_i	20.0 [126]	$Wcm^{-2}K^{-1}$
emissivity (crystal)	ϵ_s	0.3 (E)	–
emissivity (melt)	ϵ_l	0.4 (E)	–
emissivity (insulation)	ϵ_i	0.2 [126]	–
Prandtl number	Pr	6.23	–
Marangoni number	Ma	$2.506 \cdot 10^1\,T_m$	–
Grashof number	Gr	$1.4795 \cdot 10^2\,T_m$	–

Table 4.2: Measured and estimated (E) $DyScO_3$ crystal and melt properties (see tab. 3.7) and properties of iridium parts (crucible / afterheater), insulation ($ZrO2$) and gas (N_2).

$$Bi = \frac{h_i\, R}{\lambda_i} \tag{4.13}$$

$$Rad_i = \epsilon_i T^3 R/\lambda_i \tag{4.14}$$

$$Rad_l = \epsilon_l T^3 R/\lambda_l \tag{4.15}$$

The measured temperature difference across the free melt surface (melt/gas interface) is between 100K and 200K (see chapter 3) during the Cz process.

4.1.2 Results and discussion

The $DyScO_3$ melt height MH has been changed (1.0, 2.7, 5.4 cm) while the relative coil height to the melt level is fixed ($CH = 0$). Then, also CH has been changed (2.7, 4.4 cm) in order to match to the corresponding MH. Fig. 4.5 shows a sketch of all investigated configurations of the MH and CH.

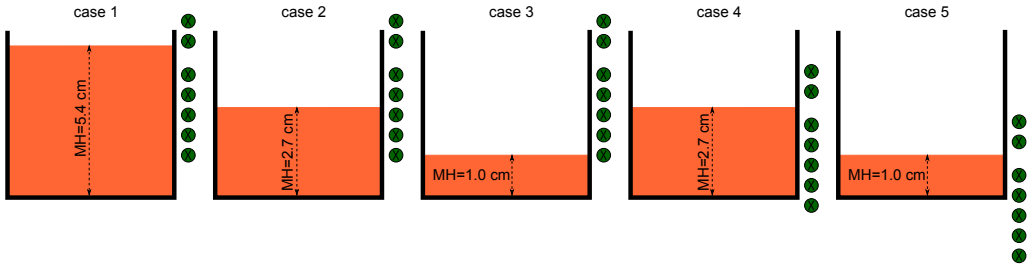

Figure 4.5: Different geometry configurations of melt height MH and RF-coils (cases $1-5$)

There was no significant influence of the variation of RF-heating configuration on the flow in the gas domain and on the temperature distribution in the crystal domain. Therefore, these results are not relevant and will not be discussed detailed here.

Geometry *case 1*

The model of *case 1* has the melt height $MH = 5.4\,cm$ and the coil height relative to the melt height is $CH = 0$. The RF-coil generates an electromagnetic field, which induces heat in the iridium crucible and afterheater, respectively. The simulation results are shown in fig. 4.6. The Q values are shown in the crucible wall and bottom and in the afterheater wall. This wall has a thickness of about 1.5 mm and a height of about 140 mm (see tab. 4.1). Because of this inappropriate ratio, only the crucible and afterheater wall is shown detailed. The maximum heat density Q_{max} was located about 15 mm above the bottom of the crucible [108]. This is reasonable because

of the good insulation and a good RF coupling. On the other hand the heat density value is smallest at top of the afterheater, because there is the top hole of the afterheater and the insulation is poor. So, in this region the temperature is smallest.

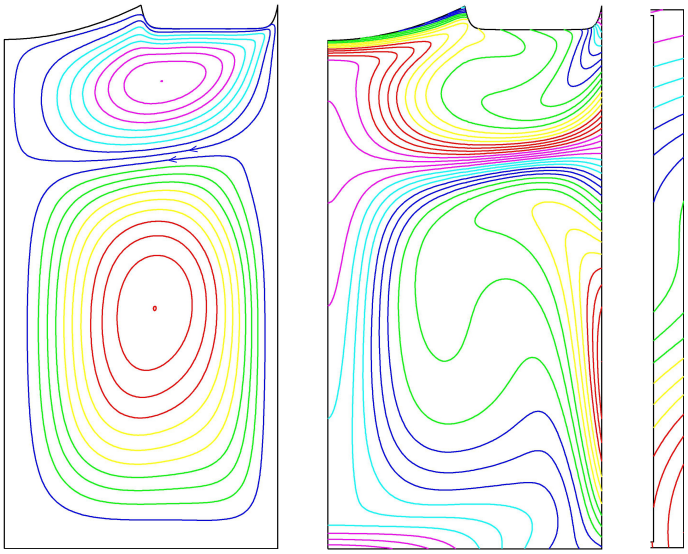

Figure 4.6: From left to right: stream function ($\psi_{min} = -0.413$; $\psi_{max} = 0.558$), melt isotherms ($T_{min} = 1.0$; $T_{max} = 1.0517$) and heat density ($Q_{min} = 8.59\,W/cm^3$; $Q_{max} = 163.23\,W/cm^3$) in the crucible and afterheater wall computed for case 1 (equidistant value distribution).

In the inductively heated crucible the $DyScO_3$ material melts. The temperature field in the melt is shown in fig. 4.6 (middle). The isotherms show that the temperature is highest at the crucible wall and becomes colder at the centre of the melt domain.
The thermal differences and the gravity cause a mass transport in the melt. This is visualized by the streamlines in fig. 4.6 (left-hand side). Beside the large eddy caused by thermal convection, there is also an eddy caused by forced convection via the crystal rotation. There is an interaction between the two eddies resulting in an exchange of energy. Especially at high temperature difference (ΔT) between the crucible wall and the crystal as well as around the equilibrium between thermal and rotational forces, the solution structure of the flow becomes more complex. The flow is characterized by a clockwise eddy, generated by the rotational forces and an anti-clockwise eddy generated by thermal forces.

Geometry *case 2*
The geometry of the RF coil is unchanged compared to *case 1*, i.e. the coil height relative to the melt height is $CH = -2.7\,cm$. This value is negative, because the MH was decreased from 5.4 to 2.7 cm. So, the melt surface and the three junction point (interface gas/liquid/solid) is now in a more homogeneously heated region.

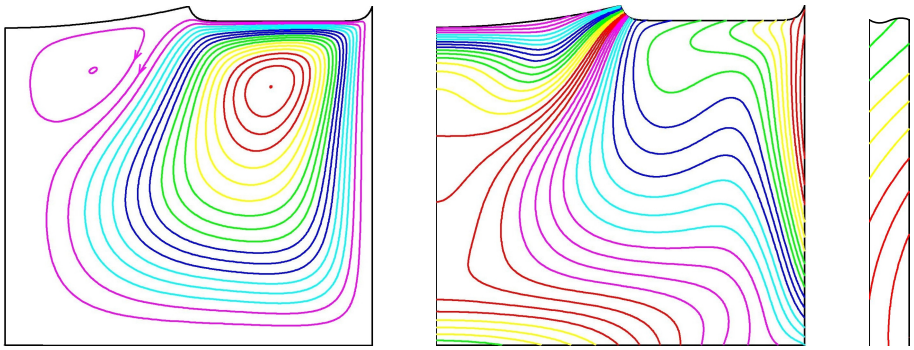

Figure 4.7: From left to right: stream function ($\psi_{min} = -0.0218$; $\psi_{max} = 0.3207$), melt isotherms ($T_{min} = 1.0$; $T_{max} = 1.0481$) and heat density ($Q_{min} = 101.66\,W/cm^3$; $Q_{max} = 152.49\,W/cm^3$) in the crucible and afterheater wall computed for case 2 (equidistant value distribution).

The inductively heated crucible and afterheater, respectively, have a volumetric heat density shown in fig. 4.7. The initial location of its maximum value Q_{max} is the same as in *case 1*, since the RF coil geometry is not changed. The whole melt is now in a homogeneously heated region, which is shown by the isotherms in fig. 4.7. In *case 2* the free melt surface and the three junction point, respectively, is now located where the maximum temperature is. Also, a change in the structure of the melt flow can be observed, because the height of the flow domain is now smaller ($MH = 2.7\,cm$). The clockwise eddy, generated by the rotational forces, has moved below the crystal and is now much smaller than the anti-clockwise eddy, which occupies most of the melt domain. So, the stagnation point moves below the crystal. This stagnation point shift influences the hydrodynamical stability [6].

Geometry *case 3*
The geometry of the RF coil is unchanged compared to *case 2* ($CH = -4.4\,cm$). This value is negative, because the MH was decreased from 5.4 to 1.0 cm. So, the melt surface and the three junction point (interface gas/liquid/solid) are closer to the crucible bottom.
Fig. 4.8 (right) shows the heat density Q in the inductively heated crucible and afterheater, respectively. The initial location of its maximum value Q_{max}

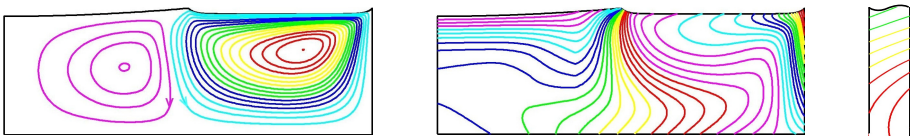

Figure 4.8: From left to right: stream function ($\psi_{min} = -0.0559$; $\psi_{max} = 0.2556$), melt isotherms ($T_{min} = 1.0$; $T_{max} = 1.0442$) and heat density ($Q_{min} = 101.73\,W$; $Q_{max} = 152.59\,W$) in the crucible and afterheater wall computed for case 3 (equidistant value distribution).

is the same as in *case 2*, since the RF coil geometry has not changed.
The melt is now in a very shallow domain ($MH = 1.0\,cm$). The highest temperature is located at the top right corner of the melt domain at the crucible wall, where the maximum value of the volumetric heat density in the crucible wall is located. The temperature changes in the melt are marginal, which is shown by the isotherms in fig. 4.8.
Compared to the *case 1* and *case 2* the melt flow structure is qualitatively different, because the height of the flow domain is much smaller ($MH = 1.0\,cm$). The clockwise eddy, generated by the rotational forces, completely has moved to a position below the crystal. The anti-clockwise eddy is completely located below the free melt surface. The stagnation point slightly moves to the right, but it is still below the crystal.

Geometry *case 4*
Compared to the *cases 1, 2* and *3* the geometry of the RF coil is now shifted down proportionally to the down shifting of the MH. Here, the MH is 2.7 cm, so that the CH is 0. So, the height of the melt surface and that of the three junction point (interface gas/liquid/solid) are about the same as the height of the RF coil gap, like in *case 1*.
On the right-hand side in fig. 4.9 a cutout of Q in the inductively heated crucible and afterheater is shown, respectively. Due to the fact that the RF coil is shifted down, the initial location of Q_{max} is about 5 mm shifted down compared to *case 1-3*. The crucible parts are located less in the main electromagnetic field, so that the RF coupling is weaker.
The highest temperature is located in the middle of the melt domain at the crucible wall, near the maximum value of the volumetric heat density in the crucible wall (see isotherms in fig. 4.7).
Compared to the *case 1-3* the melt flow structure is qualitatively different. The clockwise eddy, generated by the rotational forces, is very weak and completely in the melt domain below the crystal. The anti-clockwise eddy is completely below the free melt surface, but also extends to the melt domain

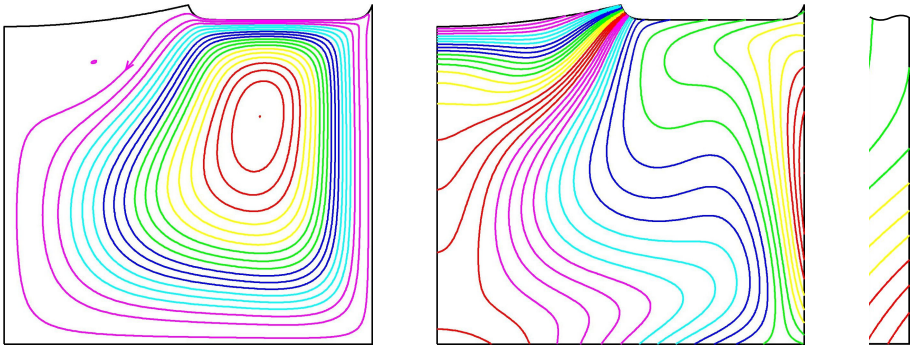

Figure 4.9: From left to right: stream function ($\psi_{min} = -0.0147$; $\psi_{max} = 0.3045$), melt isotherms ($T_{min} = 1.0$; $T_{max} = 1.0483$) and heat density ($Q_{min} = 99.35\,W/cm^3$; $Q_{max} = 188.77\,W/cm^3$) in the crucible and afterheater wall computed for case 4 (equidistant value distribution).

below the crystal, where it weakens the flow induced by the rotational forces. So, the stagnation point is completely in the melt domain below the crystal.

Geometry *case 5*
Compared to the *cases 4* the geometry of the RF coil is further shifted down proportionally to the down shifting of the MH. In *case 5* the MH is 1.0 cm, so that CH is 0. So, the height of the melt surface and that of the three junction point (interface gas/liquid/solid) are about the same as the height of the RF coil gap, like in *case 1*.

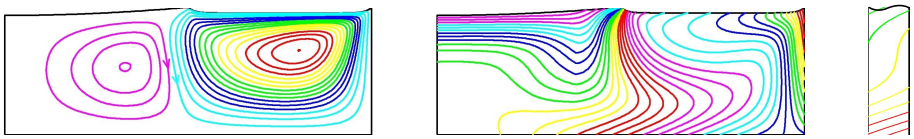

Figure 4.10: From left to right: stream function ($\psi_{min} = -0.0594$; $\psi_{max} = 0.2508$), melt isotherms ($T_{min} = 1.0$; $T_{max} = 1.0453$) and heat density ($Q_{min} = 119.91\,W/cm^3$; $Q_{max} = 179.87\,W/cm^3$) in the crucible and afterheater wall computed for case 5 (equidistant value distribution).

On the right-hand side in fig. 4.10 a cutout of Q in the inductively heated crucible and afterheater is shown, respectively. Due to the fact that the RF coil is shifted down, the initial location of Q_{max} is shifted down to the crucibles bottom corner (about 10 mm under the location of Q_{max} in *case 3* (see 4.8)). The crucible parts are located less in the main electromagnetic field, so that the RF coupling is weaker.
The melt is in a very shallow domain ($MH = 1.0\,cm$), like in *case 3*. The

highest temperature is located at the top right corner of the melt domain at the crucible wall, about at the same height as the afterheater RF-coil. (see isotherms in fig. 4.10).
Compared to the *case 1* and *case 2* the melt flow structure is qualitatively different, because the height of the flow domain is much smaller ($MH = 1.0\,cm$), but very similar to the flow in *case 3*. The clockwise eddy, generated by the rotational forces, completely has moved to a position below the crystal. The anti-clockwise eddy is completely below the free melt surface and only slightly extended to the melt domain below the crystal. So, the stagnation point slightly moves to the right, but it is still below the crystal.

Concluding remarks
There was no significant influence of the variation of the RF-heating configuration on the flow in the gas domain and on the heat transfer in the solid domain (crystal). While taking the relative height of the RF-coil related to the crucible constant and changing the melt height from $MH = 5.4$ via $MH = 2.7$ to $MH = 1.0\,cm$, it can be seen that a decrease of the melt height changes the position of the eddies (rotational and thermal forces), i.e. the interaction between the forces in the melt is being influenced.
Changing the geometry of the RF coil in the same proportions like the melt height causes a small shift of the stagnation point, which could influence the stability properties of the melt ([6]). The mean heat density in the metallic parts is in *case 2* and *case 3* about 10% larger than in *case 4* and *case 5*. The values of the stream function are similar in corresponding cases. Therefore, the conclusion is, that a matching of RF coil geometry to the melt height level has no significant effect on the melt flow.

4.2 Bifurcation analysis and continuation using $DyScO_3$ melt properties

In the previous section the influence of the RF coil configuration has been analysed in a few selected examples. Here, the focus is set on the analysis of the global melt flow solution structure applying bifurcation and continuation techniques [65].
For continuation the geometry model in fig. 4.4 has been simplified. Only the melt domain is considered, because the subject of this subsection is the hydrodynamic stability of the melt flow. In contrast to T6/3 elements Q9/4 elements have better approximation with 9 quadratic nodes and 4 linear nodes, so that the latter have shown a better convergence of the solution. Simulating the melt flow the grid size has to be refined for larger rotational

Reynolds numbers, which one can expect. The accuracy is shown by the fast convergence of the solution.
Physical properties of the $DyScO_3$ melt have been used (see tab. 4.2).
Path following uses a pseudo arclength algorithm (see [65]) to calculate solutions of the melt flow for a wide range of values of one parameter while all other parameters are fixed.
Two technologically important cases are considered. First the control parameter rotational Reynolds number Re (equivalent to the crystal rotation rate) is varied for fixed temperature difference along the free melt surface (gas/melt interface) ΔT (see section 2.1, eqs. (2.5) and (2.8)). In the second case the control parameter is ΔT (influenced by the modulation of the RF generator) and Re is held fixed. In both cases the continuation diagrams are plots of Re and ΔT vs. the total kinetic energy of the melt flow E_{kin} in the melt domain, which is determined by the dimensionless melt height H and crucible radius R (see eq.(4.16). This is a global measure for the melt flow solution behaviour, which is defined for comparison reasons.

$$E_{kin} = 2\pi \int_0^{HR}\int_0^{} \left(u^2 + v^2 + w^2\right) r dr dz \tag{4.16}$$

4.2.1 Continuation with control parameter Re

Taking the rotational Reynolds number Re as the control parameter four continuation diagrams have been computed using the FEM software package ENTWIFE [80].

***Case* $\mathbf{\Delta T = 50\,K}$**
The first continuation diagram is done for $\Delta T = 50K$. The result is shown in fig. 4.11. Using the physical properties of the $DyScO_3$ melt (see tab. 4.2), $Re = 100$ is equivalent to a crystal rotation rate of about $10\,rpm$. The curve in fig. 4.11 starts from $Re = 0$, where no rotational forces are acting and only thermal forces are present. Thus, the first value corresponds to the initial value of the temperature difference across the melt surface (here $\Delta T = 50K$). Increasing the rotational forces, the thermally induced convection becomes weaker, so that the curve decreases to a global minimum at about $Re = 145$.
This is the most sensitive region with respect to the hydrodynamic stability of the melt flow, since there is a strong competition between rotational forces induced by the external crystal rotation and thermal forces determined by the heat generation in the crucible. This can be seen in fig. 4.12, where streamlines of typical points in the region of multiple solutions are shown (A: lower branch at $Re = 135$, B: upper branch at $Re = 135$).

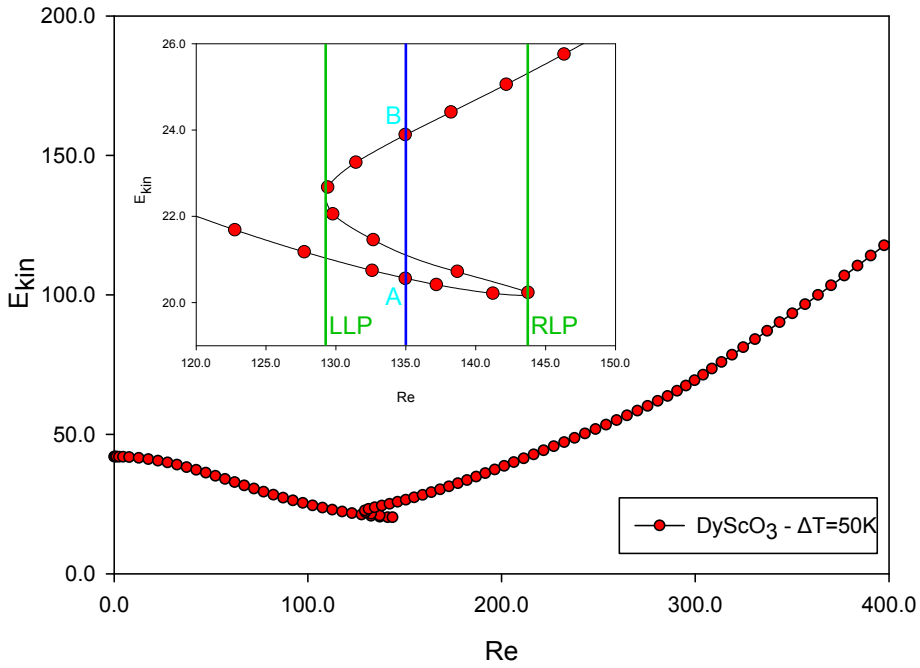

Figure 4.11: Path following diagram for the dysprosium scandate ($DyScO_3$) melt with $\Delta T = 50K$. (Re: rotational Reynolds number, E_{kin}: total kinetic energy of the melt flow, ΔT: temperature difference across the free melt surface)

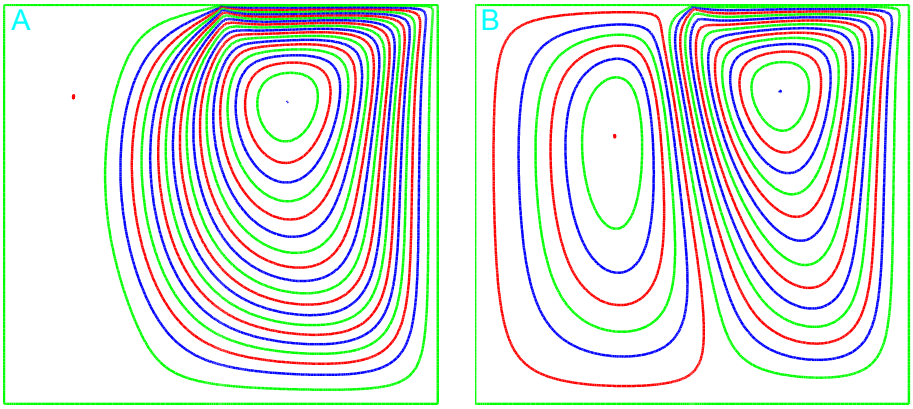

Figure 4.12: Streamlines of typical points in the region of multiple solutions for $\Delta T = 50K$. (A: lower branch at $Re = 135$, B: upper branch at $Re = 135$)

Fig. 4.11 also shows a detailed view of this region, which is delimited by the left limiting point (LLP) at $Re \approx 130$ and by the right limiting point (RLP) at $Re \approx 145$. For $Re > 145$ the total kinetic energy E_{kin} is rising and the rotational forces dominate the melt flow.

***Case* ΔT = 100 K**

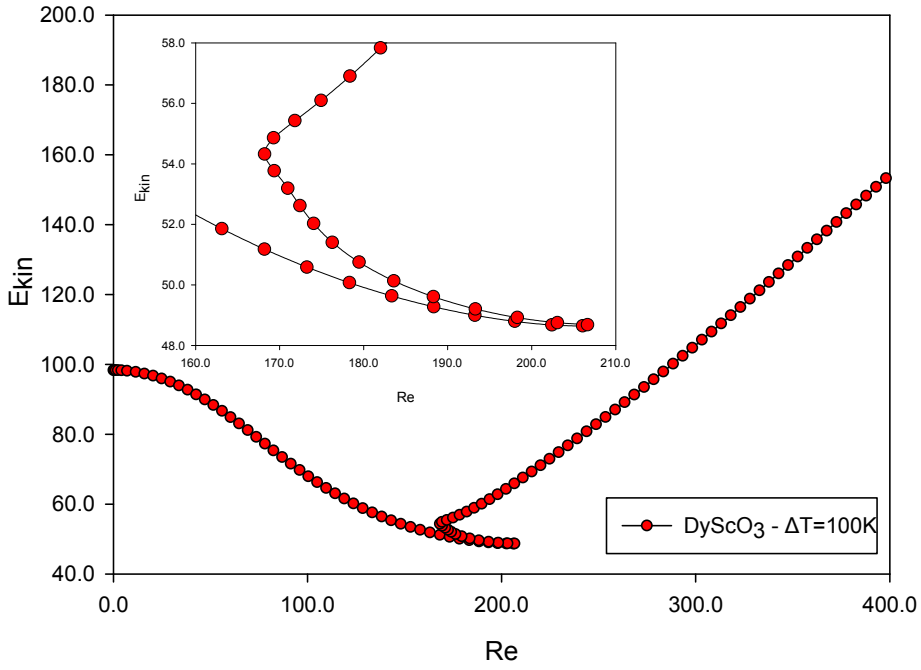

Figure 4.13: Path following diagram for the $DyScO_3$ melt with $\Delta T = 100K$. (Re: rotational Reynolds number, E_{kin}: total kinetic energy of the melt flow, ΔT: temperature difference across the free melt surface)

In fig. 4.13 results of the path following for $\Delta T = 100K$ are shown. The control parameter is Re, which is varied from 0 to 400. The most sensitive region, where thermal and rotational forces are in strong competition, is located between $Re \approx 170$ and $Re \approx 210$ (see cutout in fig. 4.13). This region has expanded compared to the previous study for $\Delta T = 50K$. This is reasonable, because the thermal forces are stronger. This is also the reason for the shift of the multiplicity region to higher Re.

***Case* ΔT = 150 K**

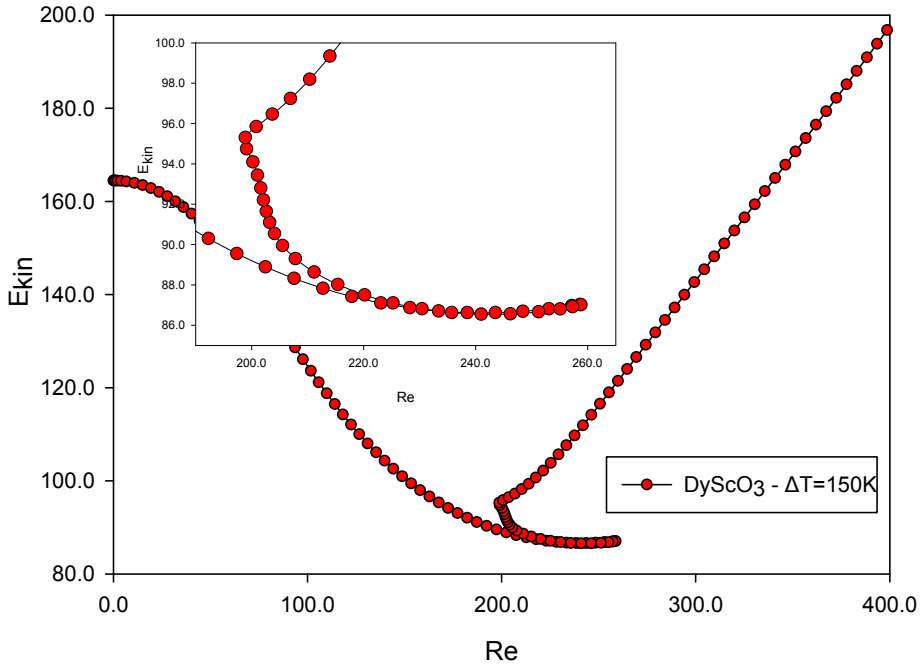

Figure 4.14: Path following diagram for the $DyScO_3$ melt with $\Delta T = 150K$. (Re: rotational Reynolds number, E_{kin}: total kinetic energy of the melt flow, ΔT: temperature difference across the free melt surface)

In the continuation diagram of fig. 4.14 the control parameter Re has been varied from 0 to 400. For $Re = 0$ the total kinetic energy is already very high, since the continuation study is done for large $\Delta T = 150K$.
The region with multiple solutions is located between $Re \approx 200$ and $Re \approx 260$. This interval is wider than in the previous continuation study for $\Delta T = 100K$. There melt flow instabilities are likely.

***Case* ΔT = 200 K**

Fig. 4.15 shows the fourth continuation diagram done for the control parameter Re and fixed $\Delta T = 200K$. Because of the high thermal forces it starts at $Re = 0$ with a high value of the total kinetic energy E_{kin} in the melt flow. With increasing Re the curve is falling rapidly into the region of multiplicities. This region containing multiple solutions is located between

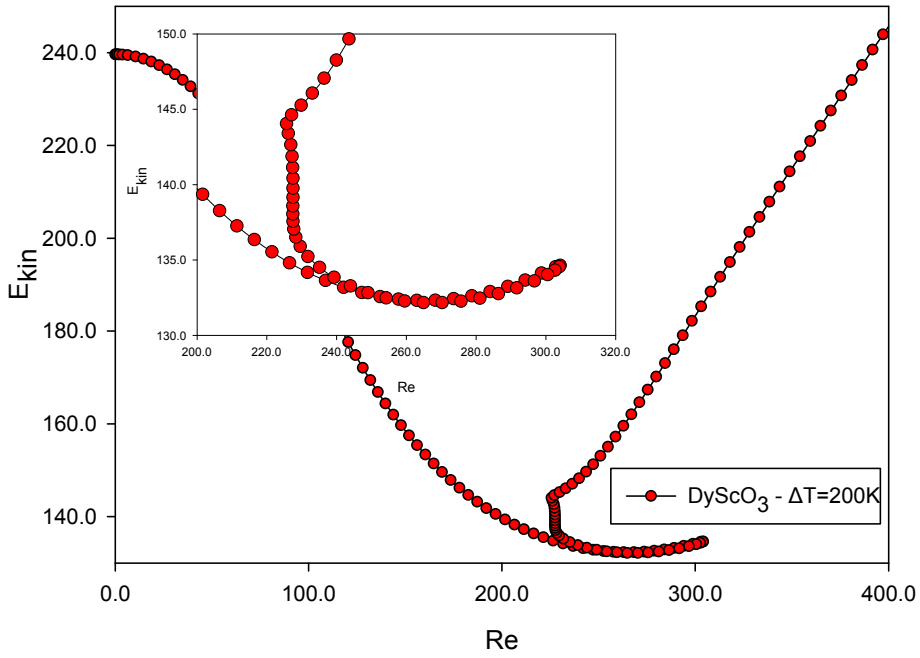

Figure 4.15: Path following diagram for the $DyScO_3$ melt with $\Delta T = 200K$. (Re: rotational Reynolds number, E_{kin}: total kinetic energy of the melt flow, ΔT: temperature difference across the free melt surface)

$Re \approx 235$ and $Re \approx 310$. This interval is wider than in the prior study made for $\Delta T = 150K$. The cutout in fig. 4.15 shows more detailed the qualitative change of the curve shape compared to the previous continuation diagram in fig. 4.14. Here the shape of the solution curve in the multiplicity region becomes more apparent. Solutions on the middle branch are linearly unstable. The global minimum of the diagram in fig. 4.15 is located at $Re \approx 260$.

4.2.2 Continuation with control parameter ΔT

Four path following diagrams have been computed for fixed rotational Reynolds number Re using the FEM package ENTWIFE [80]. Thereby, the temperature difference across the free melt surface ΔT has been chosen as control parameter, which is the driving force for the thermally induced flow.

Case Re=50

The first path following diagram is done for $Re = 50$ (fig. 4.16).

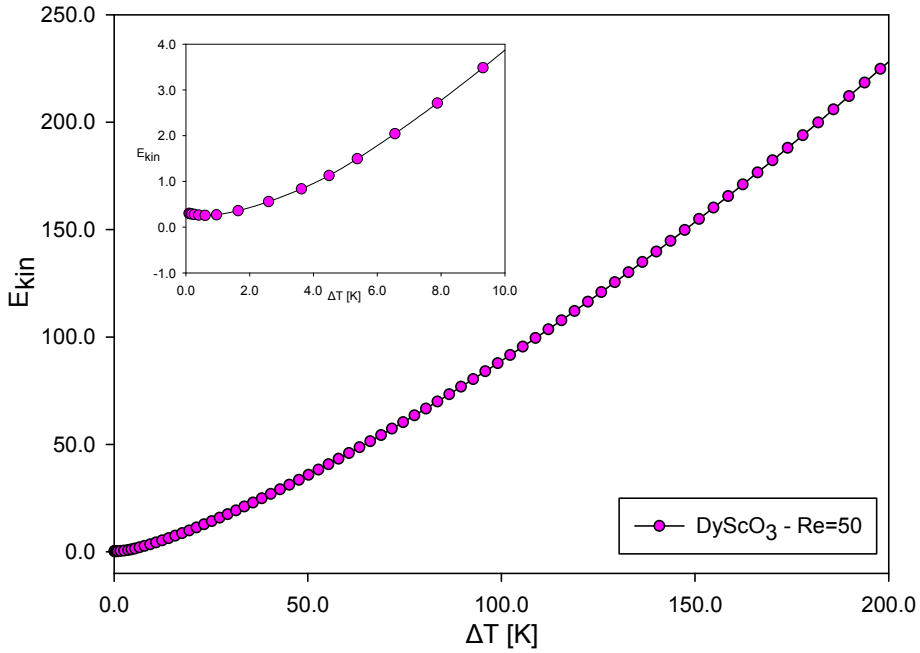

Figure 4.16: Path following diagram for the $DyScO_3$ melt with $Re = 50$. (Re: rotational Reynolds number, E_{kin}: total kinetic energy of the melt flow, ΔT: temperature difference across the free melt surface)

The physical parameters of $DyScO_3$ melt were used. During the Cz growth of $DyScO_3$ single crystals, typical temperature differences across the free melt surface (gas/melt interface) are between $\Delta T = 100K$ and $\Delta T = 200K$ (see. 4.2). So, typical temperature gradients between the crucible side wall and the crystal are between $70K/cm$ and $140K/cm$. The curve in fig. 4.16 starts from $\Delta T = 0K$, where the total kinetic energy of the melt flow is almost 0, because of the slow crystal rotation. Increasing the control parameter ΔT the curve exhibits a minimum for low ΔT (see the detailed cutout in fig. 4.16). For larger ΔT the curve is monotonically increasing without any solution multiplicities, so that the melt flow should be stable.

Case Re=100

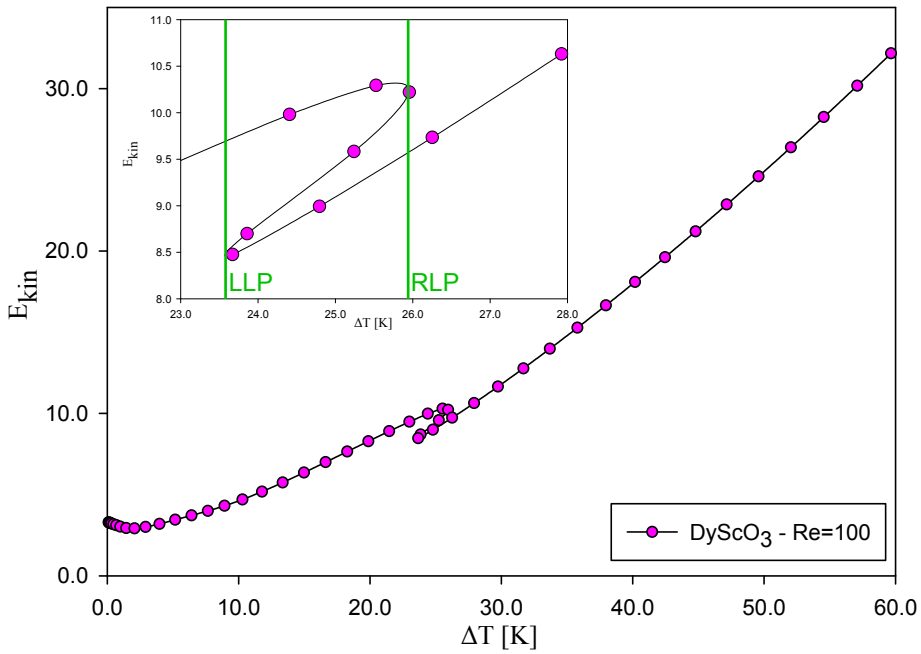

Figure 4.17: Path following diagram for the $DyScO_3$ melt with $Re = 100$. (Re: rotational Reynolds number, E_{kin}: total kinetic energy of the melt flow, ΔT: temperature difference across the free melt surface)

In fig. 4.17 the rotational forces have been increased to $Re = 100$. Therefore the curve starts with a certain total kinetic energy E_{kin} in the melt flow for $\Delta T = 0K$.
Increasing ΔT the forced convection induced by the rotational forces is being weakened by the thermally induced convection. At about $\Delta T = 3K$ the curve exhibits a minimum of the total kinetic energy. Apparently, for higher ΔT the melt flow becomes more complex. Solution multiplicity occurs between the left limiting point (LLP) at $\Delta T \approx 23K$ and the right limiting point (RLP) at $\Delta T \approx 26K$ (see the cutout in fig. 4.17).
The multiplicity region is sensitive in terms of melt flow stability, because linearly unstable solutions are possible. During the Cz process of the $DyScO_3$ single crystal $Re = 100$ ($\approx 10\,rpm$) is realistic, but the ΔT at which the multiple solutions occur is not. It could be realistic for the seeding process, so that the melt flow could become unstable.

Case Re=150

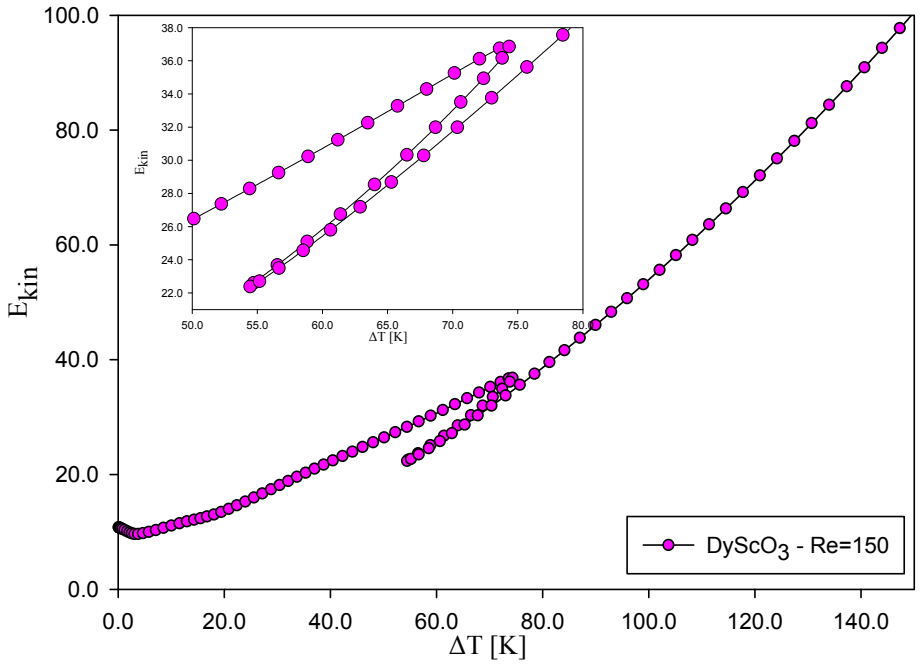

Figure 4.18: Path following diagram for the $DyScO_3$ melt with $Re = 150$. (Re: rotational Reynolds number, E_{kin}: total kinetic energy of the melt flow, ΔT: temperature difference across the free melt surface)

Fig. 4.18 shows a path following diagram for the control parameter ΔT for $Re = 150$. For $\Delta T = 0K$ the total kinetic energy E_{kin} in melt flow is slightly larger than in the previous study for $Re = 100$, because the rotational forces are larger. Again, E_{kin} first decreases for increasing ΔT to a global minimum and then it is rising for increasing ΔT.
The most sensitive region with multiple solutions occurs in the interval $\approx 55K \leq \Delta T \leq \approx 75K$. It became wider compared to the multiplicity region in the continuation diagram for $Re = 100$ (see fig. 4.17).

Case Re=200

In the last continuation diagram (fig. 4.19) the rotational Reynolds number is increased to $Re = 200$. So, the curve starts at $\Delta T = 0K$ with a larger E_{kin} than in the prior study for $Re = 150$. Also here, the curve exhibits a global minimum at $\Delta T \approx 5K$.

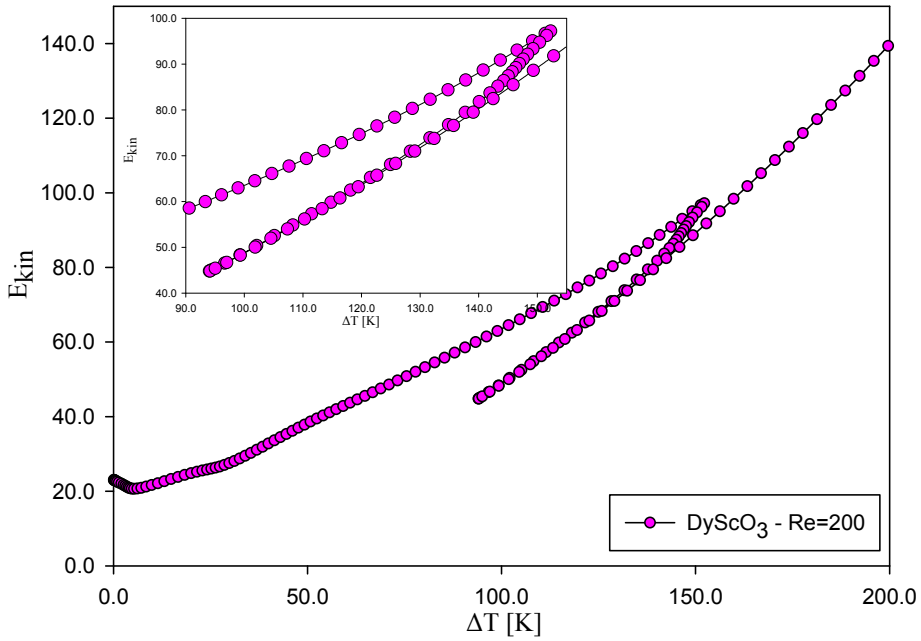

Figure 4.19: Path following diagram for the $DyScO_3$ melt with $Re = 200$. (Re: rotational Reynolds number, E_{kin}: total kinetic energy of the melt flow, ΔT: temperature difference across the free melt surface)

The multiplicity region became wider than in the prior study (fig. 4.18), and it has been shifted to higher ΔT values. This is reasonable, since the rotational forces are stronger and the competition with thermal forces is stronger, too.

4.3 Summary and concluding remarks

Continuation diagrams have been calculated in order to obtain an overview of the global solution behaviour in the $DyScO_3$ melt flow. Two cases have been considered. First the control parameter rotational Reynolds number Re has been varied, while the temperature difference across the free melt surface (gas/melt interface) ΔT was fixed ($\Delta T = 50$, 100, 150, 200 K). In the second case ΔT was the control parameter, which has been varied, and Re was fixed ($Re = 50$, 100, 150, 200).

In both cases there is a strong interaction between the flow induced by rotational forces and the thermally induced flow. Every continuation diagram has a region of multiple solutions, except the first path following diagram of the second case ($Re = 50$). This parameter combination seems to be stable for all analyzed ΔT intervals. In both cases there is the phenomenon, that the region of multiple solutions is shifted to higher values of the control parameter, when the fixed parameter has been increased. Also, the multiplicity interval becomes wider for larger control parameter, i.e. the melt flow is instability sensitive for a larger interval of parameter values.
The solution multiplicity region is enclosed by the limiting points. Outside this region an unique and linearly stable solution exists. Exactly at the limiting points two solutions exist, and in between three solutions. The multiplicity of solutions, which can be linearly stable or unstable, can be the prerequisite of melt flow instabilities, which could initiate spiral crystal growth.
In both cases there is a global minimum, which is connected to the interaction of thermally and rotationally induced melt flows. The difference is, that in the first case (control parameter Re) the global minimum is located in the region of solution multiplicities (see fig. 4.11−4.15) and in the second case (control parameter ΔT) the global minimum occurred in all four continuation diagrams (see fig. 4.16−4.19) very close to the symmetry axis ($\Delta T = 0K$).
The region of multiplicities is very sensitive in terms of melt flow instability. Especially when steep gradients (see detailed cutouts in fig. 4.11 − 4.19) are present in the solution, the numerical demands on the FEM grid accuracy and the computation times increase. For the crystal growth of the rare earth scandate $DyScO_3$ single crystal, it could be a problem during the seeding process at lower rotation rates, because a possible melt flow instability, which apparently can occur (see fig. 4.11), will produce a symmetry breaking at the very beginning of the crystal growth process.
During the regular crystal growth process, especially the step from one solution branch onto another, can be a source of symmetry breaking and spiral growth, because this branch could be linearly unstable. This change from one solution branch onto another could occur due to melt flow disturbances, e.g. disturbances of the heat transfer. Also, heat accumulation in the grown crystal, because of bad transparency properties, can disturb the heat transfer in the melt flow and lead to an unstable solution branch. Therefore, the most sensitive region in the continuation diagram is that where the distance between the solution branches is small, since it needs smaller disturbance amplitudes to produce a branch change, i.e. the invariance of the melt flow stability against disturbances becomes weaker.
Finally, it can be concluded that unstable parameter intervals do not occur

when either rotational or thermal forces dominate the melt flow, but will occur when the flow energies resulting from thermal and rotational forces, respectively, are of about equal order of magnitude.

Chapter 5

Summary and final remarks

Since a whole century material sciences and solid state physics are making enormous contributions to the technological progress in industry. Especially, since the invention of the transistor based on semiconductors about 60 years ago crystal growth gained rapidly on importance in industry and science.
Semiconductor materials cover about 90% of industry demand on single bulk crystals and about 10% is covered by oxide materials. Nevertheless, oxides are not replaceable for many applications, e.g. optoelectronics, sensor technologies or substrates for epitaxial growth. Especially, the demand on special oxides, i.e. rare earth scandates ($ReScO_3$), is growing during the last years, mainly for memory technologies (strain engineering). Rare earth substances can be $Re = La, Ce, Pr, Nd, Sm, Eu, Gd, Tb, Dy$. A very high melting point with $T_m > 2000\ ^\circ C$ is common for all rare earth scandates. This implies a non-trivial handling and requires for special operating conditions during the crystal growth, e.g. very good insulation. Bulk single rare earth scandate crystals are mainly used as substrates in epitaxial growth. Choosing a proper rare earth type crystals with a wide range of lattice constants can be grown [5, 6].
Beside the experimental challenges due to high operating temperatures and other problems like thermal stresses and chemical purity, the main problem during the Czochralski (Cz) growth of rare earth scandates is the tendency to spiral growth. The consequence is a premature stop of the growth process, i.e. a decrease of the yield.

In the present work reasons for the initiation process of the spiral crystal growth had to be investigated. Due to a very high melting point of rare earth scandates, the Cz setup requires an optimal insulation leading to bad observability of the growth process. Consequently, the reasons for spiral growth cannot be found applying experimental approaches. Therefore, it is

mandatory to apply numerical analysis of hydrodynamical instabilities in the melt.
The main hypothesis is that heat and momentum changes in the melt are initiating this unwanted process of spiral growth. In order to numerically model the realistic crystal growth of rare earth scandates the most important physical properties of the $DyScO_3$ melt had to be determined experimentally, because almost no properties could be found in the literature.
In chapter 2 the focus has been set on numerical analysis of a model melt with well known physical properties, i.e. $NaNO_3$. The melt temperature $T_m \approx 306\ ^\circ C$ is much smaller than the melt temperature of $DyScO_3$, but for the verification of the applied numerical code this has no influence. Since the hydrodynamical instability of the melt flow was under consideration only the melt domain as simple rectangle has been analysed. The realistic geometry like the shape of the liquid / solid interface has been neglected. The model describes the heat transfer and the melt flow by applying the Navier-Stokes-equations under Boussinesq approximation, the continuity equation and the energy equation. The temperature distribution was calculated and the melt flow has been simulated varying the main parameters. These are the rotational Reynolds number Re, which describes the forced convection induced by the rotation of the crystal and the temperature difference across the free melt surface ΔT, which describes the thermally induced convection in the melt.
Direct numerical Simulation (DNS) has been applied and "stability diagrams" have been calculated by looking for the last possible parameter combination (Re / ΔT) where the simulation algorithm is still converging. Also, transient simulation has been performed for different parameter sets. On one hand this is a very time consuming procedure and on the other hand it is not reliable, but this is the only way using generic FEM software packages. Why it is not reliable? Because, it could be shown, that in a region where the DNS only results in steady state solutions, also oscillatory solutions can occur. That means, that multiple solutions are possible. Therefore, the solution structure has been analysed intensively applying continuation and bifurcation techniques, respectively, which is novice in numerical simulation of the Czochralski crystal growth processes. These numerical tools allow for a much faster simulation than DNS, when the global solution overview is under consideration. Whereas a conventional Newton algorithm converges with order $O(h)^2$ the Hopf-bifurcation algorithm shows a super convergence with $O(h)^4$. The applied code is fully parallelized and could be run on a super computer with a total performance of 10 Tflops. Continuation diagrams show often a S-like shape, which is determined by limiting points. Outside this region the solution is unique and linearly stable, exactly on these points two

solutions exist and in between three solutions exist. Deeper analysis of the solutions applying eigenvalue analysis and calculation of Hopf bifurcation points only can decide about the solution stability. Hopf points are origins of oscillatory solution branches, i.e. periodic orbits. All results which are gained during the analysis of the $NaNO_3$ model were reproduced by an independent research group of Tel-Aviv University who used a FVM discretization instead of a FEM grid.
After the verification of the numerical tools using the simple $NaNO_3$ model a more comprehensive and realistic model of the $DyScO_3$ crystal growth has been implemented. For that the main physical properties of the $DyScO_3$ had to be measured, which is reported in chapter 3. This is a consequence of a lack of physical properties for oxide materials with high melting point ($\approx 2000\ ^\circ C$). The IKZ Cz-equipment for growing oxide single crystals has been used for these experiments.
The temperature on the melt surface could not be reliably measured using optical measuring equipment, i.e. pyrometer and/or an IR camera system. The main problem came from evaporated substances from the oxide melt which condensed on the observation window and/or the fibre optics of the IR camera system, so that the heat radiation had been falsified. Therefore the temperature measurements have been done using self made Ir/Ir40%Rh thermocouples. Temperature measurement close to the outer crucible wall can not detect temperature fluctuations in the melt, but a vertical temperature gradient of 25 K/cm was measured during a real Cz crystal growth process outside the crucible wall. The measurement inside the $DyScO_3$ melt yielded the vertical temperature profile in the melt showing that the maximum melt temperature is located about 15 mm above the crucible bottom. The temperature measurement inside the melt has not been done during a real crystal growth process.
The same setup was used to measure the electrical conductivity of the melt. This yielded a value in the order of $10^{-7}\Omega^{-1}cm^{-1}$, but has to be analysed more detailed because of the simple measurement setup used.
The Wilhelmy plate method has been applied for measuring the surface tension σ of $DyScO_3$ melt. The result was $\sigma \approx 1.421$ N/m measured at about 10 K above the melting temperature of $DyScO_3$. Its temperature dependence is approx. $-3.48 \cdot 10^{-4} N/m \cdot K$ in the temperature range $2070 - 2093\ ^\circ C$, which is larger than values of other oxide melts referenced in the literature. For comparison also σ measurements were made for a GGG melt. The surface tension of the GGG melt close to the melting point of about $1750\ ^\circ C$ is 1.285 N/m with a temperature dependence of about $-2.76 \cdot 10^{-4} N/m \cdot K$ in the temperature range $1753 - 1840\ ^\circ C$. These values are similar to those of the $DyScO_3$ melt and that seems to be reasonable, because the flow pattern

at the melt surface caused by the Marangoni convection is very similar and therefore the sensitivity for changes of σ must be about the same.
The dynamic viscosity of $DyScO_3$ melt has been measured using a rotary viscosimeter. This measurement yielded an averaged dynamic viscosity of about 49.86 $mPa \cdot s$, which is similar to the values of other oxide melts published in the literature.
The density of the $DyScO_3$ solid phase is determined to be about $\rho_s \approx 6.79 g/cm^3$, and is about 10 % larger than the density of the liquid phase $\rho_l \approx 6.12 g/cm^3$. This is estimated using the melt level decrease inside the crucible which is visible after solidification of the melt.
For the viscosity measurement a rotary body was used with relatively large heat capacity which caused "freezing" during its immersion into the melt. This required higher power rates for remelting. Therefore, in the future a smaller rotary body should be used. The presented measurements have not been performed using special high precision equipment. However, the obtained physical properties of $DyScO_3$ melt should help getting more accurate numerical simulation results during the analysis of spiral crystal growth which is still the goal of the presented work.
One has to recognise that taking data of material properties from literature should be done with care. Some of them are only estimated and there are different values available for the same material. Nevertheless, using the IKZ equipment it was not possible to carry out all properties needed for the numerical simulations, so that estimated values were used also (e.g. thermal conductivity or heat capacity).
After the measurements of important physical properties of the $DyScO_3$ melt a more comprehensive model has been implemented in chapter 4, which should take into account a more realistic geometry and the RF induction heating. The geometry describes beside the melt domain, a rounded crucible bottom, an afterheater with a flat baffle, the crystal, the gas domain, the insulation and the RF coils.
The influence of the height of the RF coils relative to the melt height on the melt flow has been analysed. Five different geometry cases have been considered. Each simulation has been performed in two steps. First, the components of the electromagnetic field generated by the RF coils have been calculated. This field induces heat in metallic parts, i.e. crucible and afterheater, which is then used in the second step to calculate the temperature distribution and the melt flow. There was no significant influence of the change of the RF coil height on the melt flow stability.
Considering only the melt flow domain path following diagrams have been calculated in order to get a qualitative overview about the solution structure. This has been done like in chapter 2 but now for a real oxide crystal ($DyScO_3$)

melting at about 2000 $^{\circ}C$. First the control parameter Re has been varied for fixed $\Delta T = 50$K, 100K, 150K, and 200K and then continuation diagrams with control parameter ΔT has been varied for fixed Re =50, 100, 150, and 200. In both cases regions of solution multiplicity could be localized, where also unstable solutions are possible. Outside these regions the solution is unique and stable and inside three solutions are possible, from which at least one is linearly unstable, which can be proved applying a linear stability analysis.
This model in combination with the bifurcation techniques cannot predict quantitatively exact parameter sets, which a crystal grower should use to avoid possible spiral growth, because the model still does not use all exact physical properties of the $DyScO_3$ melt. Also, not all important effects, especially the internal radiation in the crystal, which is apparently very important, are not considered. Experiments had shown that the spiral growth tendency is stronger for rare earth scandates with lower transparency at operating temperatures (e.g. $NdScO_3$) than for rare earth scandates with higher transparency at operating temperatures (e.g. $GdScO_3$) [6]. This means a realistic modelling will require a global 3D simulation of the entire Cz setup, which should be the goal for the future. However, the continuation diagrams had shown a multiplicity for realistic crystal rotation rates ($\Omega = 10..20\,rpm$) and this knowledge can be useful for the crystal grower.

Bibliography

[1] N. Crnogorac, H. Wilke, K.A. Cliffe, A.Yu. Gelfgat, and E. Kit. Numerical modelling of instability and supercritical oscillatory states in a czochralski model system of oxide melts. *Crystal Research and Technology*, 43:606, 2008.

[2] H.J. Scheel. Historical aspects of crystal growth technology. *Journal of Crystal Growth*, 211:1, 2000.

[3] K. Nassau. Dr. a. v. l. verneuil: The man and the method. *Journal of Crystal Growth*, 13/14:12, 1972.

[4] K. Byrappa and T. Ohachi. *Crystal Growth Technology.* Springer Verlag, 2003.

[5] R. Uecker, B. Velickov, et al. Properties of rare-earth scandate single crystals (re=nd–dy). *J. Cryst. Growth*, 310:2649, 2008.

[6] R. Uecker, H. Wilke, et al. Spiral formation during czochralski growth of rare-earth scandates. *Journal of Crystal Growth*, 295(1):84, 2006.

[7] W. Kossel. Über krystallwachstum. *Die Naturwissenschaften*, 18(44): 901, 1930.

[8] I.N. Stranski. Über die energieschwellen beim kristallwachstum. *Die Naturwissenschaften*, 37(13):289, 1950.

[9] M. Volmer and A. Weber. Keimbildung in übersättigten gebilden. *Z. f. phys. Chemie*, 119:277, 1926.

[10] J. Czochralski. Ein neues verfahren zur messung der kristallisationsgeschwindigkeit der metalle. *Z. phys. Chem.*, 92:219, 1918.

[11] C.D. Brandle. Czochralski growth of oxides. *Journal of Crystal Growth*, 264:593, 2004.

[12] J. Evers, P. Klüfers, R. Staudigl, and P. Stallhofer. Czochralskis schöpferischer fehlgriff: ein meilenstein auf dem weg in die gigabit-Ära. *Angewandte Chemie*, 115(46):5862, 2003.

[13] K.-Th. Wilke and J. Bohm. *Kristallzüchtung*, volume 2. Harri Deutsch, 1988.

[14] P. Capper. *Bulk Crystal Growth of Electronic, Optical and Optoelectronic Materials*. John Wiley and Sons, 2005.

[15] R.F. Belt, R.C. Puttbach, and D.A. Lepore. Crystal growth and perfection of large nd:yag single crystals. *Journal of Crystal Growth*, 13-14: 268, 1972.

[16] J.J. Derby and Q. Xiao. Some effects of crystal rotation on large-scale czochralski oxide growth: analysis via a hydrodynamic thermal-capillary model. *J. Cryst. Growth*, 113(3-4):575, 1991.

[17] F.E. Rosenberger. *Fundamentals of Crystal Growth*. Springer Verlag, 1979.

[18] J.C. Brice. *Crystal Growth Processes*. Blackie, 1986.

[19] H. Arend. *Crystal Growth in Science and Technology*. Plenum Press, 1989.

[20] D.T.J. Hurle. *Crystal Pulling from the Melt*. Springer Verlag, 1993.

[21] D.T.J. Hurle. *Handbook of Crystal Growth*, volume A-B. North-Holland, 1993-1994.

[22] R. Fornari. *Theoretical and Technological Aspects of Crystal Growth*. Trans. Tech. Publ., 1998.

[23] H.J. Scheel and T. Fukuda. *Crystal Growth Technology*. Wiley, 2003.

[24] N.Jr. Holonyak. *Solid state physical electronics series*. Prentice-Hall, 1970.

[25] R.F. Strickland-Constable. *Kinetics and Mechanisms of Crystallization*. Academic Press, 1968.

[26] I. Tarjan and M. Matrai. *Laboratory manual on crystal growth*. Academic Press, 1968.

[27] R. Narayanan and D. Schwabe. *Interfacial Fluid Dynamics and Transport Processes*. Springer Verlag, 2003.

[28] Z. Galazka and H. Wilke. Influence of marangoni convection on the flow pattern in the melt during growth of $y_3al_5o_{12}$ single crystals by the czochralski method. *Journal of Crystal Growth*, 216(1-4):389, 2000.

[29] K. Takagi and T. Fukuzawa. Effect of growth conditions on the shape of $bi_4ge_3o_{12}$ single crystals and on melt flow patterns. *Journal of Crystal Growth*, 76(2):328, 1986.

[30] H. Wilke, N. Crnogorac, and K.A. Cliffe. Numerical study of hydrodynamical instabilities during growth of dielectric crystals from the melt. *Journal of Crystal Growth*, 303:246, 2007.

[31] A.Yu. Gelfgat, A. Rubinov, P.Z. Bar-Yoseph, and A. Solan. Numerical study of three-dimensional instabilities in a hydrodynamic model of czochralski growth. *Journal of Crystal Growth*, 275:e7, 2005.

[32] P.H.O Rappl, L.F.M. Ferraz, H.J. Scheel, M.R.X. Barros, and D. Schiel. Hydrodynamic simulation of forced convection in czochralski melts. *Journal of Crystal Growth*, 70(1-2):49, 1984.

[33] Q. Xiao and J.J. Derby. Bulk-flow versus thermal-capillary models for czochralski growth of semiconductors. *Journal of Crystal Growth*, 129 (3-4):593, 1993.

[34] K. Kakimoto, M. Eguchi, H. Watanabe, and T. Hibiya. Flow instability of molten silicon in the czochralski configuration. *Journal of Crystal Growth*, 102(1-2):16, 1990.

[35] D. Schwabe, R.R. Sumathi, and H. Wilke. An experimental and numerical effort to simulate the interface deflection of yag. *Journal of Crystal Growth*, 265:440, 2004.

[36] D. Schwabe, R.R. Sumathi, and H. Wilke. The interface inversion process during the czochralski growth of high melting point oxides. *Journal of Crystal Growth*, 265:494, 2004.

[37] X. Wu, X. Geng, and Z. Guo. Fundamental study of crystal/melt interface shape change in czochralski crystal growth. *Journal of Crystal Growth*, 169(2):786, 1996.

[38] S.L. Baldochi, V.L Mazzocchi, C.B.R. Parente, and S.P. Morato. Study of the crystalline quality of czochralski grown barium lithium fluoride single crystals. *Journal of Crystal Growth*, 29(12):1321, 1994.

[39] B. Cockayne, M. Chesswas, and D.B. Gasson. Facetting and optical perfection in czochralski grown garnets and ruby. *Journal of Materials Science*, 4(5):450, 1969.

[40] I.M. Dawson and V. Vand. The observation of spiral growth-steps in n-paraffin single crystals in the electron microscope. *Proceedings of the Royal Society of London. Series A, Mathematical and Physical Sciences*, 206(1087):555, 1951.

[41] I.M. Dawson. The study of crystal growth with the electron microscope. ii. the observation of growth steps in the paraffin n-hectane. *Proceedings of the Royal Society of London. Series A, Mathematical and Physical Sciences*, 214(1116):72, 1952.

[42] M.H.J. Hottenhuis and C.B. Lucasius. The influence of impurities on crystal growth; in situ observation of the 010 face of potassium hydrogen phthalate. *Journal of Crystal Growth*, 78(2):379, 1986.

[43] B. Van Der Hoek, J.P. Van Der Eerden, P. Bennema, and I. Sunagawa. The influence of stress on spiral growth. *Journal of Crystal Growth*, 58 (2):365, 1982.

[44] H.P. Strunk. Edge dislocations may cause growth spirals. *Journal of Crystal Growth*, 160(1-2):184, 1996.

[45] H. Machida, K. Hoshikawa, and T. Fukuda. Spiral growth of rutile single crystal boules in the edge-defined, film-fed growth process. *Journal of Crystal Growth*, 137(1-2):82, 1994.

[46] J-P. Chaminade, O. Viraphong, and S. Miyazawa. One possible mechanism of spiral/footing growth of cz-grown $li_6gd(bo_3)_3$. *Journal of Crystal Growth*, 237-239(1):864, 2002.

[47] V.V. Kochurikhin, K. Shimamura, and T. Fukuda. The influence of dopants on the interface stability during $dy_3ga_5o_{12}$ single crystal growth. *Journal of Crystal Growth*, 143(3-4):232, 1994.

[48] S. Erdei and V.T. Gabrieljan. The twisting of $linbo_3$ single crystals grown by the czochralski method. *Crystal Research and Technology*, 24 (10):987, 1989.

[49] H. Cong, H. Zhang, S. Sun, Y. Yu, W. Yu, H. Yu, J. Zhang, J. Wang, and R.I. Boughton. Morphological study of czochralski-grown lanthanide orthovanadate single crystals and implications on the mechanism of bulk spiral formation. *Journal of Applied Crystallography*, 43: 308, 2010.

[50] N. Crnogorac and H. Wilke. Measurement of physical properties of $dysco_3$ melt. *Crystal Research and Technology*, 44(6):581, 2009.

[51] P. Hintz, D. Schwabe, and H. Wilke. Convection in a czochralski crucible - part 1: non-rotating crystal. *Journal of Crystal Growth*, 222: 343, 2001.

[52] U. Krzyminski and A.G. Ostrogorsky. Visualization of convection in czochralski melts using salts under realistic thermal boundary conditions. *Journal of Crystal Growth*, 174(1-4):19, 1997.

[53] V. Nikolov, K. Iliev, and P. Peshev. Relationship between the hydrodynamics in the melt and the shape of the crystal/melt interface during czochralski growth of oxide single crystals. *Journal of Crystal Growth*, 89(2-3):313, 1988.

[54] J.J. Derby, L.J. Atherton, and Gresho P.M. An integrated process model for the growth of oxide crystals by the czochralski method. *Journal of Crystal Growth*, 97(3-4):792, 1989.

[55] Q. Xiao and J.J. Derby. Heat transfer and interface inversion during the czochralski growth of yttrium aluminum garnet and gadolinium gallium garnet. *J. Cryst. Growth*, 139:147, 1994.

[56] W.E. Langlois. Digital simulation of czochralski bulk flow in microgravity. *Journal of Crystal Growth*, 48:25, 1980.

[57] M. Mihelcic, C. Schroeck-Pauli, K. Wingerath, H. Wenzl, W. Uelhoff, and A. Van Der Hart. Numerical simulation of forced convection in the classical czochralski method, in acrt and cacrt. *Journal of Crystal Growth*, 53:337, 1981.

[58] H. Kopetsch. Numerical simulation of the interface inversion in czochralski growth of oxide crystals. *Journal of Crystal Growth*, 102: 505, 1990.

[59] M.H. Tavakoli and H. Wilke. Numerical investigation of heat transport and fluid flow during the seeding process of oxide czochralski crystal

growth, part 1: non-rotating seed. *Crystal Research and Technology*, 42(6):544, 2007.

[60] M.H. Tavakoli and H. Wilke. Numerical investigation of heat transport and fluid flow during the seeding process of oxide czochralski crystal growth, part 2: rotating seed. *Crystal Research and Technology*, 42(7): 688, 2007.

[61] R.B. Lehoucq and A.G. Salinger. Large-scale eigenvalue calculations for stability analysis of steady flows on massively parallel computers. *J. Num. Meth. Fluids*, 36:309, 2001.

[62] Y. Feldman and A.Yu. Gelfgat. On pressure-velocity coupled time-integration of incompressible navier-stokes equations using direct inversion of stokes operator or accelerated multigrid technique. *Computers and Structures*, 87:710, 2009.

[63] K.A. Cliffe, T.J. Garratt, and A. Spence. Eigenvalues of the discretized navier-stokes equation with application to the detection of hopf bifurcations. *Advances in Computational Mathematics*, 1:337, 1993.

[64] P.M. Gresho, D.K. Gartling, J.R. Torczynski, K.A. Cliffe, K.H. Winters, T.J. Garratt, A. Spence, and J.W. Goodrich. Is the steady viscous incompressible twodimensional flow over a backward-facing step at re=800 stable? *J. Num. Meth. Fluids*, 17:501, 1993.

[65] K.A. Cliffe, A. Spence, and S.J. Tavener. The numerical analysis of bifurcation problems with application to fluid dynamics. *Acta Numerica*, page 39, 2000.

[66] E.L. Allgower and K. Georg. *Introduction to Numerical Continuation Methods*. SIAM, 45 edition, 2003.

[67] A.F. Mills. *Heat and Mass Transfer*. IRWIN, 1995.

[68] M. Rappaz, M. Bellet, and M. Deville. *Numerical Modeling in Materials Science and Engineering*. Springer Verlag, 32 edition, 2003.

[69] Q. Xiao and J.J. Derby. The role of internal radiation and melt convection in czochralski oxide growth: deep interfaces, interface inversion, and spiraling. *Journal of Crystal Growth*, 128(1-4):188, 1993.

[70] O. Budenkova, M. Vasiliev, V. Yuferev, and V. Kalaev. Effect of internal radiation on the solid-liquid interface shape in low and high thermal

gradient czochralski oxide growth. *Journal of Crystal Growth*, 303(1): 156, 2007.

[71] T. Cebeci. *Convective Heat Transfer*. Springer Verlag, 2 edition, 2002.

[72] T. Roger. *Navier-Stokes equations: theory and numerical analysis*. American Mathematical Society, 2 edition, 1984.

[73] F. Kohlrausch. *Praktische Physik*. B.G. Teubner Stuttgart, 1985.

[74] J. Folta. Some remarks on the history of numerical analysis especially in the area of prague. *LLULL:Revista de la Sociedad Espanola de Historia de las Ciencias y de las Tecnicas*, 11(21):217, 1988.

[75] V. Karpenko. Two thousand years of numerical magic squares. *Endeavour*, 18(4):147, 1994.

[76] P.G. Ciarlet and J.L. Lions. *Handbook of Numerical Analysis*. North-Holland, 2003.

[77] H.C. Elman, D.J. Silvester, and A.J. Wathen. *Finite Elements and Fast Iterative Solvers*. Oxford University Press, 2005.

[78] F. Thomasset. *Implementation of Finete Element Methods for Navier-Stokes Equations*. Springer Verlag, 1981.

[79] C.A.J. Fletcher. *Computational Galerkin Methods*. Springer Verlag, 1984.

[80] K.A. Cliffe. Entwife. http://www.sercoassurance.com/entwife, 2001.

[81] K.A. Cliffe. *ENTWIFE Reference Manual*. Serco Assurance, 7.3 edition, July 2005.

[82] P. Amestoy et al. *MUMPS user guide*. CERFACS, INPT and RAL, 4.9.2 edition, Nov 2009.

[83] Y.A. Kuznetsov. *Elements of Applied Bifurcation Theory*. Springer-Verlag, 1995.

[84] G. Iooss and D.D. Joseph. *Elementary stability and bifurcation theory*. Springer Verlag, 2 edition, 1997.

[85] C.S. Morawetz, J.B. Serrin, and Y.G. Sinai. *Selected Works of Eberhard Hopf with Commentaries*. American Mathematical Society, 2002.

[86] E. Hopf. Abzweigung einer periodischen Lösung von einer stationären Lösung eines Differentialsystems. *Berichte der Mathematisch-Physischen Klasse der Sächsischen Akademie der Wissenschaften zu Leipzig*, 94:1, 1942.

[87] R. Seydel. *Practical bifurcation and stability analysis: from equilibrium to chaos*. Springer Verlag, 2 edition, 1994.

[88] H. B. Keller. Numerical solution of bifurcation and nonlinear eigenvalue problems. *Applications of Bifurcation Theory (ed. P. H. Rabinowitz)*, page 359, 1977.

[89] P.H. Rabinowitz. *Applications of Bifurcation Theory*. Academic Press, 1977.

[90] H.B. Keller. *Lectures on Numerical Methods in Bifurcation Problems*. Springer Verlag, 1987.

[91] K.A. Cliffe. *ENTWIFE Installation and Running Guide*. Serco Assurance, 7.3 edition, July 2005.

[92] Wolfram Research. Wolfram mathematica documentation center. http://reference.wolfram.com/legacy/v5_2/, 2005.

[93] Maplesoft. Maple documentation center. http://www.maplesoft.com/documentation_center/, 2005.

[94] K.H. Winters and C.P. Jackson. *A Guide To Finite-Element Grid Generation using TGIN*. Theoretical Physics Divison - AERE Harwell, release 1 edition, Oct 1984.

[95] C.W. Gear. *Numerical Initial Value Problems in Ordinary Differential Equations*. Prentice Hall, 1971.

[96] A.Yu. Gelfgat. Studies on flow of instabilities in bulk crystal growth. *Transworld Research Network*, 2007.

[97] M. Teitel, D. Schwabe, and A.Yu. Gelfgat. Experimental and computational study of flow instabilities in a model of czochralski growth. *Journal of Crystal Growth*, 310:1343, 2008.

[98] A.Yu. Gelfgat, P.Z. Bar-Yoseph, and A. Solan. Stability of confined swirling flow with and without vortex breakdown. *J. Fluid Mech.*, 311: 1, 1996.

[99] A.Yu. Gelfgat, P.Z. Bar-Yoseph, and A. Solan. Three-dimensional instability of axisymmetric flow in a rotating lid - cylinder container. *J. Fluid Mech.*, 438:363, 2001.

[100] Peter Hintz. *Konvektion im Czochralski-Tiegel.* PhD thesis, I. Physikalisches Institut der Justus-Liebig-Universität Giessen, 1999.

[101] A.Yu. Gelfgat and P.Z. Bar-Yoseph. Multiple solutions and stability of confined convective and swirling flows - a continuing challenge. *Int. J. Numer. Meth. Heat and Fluid Flow*, 14:213, 2004.

[102] B. Werner and A. Spence. The computation of symmetry breaking bifurcation points. *SIAM J. Numer. Anal.*, 21:388, 1984.

[103] A. Griewank and G. Reddien. Characterization and computation of generalized turning points. *SIAM J. Numer. Anal.*, 21:176, 1984.

[104] Cyberstar. Czochralski puller. http://www.cyberstar.fr/telecharge/cz_puller.pdf, 2009.

[105] Hüttinger Elektronik. Rf-generator. http://www.huettinger.com/, 2009.

[106] Heinz Konsolke Ingenieurbüro. Logoscreen cf. http://www.konsolke-messtechnik.de/t70.6570d_konsolke.pdf.pdf, 2006.

[107] ENGELHARD. Thermocouple reference data book. http://www.engelhard.com, 2004.

[108] M.H. Tavakoli, H. Wilke, and N. Crnogorac. Influence of the crucible bottom shape on the heat transport and fluid flow during the seeding process of oxide czochralski crystal growth. *Crystal Research and Technology*, 42:1252, 2007.

[109] J.M. Badie. Phases et transitions de phases à haute température dans les systèmes $sc_2o_3 - ln_2o_3$ (ln=lanthanide et yttrium). *Rev. Int. Hautes Temp. Refract.*, 15:183, 1978.

[110] M. Malki and P. Echegut. Ionic conductivity in glasses and melts (up to 1950k): Application to the $cao - sio_2$ system. *International Journal of Thermophysics*, 25(5):1495, 2004.

[111] T. Tsukada, N. Imaishi, and M. Hozawa. Theoretical study of the flow and temperature fields in cz single crystal growth. *J. Chem. Eng. Japan*, 21:184–191, 1988.

[112] V.J. Fratello and C.D. Brandle. Physical properties of a $y_3a_{15}0_{12}$ melt. *J. Cryst. Growth*, 128:1006, 1993.

[113] Y. Anzai, S. Kimura, T. Sawada, T. Rudolph, and K. Shigematsu. Measurement of density, viscosity and surface tension of molten lithium niobate. *J. Cryst. Growth*, 134:227, 1993.

[114] British Standards Institute. *BS188:1977 - Methods for Determination of the viscosity of liquids.* British Standards Institute, 1977.

[115] G. Schramm. *Einführung in praktische Viskosimetrie.* HAAKE Viskosimeter, 1981.

[116] RHEOTEST Messgeräte Medingen GmbH. Rheotest® rn 3.1 users manual. www.rheotest.de, 1997.

[117] The International Centre for Diffraction Data. Powder diffraction file: Card 027-0204. Newton Square/PA, 1999.

[118] International Standardization Organization. *ISO 15212-1:1998 - Oscillation-type density meters – Part 1: Lab. instruments.* ISO, 1998.

[119] D.C. Miller, A.J. Valentino, and L.K. Shick. The effect of melt flow phenomena on the perfection of czochralski grown gadolinium gallium garnet. *J. Cryst. Growth*, 44:121, 1978.

[120] T. Tsukada, N. Imaishi, and M. Hozawa. Global analysis of heat transfer in cz crystal growth of oxide. *J. Chem. Eng. Japan*, 27:25, 1994.

[121] T. Tsukada, N. Imaishi, and M. Hozawa. Effect of interface inversion on thermal stress field in cz crystal growth of oxide. *J. Chem. Eng. Japan*, 23:286, 1990.

[122] P.A. Sackinger, R.A. Brown, and J.J. Derby. A finite element method for analysis of fluid flow, heat transfer and free interfaces in czochralski crystal growth. *J. Num. Meth. Fluids*, 9:453, 1989.

[123] P.M. Gresho and J.J. Derby. A finite element model for induction heating of a metal crucible. *Journal of Crystal Growth*, 85:40, 1987.

[124] M.H. Tavakoli and H. Wilke. Numerical study of induction heating and heat transfer in a real czochralski system. *Journal of Crystal Growth*, 275(1-2):e85, 2005.

[125] M.H. Tavakoli and H. Wilke. Two and three-dimensional numerical modeling of induction heating in oxide czochralski systems. *Crystal Research and Technology*, 43(5):483, 2005.

[126] D.R. Lide. *Handbook of Chemistry and Physics*. CRC Press, 1999.

Selbständigkeitserklärung

Hiermit versichere ich, Nebojša Crnogorac, an Eides statt die vorliegende Dissertation selbständig, sowie nur mit den in dieser Arbeit aufgeführten Hilfsmitteln und Hilfen verfasst zu haben. Diese Arbeit wurde noch in keinem früheren Promotionsverfahren eingereicht, angenommen oder abgelehnt.

Nebojša Crnogorac Berlin, den 17.12.2013